NATURAL ATTENUATION OF BIODIESEL IN A SANDTANK EXPERIMENT

by

Keelin Scully

B.A.Sc., Queen's University, 2013

A THESIS SUBMITTED IN PARTIAL FULFILLMENT OF

THE REQUIREMENTS FOR THE DEGREE OF

MASTER OF APPLIED SCIENCE

in

THE FACULTY OF GRADUATE AND POSTDOCTORAL STUDIES

(Geological Engineering)

The University of British Columbia

(Vancouver)

March, 2017

Abstract

The use of alternative fuels, including biodiesel, has increased steadily in the last two decades, increasing the risk of accidental spills. However, a comprehensive understanding of the fate of biodiesel in the subsurface is currently lacking. A large sandtank experiment was conducted over 18 months to evaluate the spatial and temporal evolution of biodiesel biodegradation with a focus on vadose zone impacts. 80 L of biodiesel was applied to the center of the sandtank. Monitoring and analysis focused on two zones: the saturated zone including the capillary fringe, and the unsaturated zone. Measured parameters included surficial CO_2 and CH_4 effluxes, gas concentrations and their isotopic composition in the vadose zone, moisture contents and temperature. In the saturated zone, groundwater chemistry was characterized based on dissolved cation and anion concentrations, volatile fatty acids (VFAs), pH and alkalinity.

The experimental results displayed a rapid response to the biodiesel release, revealed by increases of surficial CO_2 effluxes and CO_2-concentrations in the vadose zone, while O_2 concentrations remained close to atmospheric levels. In the saturated zone, elevated VFA concentrations were observed together with pronounced increases in cation concentrations, specifically Ca, Mg, Fe and Mn, indicating the rapid development of anaerobic conditions. The generation of acidity associated with aerobic and anaerobic degradation reactions led to a decline in pH, locally to values below 5, likely inhibiting the progress of biodegradation. The onset of CH_4 generation was delayed and coincided with reaching maximum VFA concentrations in the saturated zone. CH_4 effluxes at the ground surface were limited; however, stable isotope analysis indicated that CH_4 oxidation in the vadose zone was weak, likely due to low-pH conditions. Increases in dissolved concentrations of Fe and Mn were attributed to the reductive dissolution of Mn- and Fe-oxides, with possible contributions from the dissolution of Fe- and Mn-bearing dolomite.

Carbon balance estimates showed that the biodiesel was recalcitrant to degradation, and at 590 days less than 5% of the biodiesel had been transformed to VFAs, CO_2 and CH_4. The average biodiesel degradation rate derived from the carbon balance is 1.3×10^{-8} mol L^{-1} H_2O s^{-1}, comparable to literature values.

Preface

This thesis is original, unpublished work. Experimental design was completed by the author, Dr. N. Sihota and Dr. K. Ulrich Mayer. All samples were collected by the author with help from Eli Riedl, Jannel Robertson, Eva Marcy and Laura Stewart. Samples were analyzed by the author or in commercial laboratories. Data interpretation and modeling was conducted by the author under guidance from Dr. K. Ulrich Mayer. All chapters were written by the author and edited by Dr. K. Ulrich Mayer.

Table of Contents

List of Tables

List of Figures

Acknowledgements

Thank you to Uli for being a wonderful supervisor – I am so grateful for your patience, support and sense of humour.

Thank you to my family for your continuous love and encouragement.

Thank you to my fellow students for your friendship and spirit of adventure.

I would also like to thank Joern Unger for help with construction of samplers, and David Jones and Charles Krzysik for help with software and programming issues. Thank you to Laura Laurenzi, Jarod Devries, Judah Chen, Eli Riedl, Jannel Robertson, Eva Marcy, Laura Stewart, Mike Zima, Elliott Skierszkan and Olenka Forde for help with sandtank construction, lab work and sampling. Thanks to Mingliang Xie for help with MIN3P and Tecplot and Daniele Pedretti for help with Matlab. I would like to thank Sean Crowe for providing the nutrients for the biostimulation event.

Funding for this work was provided by NSERC (Discovery Grant), NSERC (Discovery Accelerator Supplement), and an NSERC (Strategic Grant) held by K. U. Mayer. Funding for the sand tank and monitoring equipment was provided by Western Diversification and the Leaders Opportunity Fund from the Canadian Foundation for Innovation (CFI), both awarded to K. U. Mayer. The author would like to acknowledge Shell for provision of the sand required to carry out the experiments.

1 Introduction

1.1 Research Motivation

Increasingly, alternative fuels are being adopted worldwide to supplement petroleum hydrocarbon products in the interest of reducing the carbon footprint from fossil fuel use and to gain independence from imported oil (Hill et al., 2006). In 2015, world biodiesel production was greater than 23.7 billion litres (Statista, 2016). The growing use of biofuels comes with increased risk of accidental spills of such fuels, yet the fate of fuel compounds and degradation products, especially in the source zone, remains largely unknown. In addition, there is considerable interest and concern among policy makers, regulators and industry related to higher expected methane (CH_4) generation rates associated with biofuel spills. The presence and spreading of CH_4 generated by biofuel degradation may also enhance the extent of anaerobic conditions in the subsurface and in this way promote the migration and persistence of BTEX compounds in groundwater and the vadose zone.

Although significant progress has been made in recent years, the impacts of subsurface releases of highly degradable alternative fuels, in particular biodiesel, are not fully understood. The bulk of recent research on alternative fuel spills has focused on the environmental impacts of ethanol (eg. Capiro et al., 2007; Freitas et al., 2010; Sihota et al., 2013); however, the effects of biodiesel releases to the subsurface have not been fully evaluated. One concern is the potential for rapid generation of CH_4, which may lead to explosive conditions in underground structures, as previously identified for ethanol-blended fuels (Freitas et al., 2010; Jewell and Wilson, 2011). In addition, increased gas generation may increase the risk of vapour intrusion of BTEX compounds (benzene, toluene, ethylbenzene, and xylene) (Ma et al., 2012; Jourabchi et al., 2013). Although these compounds are not present in biodiesel, they may also exist in the subsurface below storage facilities and service stations, owing to pre-existing fuel spills containing petroleum hydrocarbons.

1.2 Literature Review

Alternative fuels for diesel engines are being used more frequently due to the depletion of fossil fuel resources and worsening of emissions from motor vehicles (Fang and McCormick, 2006). Vegetable oils have been used directly for operating diesel engines since the early 1900s; however, these oils have problematic characteristics which may cause thickening of lubricating oil and carbon deposits in the engine (Leung et al., 2006). These properties may damage the normal operation of a diesel engine and reduce its lifespan. In response to these issues, biodiesel was developed as a less complex derivative of long-chain vegetable oils. In particular, biodiesel has become more widely used since the 1970s due to its many environmental advantages (Fang and McCormick, 2006).

Biodiesel is a non-toxic, biodegradable biofuel made up of methyl esters of long chain fatty acids and is produced from organic feedstocks such as vegetable oils or animal fats. A process called transesterification, which removes glycerin and lowers viscosity, is the most common method for producing biodiesel (Meher et al., 2006). Transesterification involves a chemical reaction between the high free fatty acid feedstock reacting with an alcohol (usually methanol but sometimes ethanol) and a catalyst (such as sodium hydroxide or potassium hydroxide) (Pasqualino et al., 2006). Impurities such as dirt and water are removed from the feedstock before the lipid is reacted with the alcohol. The reaction produces glycerin and an ester: biodiesel. The biodiesel is treated to remove all traces of soap, glycerol, excess alcohol and water. Soap formation and emulsions can occur when moisture reacts with the catalyst during the transesterification process (Sanford et al., 2009).

The most critical fuel quality parameter is reaction completeness, so reactions typically involve a trade-off between reaction time and temperature (Lower Mainland Biodiesel, 2012). Biodiesel yields 93% more energy than is invested in production and greenhouse gas emissions are reduced 41% relative to the fossil fuels displaced by biodiesel use. Relative to ethanol, biodiesel releases per net energy gain just

1.0%, 8.3% and 13% of the agricultural nitrogen, phosphorus and pesticide pollutants, respectively. This advantage comes from lower agricultural inputs and more efficient conversion of feedstocks to fuel (Hill et al., 2006). Unfortunately, high production costs made both biofuels unprofitable without subsidies until recent increases in petroleum prices. In the last 15 years, biodiesel production has risen steadily (Statista, 2016).

The composition of biodiesel is highly variable. Fatty acid methyl esters (FAMEs) typically have very low solubility (10-20 mg L^{-1}) whereas fatty acids have higher solubility (approximately 70-700 mg L^{-1} depending on pH). The various combinations of source oils and additives equates to over 1.5 million possible B100 formulations (Hodam, 2008).

The Feedstock and Biodiesel Characteristics Report (Sanford et al, 2009) measured the parameters for 34 types of feedstocks and their respective biodiesels. The results of used cooking oil biodiesel (which was used in the experiment performed for this thesis) are summarized in Table 1-1 below. These parameters provide a general idea on the composition of this type of biodiesel, but are not necessarily reflective of the biodiesel used for this study.

Table 1-1: Used Cooking Oil Biodiesel - Select Parameters (from Sanford et al., 2009)

Parameter	Used Cooking Oil	Biodiesel	Max value
Moisture content (% by wt.)	0.242	0.038	
Free fatty acid content (% by wt.)	2.72	4.332	
Kinematic viscosity ($mm^2 s^{-1}$ at 40 degrees C)	27	4.3	
Saponification value (g KOH g^{-1})	198.5		
Total acid number (mg KOH g^{-1})		0.332	
Oxidation stability (h)	2.8	1	
Sulfur content (ppm)		2.4	15 (ASTM D6751)
Phosphorus content (ppm)	27	<0.1	10 (ASTM D6751)
Calcium content (ppm)	0.1	0.6	5 (Mg + Ca) (ASTM D6751)
Magnesium content (ppm)	0.8	1.1	
Relative density		0.8555	
Flashpoint (degrees C)		>160	

Used cooking oil is composed mostly of yellow fats. Based on the measured saponification value of 198.5 g KOH g^{-1}, the feedstock is likely to have mostly fatty acids with a chain length between 16 and 18 carbons (Sanford, 2009).

The oxidation stability of biodiesel from used cooking oil is 2.8 hours; the higher this value, the more resistant the oil or fat is towards oxidation (Sanford et al., 2009). When biodiesel made from unsaturated oil reacts with oxygen, it can form a free radical which can react directly with oxygen, leading to the formation of a peroxide or hydroperoxide molecule. Later, aldehydes and ketones are formed and finally, the formation of a resin can make the biodiesel fuel unusable (Shah et al., 2009). The formation of peroxides, aldehydes and ketones may affect the pH in an experimental system involving biodiesel. The oxidation stability value may be indicative of the age or prior storage conditions of the oil or fat and can predict if the feedstock is capable of meeting the minimum requirements for biodiesel oxidation stability (ASTM D6751). Since oxidation can occur at points where hydrogen atoms occur next to carbon-carbon double bonds, the presence of these structures will affect the oxidation stability. This parameter is also influenced by the presence of naturally occurring antioxidants in the feedstock that can prevent oxidation of the triglyceride molecules.

Phosphorous, calcium, and magnesium in a feedstock may act as emulsifiers or cause sediment, lowering yields during the transesterification process. They are minor components typically associated with phospholipids and gums (Sanford et al., 2009). The phosphorous content of used cooking oil is 27.0 ppm; this is a significant concentration although the value may be reduced during the transesterification process. The calcium content is 0.1 ppm, and the magnesium content is 0.8 ppm; these values would be negligible in relation to the Ca and Mg balance in a soil.

The density of used cooking oil biodiesel relative to water is 0.86 g cm^{-3} and the kinematic viscosity is 4.3 mm^2 s^{-1}. Biodiesel kinematic viscosities are all lower than those presented by their respective oils or fats.

This is an expected finding since biodiesel molecules are single, long chain fatty esters with higher mobility than the bigger and bulkier triglyceride molecules. The same trends found for kinematic viscosity in the feedstocks are found in the biodiesels.

The Total Acid Number (TAN) for used cooking oil biodiesel is 0.33 mg KOH g^{-1}. This parameter assesses the quality of a particular biodiesel by indicating the degree of hydrolysis of the methyl ester. This is a particularly important parameter when considering storage and transportation of large quantities of free fatty acids, which can cause corrosion in tanks (Sanford et al., 2009).

1.2.1 Experiments on Microbial Degradation of Fuels in the Subsurface

Fuel degradation may occur via microbial respiration; in this case, an electron acceptor present in the subsurface is reduced, while biodiesel is used as substrate. Microbes can use the energy released when electrons are passed from an organic carbon atom to an oxidized ion. Under thermodynamic equilibrium conditions, electron acceptors in the subsurface are used sequentially following the redox ladder, which moves from oxic to anoxic conditions from O^0, N^{5+}, Mn^{4+}, Fe^{3+}, S^{6+} and finally C^{4+} (Baedecker et al., 1993). This order is based on the electron acceptor which provides the most energy for the microbes when it is reduced. Solid phase electron acceptors such as Mn- and Fe-oxides undergo reductive dissolution, releasing Mn^{2+} and Fe^{2+} to the groundwater, possibly resulting in the formation of secondary minerals such as rhodochrosite ($MnCO_3$) and siderite ($FeCO_3$) (Baedecker et al., 1993). The process of biodegradation also leads to the generation of gases such as CO_2 and CH_4, possibly leading to gas exsolution and transfer of gases to the ground surface resulting in surface gas effluxes (Sihota et al., 2013). The center of a plume is typically characterized by the most mature processes, i.e. the processes furthest down the redox ladder.

However, in nature, groundwater systems are highly heterogeneous, both from a physical and geochemical perspective, and redox conditions are unlikely in a thermodynamic or compositional

equilibrium (Christensen et al., 2000). The effect of heterogeneity is very difficult to account for and may cause redox zones to show unexpected spatial variations, overlaps, or indicate that several terminal-electron accepting processes (TEAPs) occur in parallel.

As the bottom of the redox ladder is approached, the onset of methanogenesis leads to the production of methane gas. The methane gas produced will either remain dissolved in the groundwater or exsolution may occur, creating a buoyancy- or gradient-driven flux of methane gas away from the reaction zone with components of the flux directed towards the surface. In some cases, methane gas efflux is measurable at the surface above a contaminated site, even years after the area has become contaminated (Sihota et al., 2013). Significant methane flux can be harmful to the ecosystem, and can create an explosion hazard, if the gas builds up in underground structures such as basements.

To predict the potential for CH_4 generation and its fate in groundwater and the vadose zone, it is critical to gain an understanding of the microbial communities present in the subsurface and their response to a fuel release, i.e. substrate addition. According to Chen et al. (2008) the microbial response to new substrate often occurs in two stages: an initial stage of decline in microbial activity due to toxicity, followed by a period of microbial growth stimulated by the presence of substrate and a shift in community composition and metabolic potential. An overall loss of microbial diversity may be expected toward microorganisms that metabolize fuel compounds and their degradation products (Bekins et al., 1999).

1.2.2 Biodiesel Degradation Experiments

Numerous biodiesel degradation experiments have focused on quantifying fuel degradation in the interest of preventing the formation of degradation products which affect engine performance (e.g. Leung et al. 2006; Fang and McCormick, 2006; Aquino et al. 2012). However, biodegradation of biodiesel

in the subsurface and associated effects on groundwater quality have not been studied extensively, aside from a few notable exceptions, which are described below.

Corseuil et al. (2011) examined the biodegradation of soybean and castor oil biodiesel using microcosm experiments. The experiments were run under anoxic conditions. They found that 80% of the soybean biodiesel was biotransformed in 41 days, while 40% of the castor oil biodiesel was removed in 90 days. Castor oil biodiesel has a higher viscosity and lower bioavailability, which may be the cause of this difference. Additional microcosms were amended with benzene and toluene with or without soybean biodiesel to determine the effect of the biodiesel on hydrocarbon degradation. The presence of biodiesel appeared to slow the removal of both toluene and benzene.

Ramos et al. (2013) conducted parallel field experiments to evaluate the degradation of B20 biodiesel blends with or without biostimulation. B20 relates to a fuel that consists of 20% biodiesel and 80% diesel fuel derived from crude oil. 100 L of B20 was released at the water table over two 1 m^2 plots. One release was biostimulated with weekly injections of ammonium acetate over 15 months, the other release served as a baseline control. The biostimulated release created near-saturation methane concentrations, indicating strongly methanogenic conditions, and BTEX removal began within 8 months. In the control source zone, BTEX concentrations were still increasing 2 years after the injection due to source dissolution, showing a high degree of persistence and a small potential for degradation.

Biodiesel has also been shown to dissolve crude oil and its derivatives. An experiment by Miller and Mudge (1997) assessed the effectiveness of biodiesel as a solvent for crude oil at contaminated beaches by constructing laboratory sand columns and attempting to remediate the crude oil contamination in the columns using biodiesel. When the biodiesel was applied directly to unweathered crude oil, there was a greater recovery of oil from the sediments.

A PhD thesis from Ali (2011) examined the microbial degradation of volatile petroleum hydrocarbons in an aerobic sandy soil with and without the blending of E10 and B20 in batch microcosms and mini-lysimeters. All volatile compounds in the mini-lysimeters remained above detection limits over 92 days except toluene which dropped below detection in the microcosm with E10 blend. The mass percentage of each petroleum hydrocarbon compound remaining at the end of the experiments was comparable for all fuel mixtures, except for m-xylene which declined significantly less in E10 compared to B20. Under aerobic conditions, competition for scarce inorganic nutrients seemed to be the most plausible reason for slower monoaromatic hydrocarbon biodegradation in the presence of more readily degradable biofuel.

The PhD thesis completed by Hatch (2011) described a multimedia risk assessment for biodiesel by examining aquatic toxicity, biodegradation, and subsurface fate and transport. Anaerobic microcosm experiments performed by this author revealed that both soy and animal fat biodiesel were more readily degradable than Ultra-Low-Sulfur Diesel (ULSD). However, the experimental results suggested somewhat increased toxicity for biodiesel for 6 aquatic species relative to ULSD. Fuel fate and transport in the subsurface was very similar for both biodiesel and ULSD, particularly with regards to lens formation and geometry.

Although these previous experiments involved biodiesel blends and assessed potential impacts on degradation of other fuels, to the author's knowledge there has been no research which examines the environmental impacts of a biodiesel (B100 = 100% biodiesel) release in the vadose zone, with an emphasis on assessing fuel persistence and the potential for methane generation and migration.

1.3 Identification of Knowledge Gaps

A comprehensive understanding of the fate of biodiesel in the vadose zone and the capillary fringe, including interactions with degradation products (e.g. volatile fatty acids (VFAs – acetate, butyrate and

propionate), CO_2 and CH_4) is currently lacking. Since biodiesel is less dense than water, many of the impacts of a biodiesel spill are expected to take place in the unsaturated zone, which is of particular concern in shallow, unconfined aquifers. Based on previous studies (Corseuil et al, 2011), biodiesel is a readily degradable compound with substantial potential for the development of anaerobic conditions, yielding rates of CH_4 generation that exceed acceptable levels. These properties may result in an increased risk for soil vapour intrusion of CH_4 into buildings and other subsurface infrastructure located in the vicinity of a biodiesel-related subsurface contamination.

1.4 Thesis Objectives and Study Approach

The overarching objective of this work was to investigate biodegradation processes in response to a surficial controlled release of biodiesel (B100) onto vadose zone sediments. To this end, a large-scale sandtank experiment was constructed with a 1-meter thick vadose zone. A biodiesel spill of known volume was applied at the surface and the spatial and temporal evolution of gas and water chemistry due to biodiesel degradation reactions were characterized over an 18 month period. Specific research questions addressed through this study include:

(i) How does biodiesel redistribute itself in response to the surface release?

(ii) Which processes affect or control biodiesel degradation under the given experimental conditions, and how do these processes evolve? What are the terminal electron accepting processes in response to the biodiesel application and how do they evolve over time?

(iii) Does biodiesel degradation lead to significant generation of CO_2 and CH_4 in the subsurface?

(iv) How persistent is biodiesel under the experimental conditions and what is its rate of degradation?

(v) What is the composition and magnitude of surface gas effluxes above and in the vicinity of the spill?

(vi) Based on subsurface gas concentrations, what is the risk for soil vapor intrusion of CH_4 in response to biodiesel spills?

(vii) What are the secondary impacts of biodiesel degradation on aqueous and gaseous geochemistry in the spill zone?

To address these research questions, the sandtank experiment was equipped with a dense monitoring network consisting of an array of sensors, sampling ports, and devices to measure surface gas emissions. The methods used for this research included:

1) Collection and analysis of discrete gas samples to quantify vadose zone gas concentrations.
2) CO_2 and CH_4 flux chambers including a laser-based high resolution greenhouse gas analyzer to quantify surficial gas emissions.
3) Compound-specific C isotopes in CO_2 and C and H isotopes in CH_4 to characterize degradation pathways
4) Collection and analysis of discrete aqueous samples from the saturated zone to determine concentrations of volatile fatty acids (acetic, propionic and butyric acids)
5) Collection and analysis of discrete aqueous samples from the saturated zone to complete cation and anion scans to determine concentrations of important elements
6) Monitoring of pH in the saturated zone of the sandtank at 10 locations along two horizontal transects in the tank; in addition, one snapshot of total alkalinity was obtained along one horizontal transect
7) Continuous monitoring of electrical conductivity, volumetric water content, matric potential, temperature, and O_2 and CO_2 concentrations via a network of sensors embedded in the sandtank

8) Preliminary process-based multicomponent reactive transport modeling to provide a quantitative and integrative assessment of laboratory data

These methods were applied in an integrated manner to identify microbiological controls on biofuel degradation, delineate zones of maximum and inhibited biodegradation, and to characterize subsurface gas distribution and composition with an emphasis on determining maximum CH_4 concentrations. The results of this work help determining risks associated with biodiesel spills and inform remediation policies associated with biodiesel releases to the subsurface.

This thesis is structured in the following way: Chapter 2 describes the design and construction of the sandtank experiment, as well as detailed methodologies for each type of analysis conducted over the duration of the experiment. Chapter 3 describes the results of these analyses, as well as the discussion of a qualitative conceptual model to describe the overall system of reactions. Chapter 4 describes the reactive transport simulations which were created to test the validity of the conceptual model. Finally, Chapter 5 provides a brief summary and conclusions.

2 Construction and Methodologies

2.1 Introduction

The sand tank experiment was conducted to evaluate biodegradation of biodiesel under nutrient-limited and nutrient-amended conditions. The data obtained provides information on the rate, timing and spatial distribution of biodiesel degradation. The purpose of the current chapter is to provide a detailed description of the sandtank construction and instrumentation as well as the laboratory methods and analytical procedures used.

2.2 Sandtank Construction

The experiment was set up in the Environmental Interfaces Laboratory (EIL), a new facility at the University of British Columbia (UBC). The sandtank (pictured in Figure 2-1) is 400 cm long, 100 cm wide and 150 cm tall. The apparatus was designed with a large volume to provide sensitivity toward the development of concentration gradients, and to provide sufficient space for the emplaced sensors. The sandtank is equipped with two chambers on either side of the tank to control the water level within the tank. These chambers can also be utilized to induce horizontal flow through the sandtank; however, for the purpose of this experiment, a flat water table was set at approximately 30 cm from the bottom. The surface of the sandtank is open to the atmosphere and allows oxygen ingress into the tank.

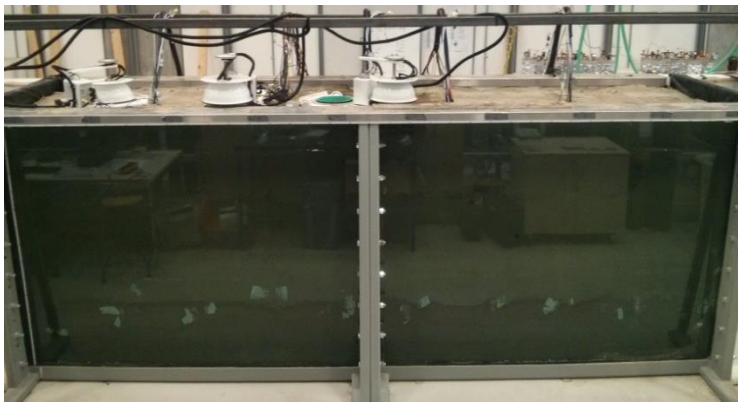

Figure 2-1 Sandtank (front panel)

The sandtank monitoring set-up consists of a network of ports and sensors as well as surface efflux measurements. The ports are accessible from the rear of the sandtank, and the sensors were inserted from the top. The fluxes and sensor information are data logged using a custom-built data acquisition system.

The sensors were emplaced to continuously measure O_2, CO_2, moisture content, matric potential, electrical conductivity (EC), and temperature. All sensors were calibrated and/or tested before insertion into the sandtank, as described in the following sections for each sensor type. The wires were fed through the top of the sandtank (Figure 2-2[A]), as the tank was filled with sand. The data logging set-up on the rear panel of the sandtank is shown in Figure 2-2[B] and Figure 2-2[C]. The set up includes Labjacks (Labjack Corporation, 2015) and Arduinos (Arduino AG, 2017), as well as the computer running the programs for autonomous data collection. Labjacks and Arduinos are two types of measurement and automation devices which provide digital inputs and outputs

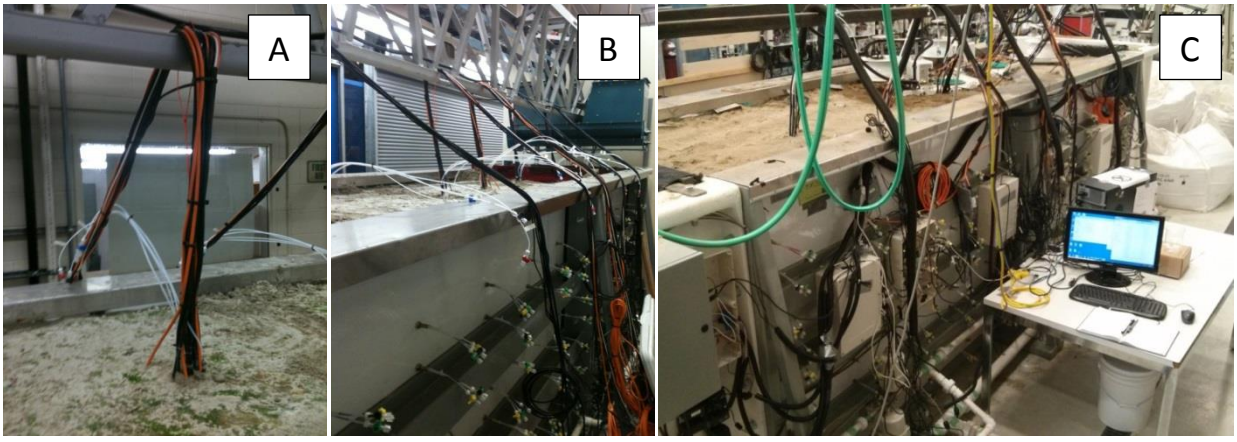

Figure 2-2: Sandtank sensors were inserted from the top, and wires were routed through the sand [A]. Data logging set-up at the rear of the sandtank, including Labjacks, Arduinos and the computer which ran the data acquisition programs [B and C].

The spatial arrangement of the sensors is shown in the Figure 2-3. GS3 sensors (5TE probes) from Decagon were used for continuous measurement of soil volumetric water content (VWC), EC and temperature. These sensors are equipped with an epoxy body to protect the sensor. The accuracy is +/- 3% for VWC, +/- 5% for EC and +/- 1 ^{o}C for temperature. The sensors were tested to ensure they

produced a response, but were left at factory calibration. During installation, the GS3 sensors were handled with latex gloves to prevent oil or any non-conducting residue from coating the prongs. The installation of these sensors required a minimum of 5 cm of undisturbed soil around the sensor prongs (a 0.3 L volume of influence). Care was taken to ensure that soil was packed tightly around the sensors to prevent air gaps; however, soil was tamped down lightly to avoid damaging the sensors. It should be noted that electrical conductivity measurements are unusable if the soil becomes too dry (i.e. if the volumetric water contents fall below 10 v/v%).

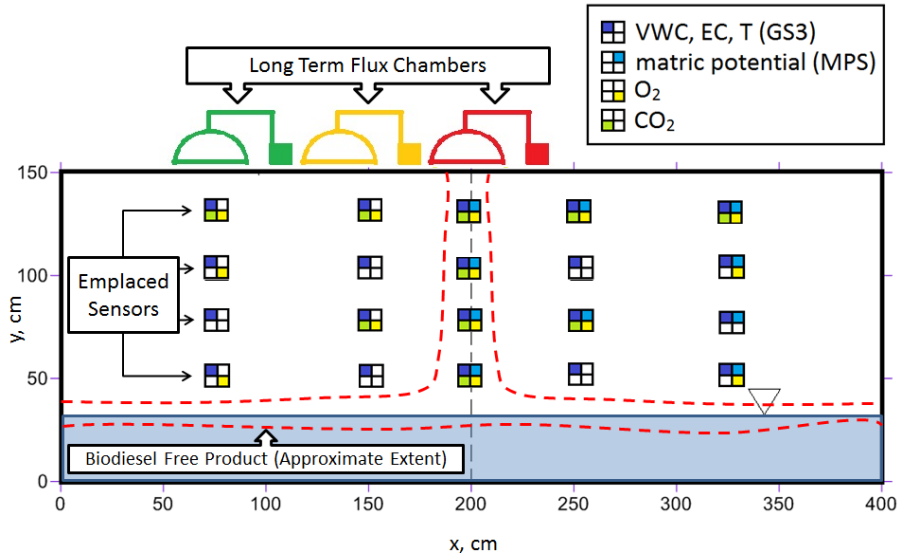

Figure 2-3 Schematic of emplaced sensor locations

The Decagon MPS-2 sensors were used to measure dielectric water potential and temperature. The accuracy of these sensors is +/- 25% for soil water potential in the range of -5 to -100 kPa, and +/- 1 ^{o}C for soil temperature. The MPS-2 sensors were also inserted with their original factory calibration. Like the GS3 sensors, the MPS-2 sensors were installed using latex gloves to prevent oils from touching the ceramic discs. To prepare the sensor for installation, wet native soil was packed around the entire sensor; care was taken to ensure moist soil was in contact with all ceramic surfaces. The sensors were positioned so that the ceramic faces were horizontal and a minimum of 4 inches of unbent cable extended from the sensor head.

The GS3 and MPS-2 sensors were attached to a string and carefully lowered into the sandtank from above. The end of the cable was pulled through the sensor port using the string and connected to one of three Arduinos on the rear of the sandtank (Figure 2-2 B). The Arduinos ran a program, which allowed for autonomous measurements to be taken and recorded every two minutes for each sensor. The Arduino program can be found in Appendix A.1. After installation, the responsiveness of the installed moisture sensors was tested via a water infiltration test, where approximately 100 L of water was applied to the top of the sandtank and the sensors' response, as the water filtered down, was monitored. The results of this infiltration test can be found in Appendix A.2.

The oxygen sensors used in the sandtank are Apogee SO-110 sensors (Apogee Instruments, Inc, 2015). These sensors measure O_2 concentrations between 0 and 100% as partial pressure O_2 with errors less than 1% when the sensors are new. Over time, a signal decrease of 0.8 mV (approximately 1% O_2) per year is expected (Apogee Instruments, Inc, 2015). The O_2 sensors were calibrated using a two point calibration (0% and 21% O_2). For calibration, the sensors were inserted into a sealed glass box and the gas of known concentration was pumped into the container. The measured voltages for the two concentrations were used to create a formula, which was inputted to the Labjack program to provide a reference for the sensor output. The O_2 sensors were retested after insertion in the sandtank by pumping gas of a known concentration (0% and 21%) into the ports near the sensors for twenty minutes, while monitoring their response. The results of this test are shown in Appendix A.3.

The CO_2 sensors are the premier miniature infrared sensors from Dynament with a range of 0-5% (resolution of 10ppm), 0-10% (resolution of 20 ppm) or 0-20% CO_2 by volume (resolution of 50 ppm) (Dynament Inc, 2011). PTFE membranes were used to provide a custom-made sensor housing and protect the sensors from soil moisture. The CO_2 sensors were calibrated using a two point calibration (0% and the upper range of the CO_2 concentration measured by each sensor). Like the O_2 sensors, the

CO_2 sensors were inserted into a sealed glass box and the gas of known concentration was pumped into the container. The measured voltages for the two concentrations were used to create a formula to input to the Labjack files to provide reference values and to calibrate the sensor output. The results of this test are shown in Appendix A.3.

The Apogee and Dynament sensors were interfaced using LabJack (U3) data acquisition systems and terminal boards. Amplifiers were used for signal adjustment. Data logging for O_2 and CO_2 concentrations was conducted using a personal computer and LabView software (available through a UBC license). The Labview program is included in Appendix A.4. Gas concentration measurements were also taken every two minutes.

The sandtank is equipped with a network of 300 gas sampling ports, which are accessible from the rear panel. A representative selection of these ports was used for the collection of discrete gas and water samples; the ports used are specified for each type of analysis in the following sections. As seen in Figure 2-4 [A] and [B], the ports were positioned spatially in the sandtank using wires. The ports are vertically distributed every 10 cm between 30 cm and 120 cm from the base of the tank, and horizontally spaced every 40 cm between 20 cm and 380 cm along the length of the tank. This 2-dimensional grid of ports is repeated three times at 25 cm, 50 cm and 75 cm into the tank (from the front glass panel).

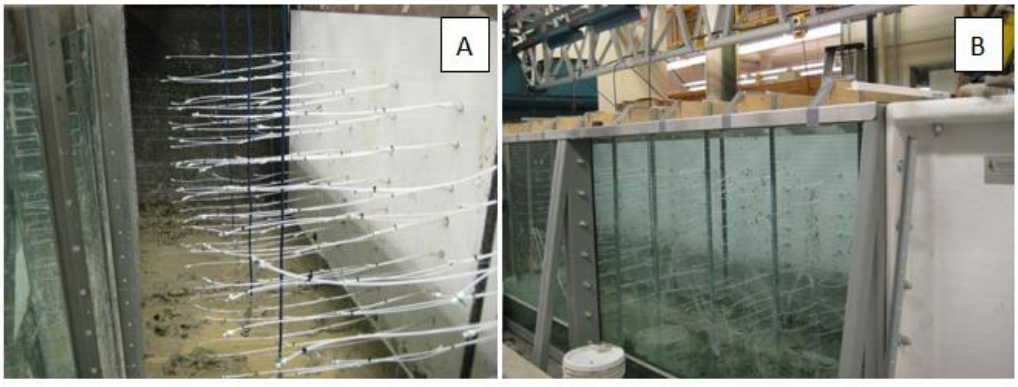

Figure 2-4: Network of ports positioned in the sandtank before filling

Figure 2-5 shows a schematic of the port locations over the length and height of the sandtank. This schematic will be used to highlight the ports which were sampled for the various types of analyses.

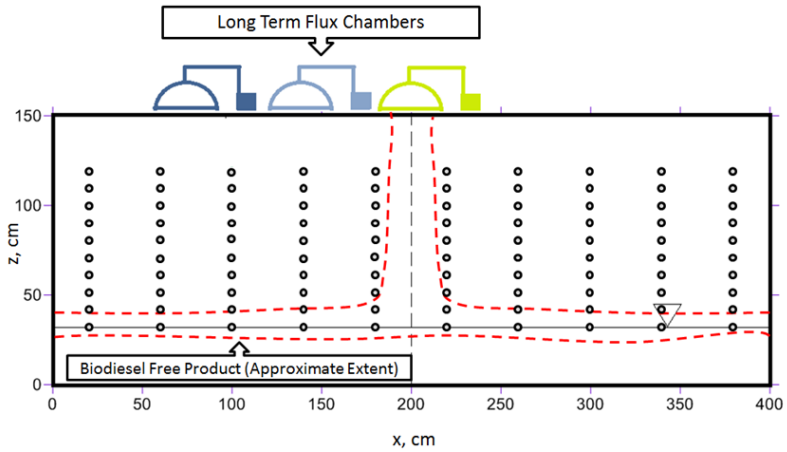

Figure 2-5: Schematic of port locations from front panel (2-D rendition)

2.2.1 Sediments

The tank was filled with unwashed silty sand obtained from a local source. Sediments for this experiment were obtained from the vadose zone at a former refinery in the Lower Mainland near Burnaby, British Columbia and were donated to the University of British Columbia for this study. The material used was clean and devoid of any contamination.

A grain size analysis was performed on the sediments via the following method:

1. The sample volume was measured in a falcon tube.
2. The mass of an aluminum pan was determined (and the value recorded), then the sample was transferred to the aluminum pan and this mass was also recorded.
3. The sample was dried in the oven at ~100 ^{o}C overnight. The mass of the dried sample was then measured and recorded.
4. The sample was washed through the 75 µm sieve (No. 200) with a No. 20 sieve nested above to retain coarser material. The material was transferred into a separate labelled aluminum pan of known mass, dried in the oven at 100 ^{o}C overnight, and the mass was measured and recorded.

5. The remaining sample was sorted through a series of sieves (No. 6, No. 12, No. 20, No. 50, No. 100 and the initial No. 200 sieve). Each retained fraction was transferred into a separate labelled and aluminum pan of known mass, dried in the oven at 100 ^{o}C overnight, and the mass was measured and recorded.

Total carbon (TC), total inorganic carbon (TIC), total organic carbon (TOC), and percentage abundance of metals were measured by Multi-Acid Digestion with ICP-MS finish. Samples were sent to and processed by SGS in Vancouver, BC. A representative sample was taken each from Sand-1 and Sand-2, which were the two sediment charges used to fill the sandtank.

Samples were also collected for qualitative and quantitative analyses by X Ray Diffraction (XRD). The minerals present in Sand-1 and Sand-2 were determined through qualitative XRD results from diffraction patterns using the International Centre for Diffraction Database PDF-4 and Search-Match software by Bruker. Full details of the quantitative XRD process are described by Klassen (2015).

Samples for baseline microbial analysis were collected from multiple locations during the filling phase. The analysis of these samples will be completed by Ashley Arnold for her M.Sc. thesis (UBC Dept. of Microbiology and Immunology).

The sand was emplaced in the tank in lifts ranging from 5 to 10 cm to prevent the development of macroscopic vertical differences in hydraulic conductivity. Packing was done evenly over the entire surface, paying close attention to avoid allowing cavities to develop along the side wall. Each layer was compacted with a 10 cm plastic disk fitted to the end of an 8 ft steel pipe until further compaction was no longer possible. After each packing, the surface was scarified to maintain a vertical hydraulic connection and to help eliminate differences in hydraulic conductivity. The soil was filled to approximately 2 cm below the planned sensor location to allow space for sensor placement.

A grain size analysis was completed on the sediments from the bags of sediment used to fill the sandtank (Klassen, 2015). The results are shown in Figure 2-6.

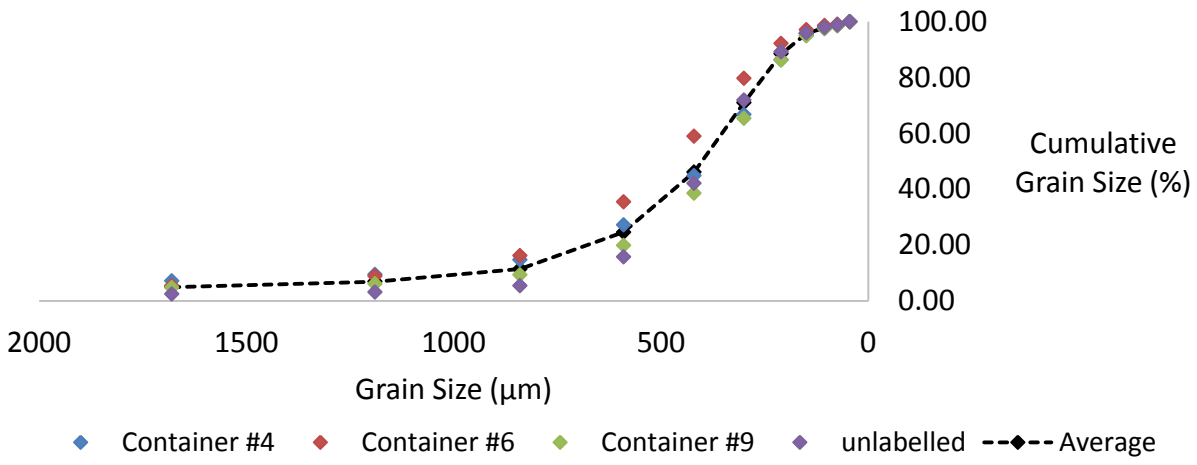

Figure 2-6: Cumulative Grain Size Curve – Percent (adapted from Klassen, 2015)

The grain size curve seemed to be reproducible between all bags sampled. On average between the four samples, the mean grain size is 450 µm with a range of 395-530 µm. The mean grain size was calculated using the formula

$$GM_e = \frac{\varphi_{16} + \varphi_{50} + \varphi_{84}}{3}$$

which sums the grain sizes corresponding to the 16%, 50% and 84% mark on the cumulative frequency distribution curve and calculates an average.

2.2.2 Water Composition

Vancouver tap water, amended with Nutrafin™ to remove chlorine, was infiltrated to the sandtank and the water table was set at 30 cm. Water was infiltrated from the top of the sandtank, wetting sediments in the vadose zone. Chemical and physical parameters obtained from the analysis in the water quality report published by the Vancouver Water Utility are shown in Table 2-1. The average conductivity is 29.6 µs cm^{-1} which is considered low for tap water.

Table 2-1: Water quality results for Vancouver tap water (City of Vancouver, 2015)

	Results				
Parameter	**Avg**	**Min**	**Max**	**Guideline**	**Reference**
Chlorine – total (mg L^{-1} Cl_2)	0.70	0.08	1.59	<4 mg L^{-1} Cl_2	EPA
Conductivity (µs cm^{-1})	29.6*	21.6	41.6	None	
pH	7.31	6.35	8.21	6.5-8.5	GCDWQ
Turbidity (NTU)	0.19	0.02	5.51	<1 NTU	GCDWQ

2.3 Flux Chambers and Measurements

Surficial CO_2 and CH_4 efflux measurements have been used previously at contaminated sites to delineate hydrocarbon source zones and to estimate depth-integrated contaminant degradation rates (Sihota et al., 2011). This technique was used in the sandtank experiment to determine the total CO_2 and CH_4 effluxes.

For this experiment, three long-term soil gas flux chambers have been deployed for long-term monitoring of CO_2 and CH_4 emissions. Chamber 1 is located 50 cm from the edge of the sandtank, Chamber 2 is located 125 cm from the edge of the sandtank, and Chamber 3 is located directly in the middle of the tank over the spill zone (at 200 cm from the edge). This design was adopted to give an adequate spatial coverage of the gas fluxes from the sandtank for one half of the symmetrical tank, and this information will be used to approximate fluxes over the entire sandtank surface. Fluxes from the chambers are fed in series through a *LI-COR® LI-8100 analyzer* for CO_2-efflux analysis, and *an extended range LGR® GGA-EP (greenhouse gas analyzer)* for CO_2 and CH_4 efflux analyses. The gas line between the LI-COR infra-red gas analyzer (IRGA) system and the chamber was spliced to include the LGR GGA-EP cavity ring down laser spectroscopy (CRDS) analyzer, and a bypass line was constructed to account for the difference in pumping rates between the two instruments, similarly to Sihota et al. (2013). The chambers each took one gas efflux measurement every twenty minutes. A detailed diagram of the flux analyzer set up can be found in Appendix A.5.

The chambers remain in an open position until the program directs them to take a measurement. Following a purge cycle, a chamber will close and target a known area of sediment delineated by a partially buried soil collar. The increasing CO_2 and CH_4 content in the chamber head space during the period when the chamber is closed is measured by the analyzer. This rate of increase, combined with measured water content, pressure, temperature and system volume allows for the calculation of the gas efflux via the equation:

$$F = \frac{10VP_0\left(1 - \frac{W_0}{1000}\right)}{RA(T_0 + 273.15)} \frac{\partial C}{\partial t}$$

where F is the gas efflux [µmol m^{-2} s^{-1}], W_0 is the initial water vapour mole fraction [µmol mol^{-1}], T_0 is the initial air temperature [^oC], V is the total volume of the system (chamber, analyzers, tubing and the soil collar) [cm^3], P_0 is the initial pressure [kPa], A is the soil surface area [cm^2], R is the gas constant (8.314 [Pa m^3 K^{-1} mol^{-1}], and ∂C/∂t is the change in the dry air concentration of the gas species of interest (i.e. corrected for the water vapour flux) within the chamber headspace over the measurement period [µmol mol^{-1} s^{-1} or ppm_v s^{-1} of CO_2 or CH_4]. Sample calculations for the CH_4 efflux, as well as sample raw data, are found in Appendix A.6.

2.4 Biodiesel Release and Stages of Experiment

On March 17, 2015 80 L of biodiesel were applied at the surface in the central 0.5 m^2 rectangular portion of the tank. All results are plotted in elapsed time from this date. The pure biodiesel was dyed red with Sudan IV (1 mg per 10 L of fuel) to visually trace the migration of the biodiesel with LNAPL characteristics. The biodiesel percolated down through the sediment and spread laterally, pooling on the water table. Visible migration of biodiesel stopped after 3 days leaving behind a stagnant labile organic carbon source in the tank. Figure 2-7 shows the approximate extent of the biodiesel present in the sandtank as free product at the steady-state distribution. The extent of the biodiesel was

determined by visual inspection through the glass window to observe the red dye. In the vadose zone, it is assumed that the biodiesel is present at residual saturation. At the water table, the biodiesel has spread to form a pool across the length of the sandtank. Minor water table fluctuations may cause the pool of biodiesel to appear slightly thicker than it is in reality.

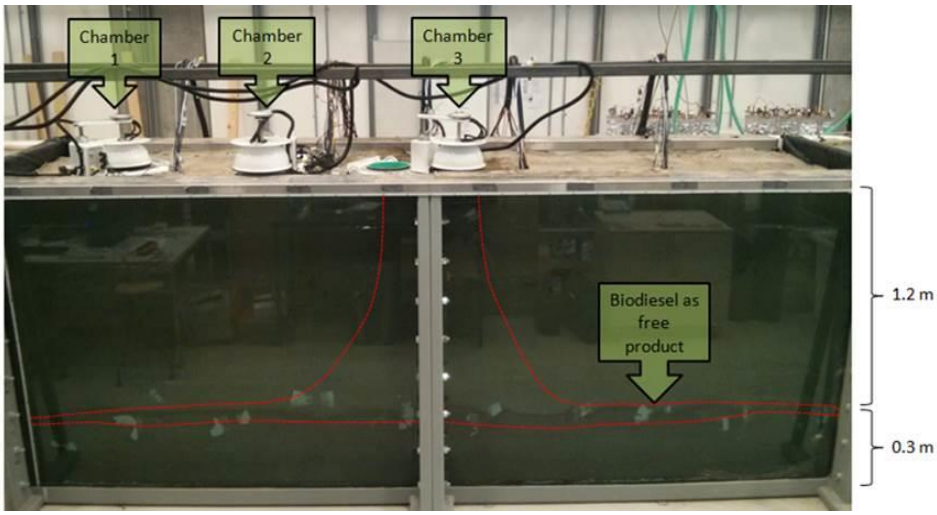

Figure 2-7: Approximate extent of biodiesel as free product in sandtank

Table 2-2 shows the elemental abundance of C, H, O and N in biodiesel relative to normal diesel according to an experiment performed by Lisiecki et al. (2013). This is useful as an approximation of the biodiesel used in this experiment since an elemental composition analysis was not performed on the biodiesel from the sandtank.

Table 2-2: Elemental composition of diesel (D) and biodiesel (B100) fuels (Lisiecki et al., 2013)

Fuel	C(%)	H(%)	O(%)	N(%)
Diesel	85.22 +- 0.47	14.67 +- 0.49	0.00 +- 0.01	0.11 +- 0.02
B100	74.13 +- 0.12	14.64 +- 0.34	10.92 +- 0.58	0.31 +- 0.13

Water was applied at surface on two occasions to simulate precipitation events and to avoid drying up of the tank by evaporation. The first application was on June 25th, 2015, 100 days after the start of the experiment. 240 L of Vancouver tap water was applied evenly to the surface of the tank over 8 hours following removal of chlorine with Nutrafin^{TM}. Nutrafin^{TM} is a biological aquarium supplement used to

remove chlorine, which is typically present in tap water. The chlorine was removed because it is toxic to bacteria in the sandtank. The second precipitation event occurred September 14th, 2015 (182 days after the start of the experiment) and was completed in the same way as the first precipitation event.

On January 14th, 2016, 304 days after the start of the experiment, the gas composition in the tank appeared to be nearing steady state conditions. A biostimulation experiment was initiated to evaluate its effect on biodiesel degradation. To this end, 100 L of Vancouver tap water was evenly applied to the surface of the tank over three hours. The water was amended with ammonium chloride and potassium orthophosphate. The concentrations of NH_4Cl and KH_2PO_4 were 7.5 mg L^{-1} and 1.4 mg L^{-1}, respectively. These values were chosen based on "typical" nutrient concentrations in groundwater. According to a USGS report by Mueller et al. (1995), 0.02 mg L^{-1} is representative of typical orthophosphate concentrations in groundwater. This concentration was used to calculate the amount of KH_2PO_4 required for the nutrient addition (accounting for dilution from water already present in the tank). The empirically derived Redfield Ratio (an atomic ratio for nitrogen to phosphorus) of 14:1 was then applied to calculate the amount of NH_4Cl. The Redfield ratio is the atomic ratio of carbon, nitrogen and phosphorus found in phytoplankton through the deep oceans and is believed to be related to nutrient requirements for many microorganisms. It should be noted that other elements (including sulfur, zinc, copper and iron) may also be important for microbial life; however, these elements were not specifically added to the amended tap water.

2.5 Sampling and Analysis Methods

2.5.1 Gas Chromatography

Samples collected from ports along four horizontal transects on one side of the sandtank were analyzed via gas chromatography. The samples were collected into 10 mL gas-tight syringes following a 10 mL purge of the gas line. The ports which were sampled are shown in Figure 2-8 in green.

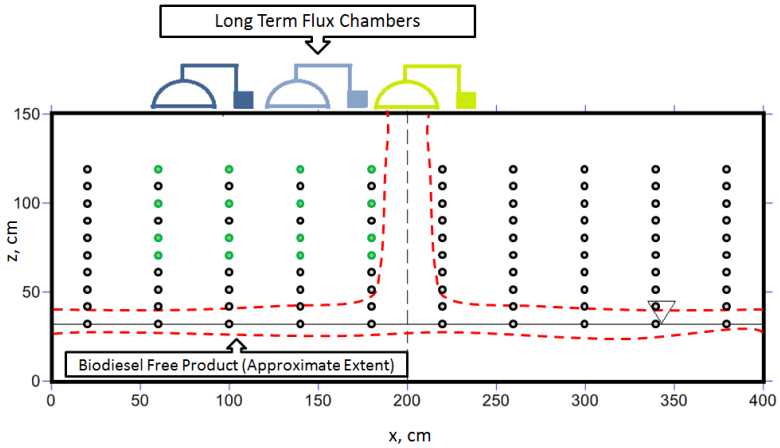

Figure 2-8: Ports sampled for gas chromatography are shown in green

The gas samples were analyzed on a Varian CP 4900 GC for Ar, CO_2, CH_4, N_2, and O_2. The GC has a Molsieve 5A PLOT column to separate Ar, O_2 and N_2 and a PoraPLOT U column to separate CH_4 and CO_2 (Amos et al., 2005). A baseline separation of Ar and O_2 can be achieved at ambient temperatures with the Molsieve column. The Varian GC requires helium as the carrier gas. Additionally, calibration gases and standards were used to calibrate and verify GC measurements. The gases used are summarized in Table 2-3. At the minimum, a 2-point calibration was performed for each compound. Calibration gases included atmospheric lab air, as well as elevated concentrations for CO_2 and CH_4; these were particularly important given the nature of these experiments. It should be noted that CO_2 in lab air is elevated; however, due to the low accuracy of the GC over this range; this was not an important source of error.

Table 2-3: Calibration gas compositions (Atmospheric Values from Pidwirny, 2006)

Gas	Ar	CH_4	CO_2	N_2	O_2
Atmospheric	0.93%	BDL**	BDL**	78.08%	20.95%
Standard 1*	0%	10%	10%	0%	0%
Standard 2	0%	20%	20%	60%	0%

*Balance is He; **Below Detection Limit, detection limit is approximately 0.1%

2.5.2 Volatile Fatty Acids (VFA)

Samples for VFA analysis were collected at ten discrete time intervals (approximately every 45 days) from fifteen ports over three horizontal transects as seen in Figure 2-9 in green. Samples were obtained above the water table (at 30 cm) following the application of a vacuum, since saturation in some

capillary fringe ports was high enough to obtain flowing water. Prior to sampling, 10 mL of water was purged from each port to remove stagnant water in the sampling line. The volume was calculated based on the diameter and length of the tubing as 5 mL, and the value was doubled. The 2 mL samples were collected and centrifuged through 0.22 micron filters to remove suspended matter that may damage or clog the GC. Aqueous samples were collected and frozen, then shipped to the UBC Bioreactor Laboratory at the University of British Columbia, Okanagan. There, the samples were analyzed for VFAs on an Agilent 7890A GC equipped with a 25-meter Agilent 19091F-112 column (0.32 mm ID, nitroterephthalic acid modified polyethylene glycol stationary phase), a flame ionization detector (FID) as well as an auto-sampler (Agilent Technologies, Santa Clara, CA) (T. Abbott, personal communication, Oct. 24 2016). The analyses reported concentrations of acetic acid, butyric acid and propionic acid with a minimum detection limit of 1 ppm. The accuracy of the analyses was +/- 5 ppm at high concentrations (above 100 ppm).

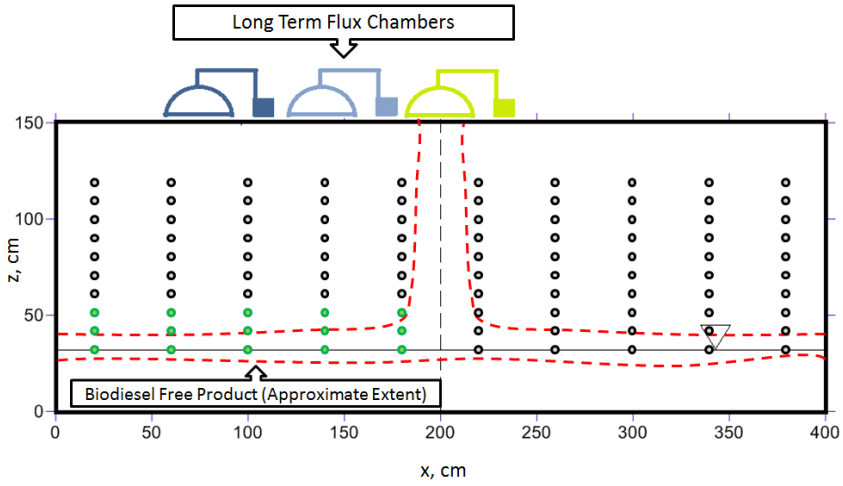

Figure 2-9: Ports sampled for VFA analysis are shown in green

2.5.3 Compound Specific Isotope Analysis (CSIA)

The sensors and GC results provide detailed spatial and temporal data, but do not reveal the controlling biodegradation processes. Gas samples were collected for carbon and hydrogen isotope analysis on CH_4 and carbon isotope analysis in CO_2 to help fill this crucial gap. Prior to sampling, 10 mL were purged from

each port to remove stagnant gas in the sampling line. Samples were collected via luer-lock syringes and injected through septa into 12 mL Labco vials to a pressure of approximately 2 atmospheres. Samples were collected at ten discrete time intervals (approximately every 45 days) from nine ports over three vertical transects to provide good spatial and temporal coverage. The sampled ports are shown in Figure 2-10 in green.

Samples were shipped to UC Davis, CA and isotope compositions were obtained for $\delta^{13}C$ in CO_2 and CH_4 and $\delta^{2}H$ in CH_4 at the University of California Davis Stable Isotope Facility. For carbon and hydrogen isotope analysis, gases were analyzed using a purge and trap system (Tekmar) coupled to an isotope ratio mass spectrometer (GC-IRMS) following the operational procedures described by Hunkeler and Aravena (2000). Average analytical errors for carbon and hydrogen isotope of 0.3 ‰ and 5 ‰, respectively, were obtained (R. Aravena, personal communication, Oct. 4 2016).

In addition, the isotopic signature of the biodiesel was measured initially (i.e. prior to application of the spill) and at two subsequent sampling events (at 65 days and 399 days) to track the isotopic enrichment of ^{13}C in the fuel at the University of Waterloo Environmental Isotope Laboratory.

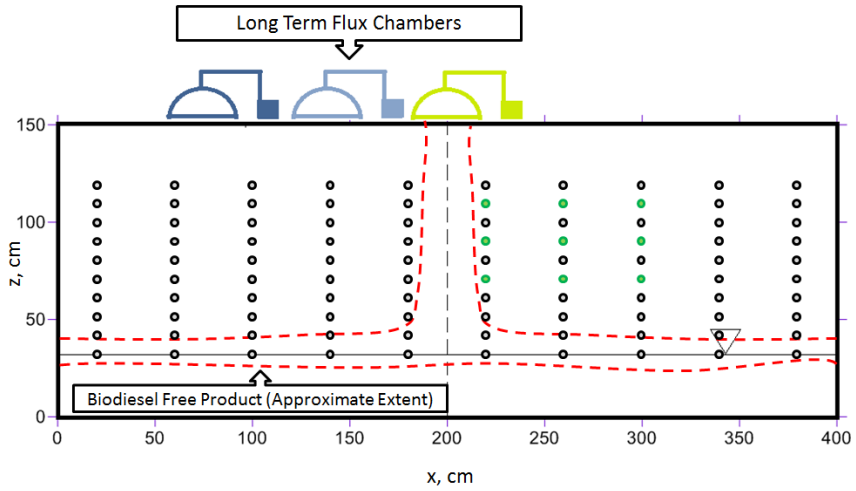

Figure 2-10: Ports sampled for CSIA are shown in green

2.5.4 Cations

Ten discrete sampling events were conducted to determine aqueous concentrations of major cations along a five port horizontal transect at the base of the tank, as seen in Figure 2-11. As discussed in the section 2.5.2, samples were obtained from the saturated zone above the water table through the application of suction to the port. Following a 10 mL purge of the sampling lines to remove stagnant water, samples were filtered to 0.22 microns and collected in 12 mL falcon tubes. The samples were acidified to 2% nitric acid matrix for preservation and analysis. Analyses were performed on the Varian 725-ES Optical Emission Spectrometer by inductively coupled plasma – optical emission spectrometry (ICP-OES) at the University of British Columbia for concentrations of Al, Ca, Fe, K, Mg, Mn, Na and Si. Standards were prepared in the range of 0.1 to 100 ppm. The reported detection limit for the instrument is 0.2 ppm, although this may vary slightly from element to element and depending on the standards used (M. Soon, personal communication, Oct. 19 2016).

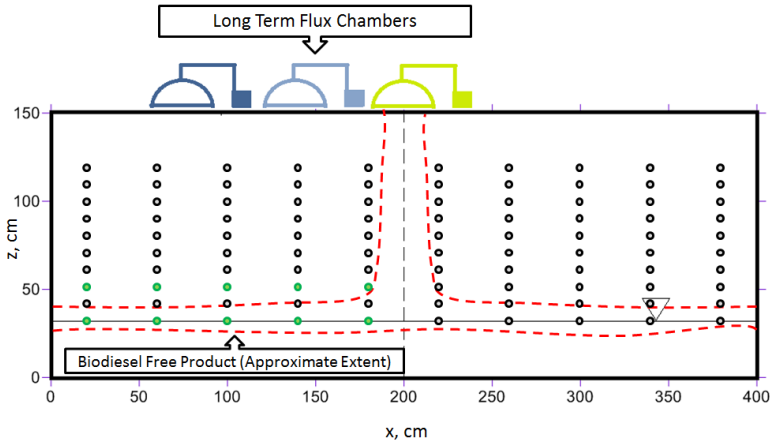

Figure 2-11: Ports sampled for analysis of cations, anions, pH and alkalinity

2.5.5 Anions

During three sampling events, ten samples were collected for determination of major anion concentrations in the sandtank water. The samples were collected in 12 mL falcon tubes and shipped to the Ministry of Environment's Environmental Sustainability and Strategic Policy Division (Knowledge Management Branch – Laboratory) for anion scans. The samples were analyzed for concentrations of F,

Cl, NO_2, Br, NO_3, PO_4, and SO_4. The sample analysis was difficult, particularly for bromide, due to the presence of a considerable organic background that interfered with the peak purity. A sample clean-up procedure was used in an attempt to remove most of the interference, but a clean ion chromatography peak for bromide could not be obtained for all samples (C. Dawson, personal communication, May 2 2016). Sampled ports are shown in Figure 2-11.

2.5.6 Alkalinity

Five 20 mL samples were collected from a horizontal transect 0.3 m from the base of the tank. Each sample was filtered using a 0.22 micron filter. To determine the alkalinity at each port, 10.3 mL of sample was pipetted into a container with the temperature maintained at 8 ^{o}C. The samples were measured into a beaker and titrated with a microburette containing 0.32 N H_2SO_4 to a pH of approximately 3.0, with constant stirring as titrant was added to the solution. A pH probe was used to continuously measure the solution pH until it dropped below pH = 3. The pH meter was calibrated using standards of pH 4.0 and 7.0. The pH was recorded at each titration step. The gran function inflection point method was then used to determine the alkalinity of the sample. Mathematically, the mL of titrant at the equivalence point was determined from the Gran function (Stumm and Morgan, 1981):

$$F1 = (V_0 + V) * 10^{-pH}$$

where V is the volume of H_2SO_4 added at that point in the titration, V_0 is the initial volume of sample, and pH is the measured pH at that point in the titration. The x-intercept of the best fit regression line for the data points leading up to the equivalence point was found by plotting the Gran function versus the volume of titrant added. This intercept was converted to the alkalinity of the solution in meq L^{-1} via the following equation:

$$Alkalinity = \frac{V * C_a}{V_0}$$

Where V is the volume of titrant added to reach the equivalence point in L, C_a is the concentration of the titrant in eq L^{-1}, and V_0 is the sample volume in L.

2.5.7 pH

Transects of pH measurements were conducted several times over the course of the experiment. Sampling lines were purged (10 mL) and 10 mL samples were collected into 12 mL falcon tubes from up to 2 horizontal transects (at 0.3 m and 0.5 m from the base of the sand tank). The pH-meter was calibrated at the beginning of the day with standards of pH 4, 7 and 10. The pH was determined immediately following collection of each sample to avoid impacts of degassing or reaction due to oxygen ingress. Ports sampled are shown in green in Figure 2-11.

2.5.8 Core Sampling for Microbiological Analysis

Before the start of the experiment, 208 samples were collected in 10 mL falcon tubes during sandtank construction to analyze microbial populations present during initial conditions. Samples were taken approximately every 40 cm in the x direction, every 25 cm in the y direction and every 20 cm in the z direction.

During the experiment, soil core samples were collected for microbiological analysis. Sampling was performed at three distinct time periods approximately 4 months, 8 months and 12 months after the beginning of the experiment. The sample locations were strategically selected to target regions of suspected enhanced microbial activity, or within confirmed methanogenic or methanotrophic zones, as evidenced by the sensor data. Care was taken to avoid taking cores in close proximity to ports and sensors.

Subsamples were extracted from duplicate soil cores collected from the three sampling locations along the length of the sand tank, as seen in Figure 2-12. Sampling locations spanned from background conditions to the center of the source zone. Each time, the cores were collected using a hand soil

sampler with a core catcher in 1 m long core sleeves. Sediment was removed from the upper 0.2 m of the sandtank to obtain a sample which spanned from the water table up through the vadose zone. Considerable compaction was caused by the core catcher and final sample lengths were between 0.3 m and 0.5 m long. The cores were labelled and frozen in dry ice immediately upon removal from the sand tank. They were placed in a -80 ^{o}C freezer for storage until the microbial analysis was completed.

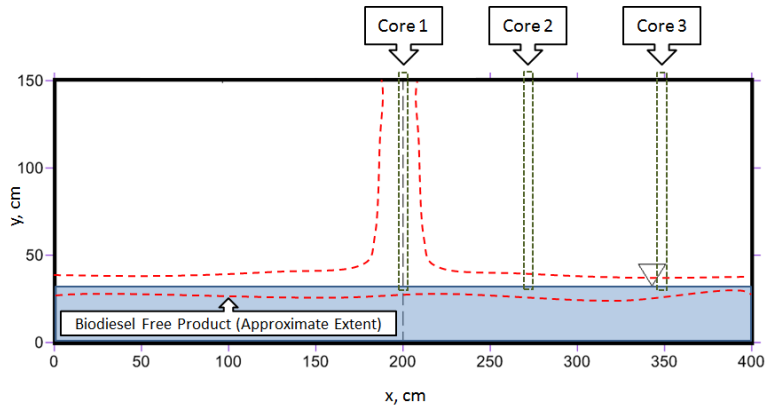

Figure 2-12: Approximate microbiological core sampling locations

The core analysis was completed as part of Ashley Arnold's M.Sc. degree in Microbiology and Immunology. The analysis will include processing for environmental DNA (eDNA) and downstream metatranscriptomic sequencing.

2.6 Reactive Transport Modeling

The existing reactive transport code MIN3P (Mayer et al., 2002) was used to quantitatively analyze and integrate data from the laboratory sand tank experiment, making use of water and gas chemistry data, sediment analysis results, and gas efflux data. The modeling was performed to provide a preliminary analysis of the experiment and to evaluate the origin of high concentrations of aqueous Fe and Mn in the sandtank water.

The model formulation includes variably saturated groundwater flow, diffusive multicomponent solute transport, diffusive gas transport, and biogeochemical reactions that can be defined through a database.

The reactive transport modeling was used to synthesize and extend the results of this laboratory experiment. Details on the model formulation and approach can be found in Mayer et al. (2002) and Mayer and MacQuarrie (2010). Details of the model set up and calibration can be found in Chapter 4.

3 Results and Discussion

Results from tests conducted on the sediments, aqueous chemistry and gaseous chemistry in the sandtank experiment are presented in this chapter. Results from the sediment tests completed by Klassen (2015) are interpreted with an emphasis on characteristics that may affect the results of the sandtank experiment.

The sandtank sampling and analysis was divided into two zones based on the type of samples obtained from the sampling ports: the saturated zone and capillary fringe, where aqueous samples were obtained, and the unsaturated zone, where gas samples were obtained. Aqueous samples were collected near the bottom of the tank, along horizontal transects at 30 cm, 40 cm and 50 cm from the base of the tank. Although some of these ports were above the water table (located at approximately 30 cm), this entire zone is here referred to as the saturated zone. At 60 cm and above, gas samples were obtained and this zone is referred to as the unsaturated zone. The chapter ends with a discussion attempting to synthesize the results from the two zones in the tank, and addressing the research questions outlined in Chapter 1.

3.1 Sediment Characterization

A constant head test was performed on the sediments to determine the saturated hydraulic conductivity; the average value obtained was 1.2×10^{-4} m s^{-1}. Percent abundance of Total Carbon (TC), Total Inorganic Carbon (TIC) and Total Organic Carbon (TOC) as well as several major element concentrations obtained from the multi-acid digestion with ICP-MS finish completed by Klassen (2015) are found in Table 3-1.

These elements were selected for analysis by ICP-MS; however, they do not sum to 100% (the elements for Sand-1 sum to 14.7% and Sand-2 to 15.8%) since there are several important elements missing, most importantly Si and O.

Table 3-1: Elemental abundance in Sand-1 and Sand-2 (Adapted from Klassen, 2015)

Abundance (%)	Sand-1	Sand-2
Total Carbon (TC)	0.056	0.084
Total Inorganic Carbon (TIC)	<0.01	<0.01
Total Organic Carbon (TOC)	0.056	0.084
Al	6.32	6.66
Fe	2.43	2.62
Na	2.12	2.27
Ca	1.92	2.12
K	0.91	1
Mg	0.69	0.79
Ti	0.21	0.26
P	0.031	0.04
S	<0.01	<0.01

Further elemental abundance results from the whole rock analysis completed by Klassen (2015) for the sediments are shown in Table 3-2.

Table 3-2: Elemental abundance results of trace elements for Sand-1 and Sand-2 (Adapted from Klassen, 2015)

Elemental abundance (ppm)	Sand-1	Sand-2	Elemental abundance (ppm)	Sand-1	Sand-2
Mn	458	512	Th	1.9	2.2
Ba	444	467	Se	<2	<2
Sr	291	325	Yb	1.2	1.3
Cr	204	320	Cs	<1	<1
V	72	82	Hf	0.87	0.93
Zn	37	43	Mo	0.83	1.01
Zr	29.8	30.8	Sb	0.83	0.6
Rb	24.2	25.9	Be	0.8	0.8
Ni	19.1	23.2	U	0.65	0.71
Ce	18.3	22	Sn	0.6	0.7
Cu	14	14.3	Tb	0.34	0.39
Ga	13.1	13.7	W	0.3	0.5
Y	11.5	12.6	Ta	0.24	0.32
Sc	9.9	10.8	Lu	0.18	0.19
La	9.1	10.9	Tl	0.18	0.18
Li	9	10	Ag	0.09	0.04
Co	7.9	8.9	Cd	0.08	0.11
Pb	6.2	7.6	Bi	0.06	0.06
Nb	3.6	4.5	Te	<0.05	<0.05
As	3	3	In	0.03	0.03

These results sum to 0.17% for Sand-1 and 0.20% for Sand-2. The qualitative XRD results are summarized in Table 3-3. Minerals are listed in order of abundance.

Table 3-3: XRD results from Sand-1 and Sand-2 (Adapted from Klassen, 2015)

	Sand-1	**Sand-2**
Common Minerals	Quartz Albite Albite disordered Dolomite Cronstedtite Magnetite Spinel Muscovite Cordierite Actinolite	Quartz Albite Albite disordered Dolomite Cronstedtite Magnetite Spinel Muscovite Cordierite Actinolite
Discordant Minerals	Illite Rhodochrosite Orthoclase	Epidote Franklinite

Some of the qualitative XRD results may be erroneous, as the diffraction pattern may have recorded irregularities in mineral texture, or particulates interfering with the X-Ray beam; therefore, uncertainty is left for the presence of the discordant minerals, especially (Klassen, 2015). The sands were expected to have similar mineral compositions; this was the case with the exception of a few discordant minerals with relatively low abundances. These include illite, rhodochrosite and orthoclase for Sand-1 and epidote and franklinite for Sand-2. Of these, only rhodochrosite is significant for the results of this experiment since it may provide a source of dissolved Mn^{2+} as it dissolves. Most of the sediments are composed of silicates, which are not very reactive. With the exception of rhodochrosite, the most important mineral in terms of chemical significance present in the sand is dolomite, which may provide pH-buffering capacity during the experiment. Magnetite is a crystalline iron oxide that may provide a source of dissolved Fe, but this is unlikely significant, since magnetite is recalcitrant to reductive dissolution.

The results of quantitative XRD analysis by Rietveld refinements are given in Table 3-4. These amounts represent the relative amounts of crystalline phases normalized to 100%.

Table 3-4: Quantitative phase analysis results (wt. %) (Adapted from Klassen, 2015)

Mineral	Ideal Formula	Sand 1	Sand 2
Quartz	SiO_2	43.9	44.9
Clinochlore	$(Mg,Fe^{2+})_5Al(Si_3Al)O_{10}(OH)_8$	1.9	1.1
Illite-Muscovite 2M1	$K_{0.65}Al_2[Al_{0.65}Si_{3.35}O_{10}](OH)_2$-$KAl_2[AlSi_3O_{10}](OH)_2$	4.2	3.1
Plagioclase	$NaAlSi_3O_8$-$CaAlSi_2O_8$	38.9	39.3
K-feldspar	$KAlSi_3O_8$	4.8	6
Ankerite-Dolomite	$Ca(Fe^{2+},Mg,Mn)(CO_3)_2$-$CaMg(CO_3)_2$	0.9	0.9
Actinolite	$Ca_2(Mg,Fe^{2+})_5Si_8O_{22}(OH)_2$	3.5	4.3
Marcasite?	FeS_2	0.4	
Titanite?	$CaTiSiO_5$	1.1	
Magnetite?	Fe_3O_4	0.3	0.4
Total		**99.9**	**100**

The EM/XRD Facility staff at UBC flagged marcasite, titanite and magnetite in Table 3-4, questioning the certainty of its presence (Klassen, 2015). The vast majority of the sediments are made up of quartz and plagioclase (82.8-84.2%) with an additional 10.2-10.9% of the bulk minerals made up of the silicate minerals illite-muscovite, K-feldspar and clinochlore. Again, a significant amount of ankerite-dolomite is present (0.9% for both sands) which is expected to provide pH- buffering capacity as well as a source of Fe^{2+}, Mg^{2+} and Mn^{2+} in solution. The bulk density of the sediments is 1.6 g cm^{-3}. As seen in Table 3-4, the composition of Sand-1 and Sand-2 is very similar; therefore any observable variation in hydrocarbon attenuation characteristics is not predicted. These two sands were mixed prior to filling the laboratory tank.

Amorphous mineral phases tend to dissolve more readily, and their dissolution may also affect the geochemical evolution within the sediments. The analyses performed on these sediments measured the quantities of crystalline minerals only. Therefore, amorphous minerals (such as amorphous iron hydroxide) present in the sediment samples could not be quantified using this method, although such

phases may be present at some amount. Sulfate reduction was not expected in this system due to the absence of SO_4^{2-}. This makes sense, since there was no source of SO_4 in either the Vancouver tap water or the sediments.

In the vadose zone, non-drainable water held by capillary forces is present in the pore space. Figure 3-1 shows the volumetric water content at four depths in the sandtank; 30 cm, 55 cm, 80 cm, and 95 cm from surface.

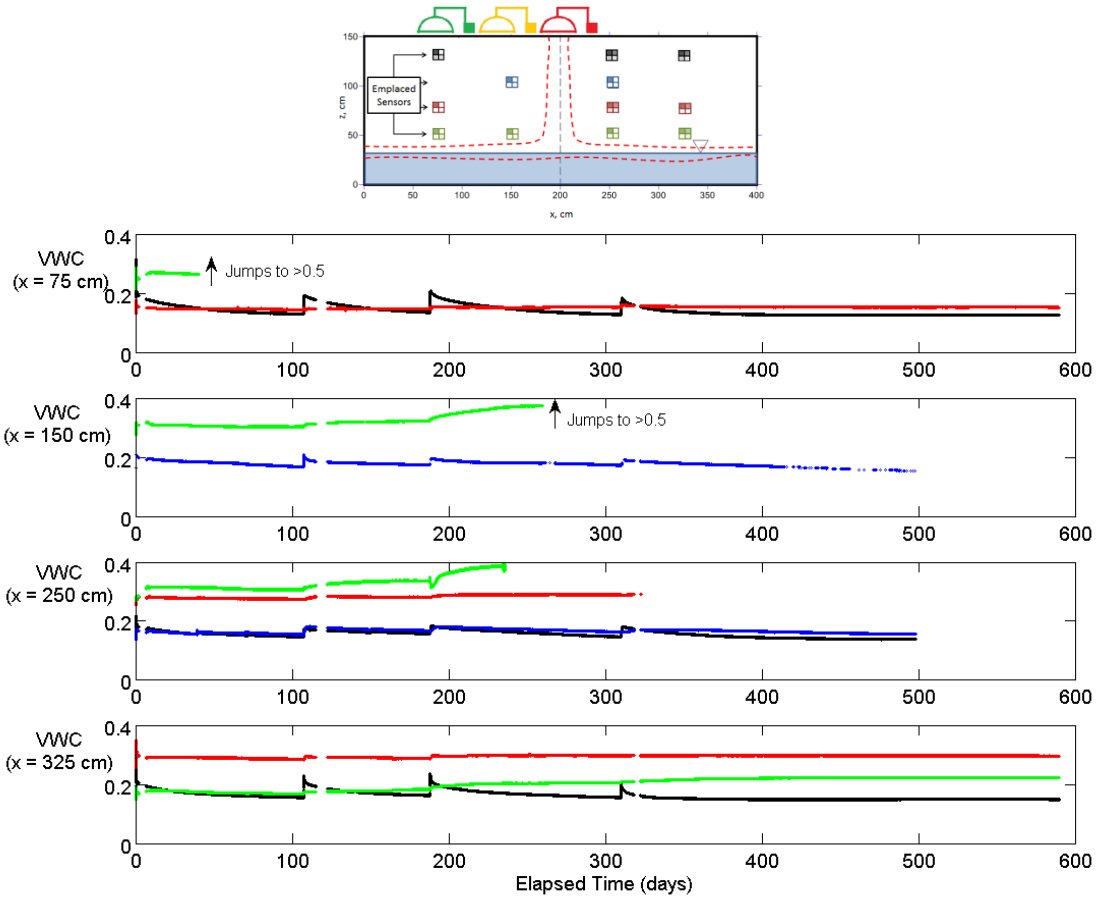

Figure 3-1: Volumetric water content with depth in sandtank from vertical transects at 75 cm, 150 cm, 250 cm and 325 cm. The green markers represent sensors at 55 cm, red at 80 cm, blue at 95 cm and black at 110 cm from the base of the tank.

Results from the sensors represented by the green markers at x = 75 cm and x = 150 cm were removed after they exhibited a sudden increase to unrealistically high values, exceeding porosity of 0.4. The sudden jumps in VWC are likely due to electronic issues, and the high water contents (>0.5) are

incorrect. Note that the unknown electronic problem which caused the large jump in sensor readings only affected two sensors (the sensors represented by the green markers at x = 75 cm and x = 150 cm).

In general, the volumetric water content in the sandtank near the surface typically ranged between 0.15 and 0.2 with higher values closer to the water table, as seen in Figure 3-1. Volumetric water content is affected by a variety of processes; it depends on soil hydraulic function parameters, elevation above the water table, and progress of evaporation.

The VWC data was somewhat difficult to interpret. In some cases, sensors located at the same depth showed different water saturation values and in other cases sensors at a lower depth in the sandtank showed lower VWC than sensors higher in the tank. These variations might be due to heterogeneities or differences in installation procedures. Although the magnitude of the sensor results was not entirely intuitive in all cases, the response to the precipitation events was very good for most sensors, with the strongest responses near the ground surface. As the pulse of water passed through the tank, a delayed spike in water content can be observed in most sensors. As expected, the sensor responses to the incoming front of moisture become more muted at depth. 280 days into the experiment, the sensor at x = 150 cm and z = 55 cm shows that the sediments reached saturation based on a sand porosity of approximately 0.4.

The infiltration velocity was estimated based on the arrival times of the water fronts at the sensors of various depths in a vertical transect. The calculated infiltration velocity from two sensors at x = 250 and z = 95 cm and z = 110 cm from the base of the tank (which provided the clearest response) was 9.0×10^{-6} m s^{-1}; however, there is considerable variability with depth and location in the sandtank. The infiltration velocity varied up to half an order of magnitude in either direction based on calculations from all sensors which provided a clear enough response to estimate the arrival time of the infiltrating water.

The VWC sensor data indicates that in the vadose zone, microbial communities can exist free of water stresses; water exists in the micropores, while the macropores are filled with gases (e.g. O_2, N_2, Ar, CO_2 and CH_4).Based on the observed volumetric water content measurements in the vadose zone, gases can move relatively freely; in particular, O_2 can ingress from the atmosphere across the top boundary into the vadose zone pore spaces. This is especially true due to the large estimated porosity of the sand. Gas migration through the vadose zone is affected by the gas content, i.e. the fraction of the pore space available for gas movement and by the tortuosity. An empirical relationship for gas tortuosity (Millington and Quirk, 1961) is given by:

$$\tau = \emptyset^{1/3} {S_g}^{7/3}$$

Where τ is the gas tortuosity factor, ϕ is the porosity and S_g is the gas saturation (equal to 1.0 for dry soil). Based on a porosity of 0.4 and a gas saturation of 0.5 (corresponding to a volumetric gas content = 0.2, which was derived from the measured VWC and porosity) in the upper vadose zone, the tortuosity is 0.15. The tortuosity factor is defined between 0 and 1 and is inversely proportional to the mobility of the gas in the porous medium (Clifford et al., 2006). These results indicate that, although tortuosity significantly inhibits gas exchange with the atmosphere, gas exchange still remains substantial due to large diffusion coefficients in the gas phase.

3.1.1 Biodiesel Redistribution

One objective of this work was to determine how the biodiesel would redistribute itself in response to the surface release. As shown previously in Figure 2-5, the biodiesel was applied to the central 0.5 m^2 of the sandtank. It infiltrated down to the water table, leaving free product on the sediments at residual saturation, and settled on the water table in a pool of free product. Due to its low viscosity, the 80 L of biodiesel was enough to form a pool which stretched the entire width and length of the sandtank. Along the center of the vadose zone, it is present in the sediments at residual saturation. The edges of the

smear zone are visible due to the Sudan IV in the biodiesel. Excavation into the top of the tank for the collection of the microbial cores also presented evidence of biodiesel held in the vadose zone, since the sediments in the center of the tank were oily and carried a strong odour of biodiesel.

A preliminary experiment was performed before the start of the sandtank experiment using sand packed into a small flow cell (60 cm x 6 cm x 60 cm). 330 mL of biodiesel dyed red with Sudan IV was applied to the center of the tank and migration was tracked visually. After two days, the biodiesel was no longer visibly migrating and had settled over a volume of sand of approximately 0.05 m^3. There was no pool at the base of the biodiesel smear zone; therefore we can calculate the residual biodiesel in the sand sediments. The residual biodiesel content in the sand is expected to be approximately 0.066 m^3 per m^3 of sediments, or a biodiesel saturation of 0.17 m^3 of biodiesel per m^3 of voids. Based on the results for the volumetric water content in the sediments, the sand in the vadose zone contains approximately 0.16 m^3 of water per m^3 of sediments above 55 cm; this was an estimate based on the average values from each of sensors in the upper section of the sandtank. A porosity of 0.4 was estimated for the sand, therefore there is approximately 0.17 m^3 of gas per m^3 of sediments in the biodiesel affected area of the vadose zone. Gas content in the region unaffected by the biodiesel release is approximately 0.24 m^3 of gas per m^3 of sediments. Effective tortuosities are therefore expected to vary somewhat from the estimate derived above, depending on location within the tank.

In the full scale sandtank, the average width of the biodiesel at residual saturation was 0.4 m. Assuming that the biodiesel is present at residual saturation for the depth of the vadose zone and width of the sandtank, there are approximately 31 L of biodiesel in the vadose zone.

At the water table, the hydrophobic LNAPL forms a pool of free product. Here, the biodiesel is expected to fill the pore space not already occupied by water (i.e. if we assume that the water content is 0.2 with a bulk porosity of 0.4, it implies a biodiesel content of approximately 0.2 in this region). The pool is

laterally extensive and ranges in thickness from 0.02 m to 0.08 m, which gives an estimated range of between 16 L and 64 L of biodiesel in the pool. Since only 80 L of biodiesel was applied, the upper range of this estimate is unlikely; however, slight fluctuations of the water table likely made the pool of biodiesel appear thicker than it is in reality. In addition, water saturations are likely somewhat higher in this region. Overall, the calculations suggest that approximately one third of the biodiesel was retained in the vadose zone, while the remainder forms a relatively thin pool across the water table in the entire tank.

The fact that the majority of the biodiesel is residing in a pool at the water table is expected to have implications on the observed rates of degradation, since saturated conditions limit O_2 access to the fuel to drive aerobic degradation.

3.2 Unsaturated Zone Results

The following sections describe the gas chemistry results obtained from the flux analysis, the emplaced sensors, and the gas chromatography work.

3.2.1 Flux Results

Figure 3-2 shows the flux results from the LICOR chambers at the surface of the sandtank. The flux from the center chamber located directly above the spill is represented by the red markers, and the fluxes represented by the orange and green markers were obtained from the chambers at 50 cm and 125 cm from the spill, respectively. The diamond markers show gas concentrations obtained in the ports along a horizontal transect at 70 cm from the base of the sandtank. The red diamonds are from a port near the center of the tank (180 cm from the edge) and the orange and green diamonds are from ports closer to the outside of the tank (100 cm and 20 cm from the edge, respectively). The blue bars represent the precipitation events, and the green bars represent the nutrient addition event.

Initially, CO_2 production increases quickly. This may be due to an abundance of highly biodegradable fractions of the fuel available at the start of the experiment, which is used up at early time. However, the decrease in CO_2 production coincides with the first precipitation event, suggesting that increased moisture content may have caused sediment saturation to increase beyond the ideal range for the microbes. The increased moisture may have limited O_2 access to some areas due to microscale heterogeneity, which would slow degradation. This interpretation is speculative in nature and difficult to verify; however, it may provide a suitable explanation for the correlation between scaling back of CO_2 production and the infiltration event. The CO_2 production never recovered to the levels seen at the start of the experiment.

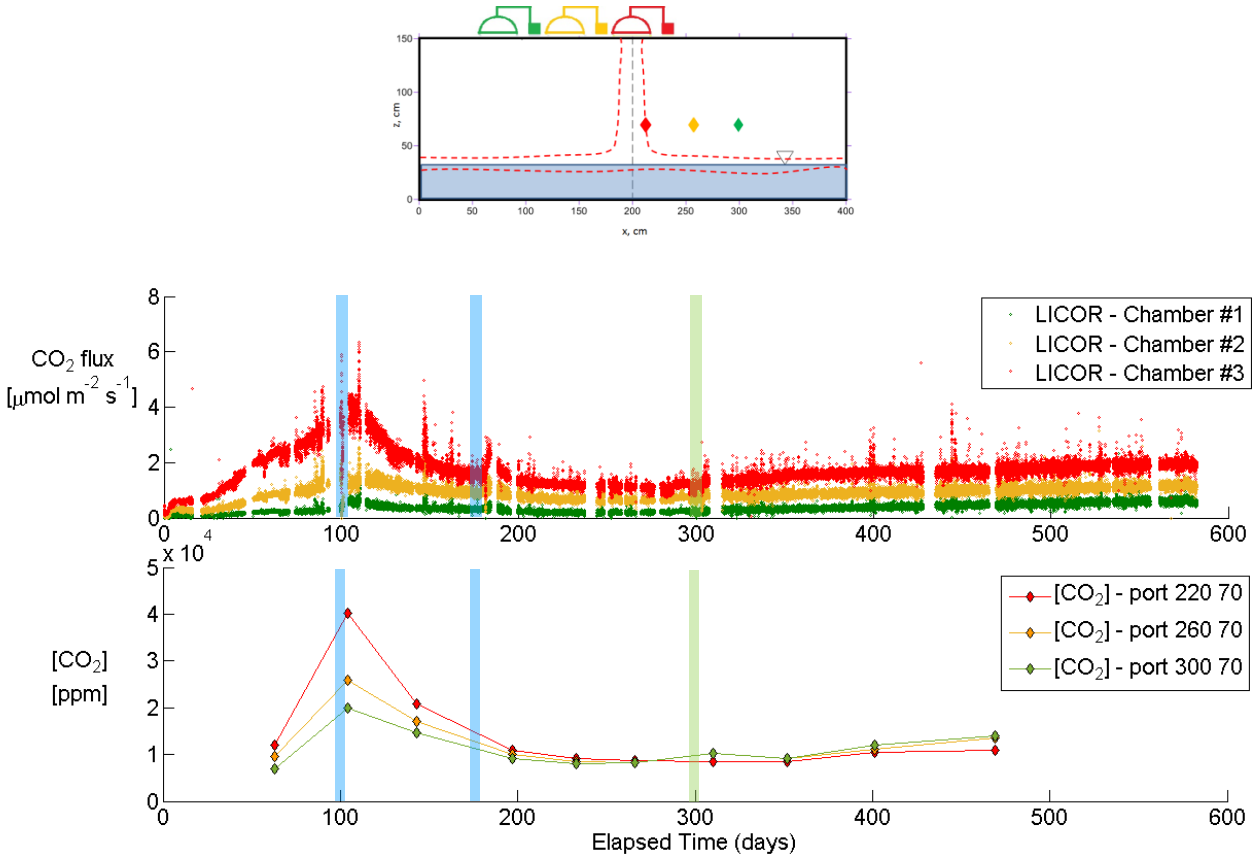

Figure 3-2: CO_2 efflux results from chambers 1, 2 and 3 (upper panel) and CO_2 concentration results from ports 0.8 m below each chamber (lower panel)

The small spike in CO_2 production during the second precipitation event is likely due to gas displacement from the sediment pores. The CO_2 flux seems to reach a quasi-steady state ranging between 0.5 and 2 µmol m^{-2} s^{-1}, with larger effluxes seen with increasing proximity to the spill zone. The time series efflux measurements, obtained under controlled conditions, serve as an indicator for the onset of microbial activity.

Figure 3-3 shows the CH_4 fluxes obtained from the LGR Greenhouse Gas Analyzer. The chambers are the same as those described for the CO_2 efflux results. The CH_4 concentrations obtained from ports in a vertical transect along the center of the sandtank (at 220 cm) are shown by the diamond markers.

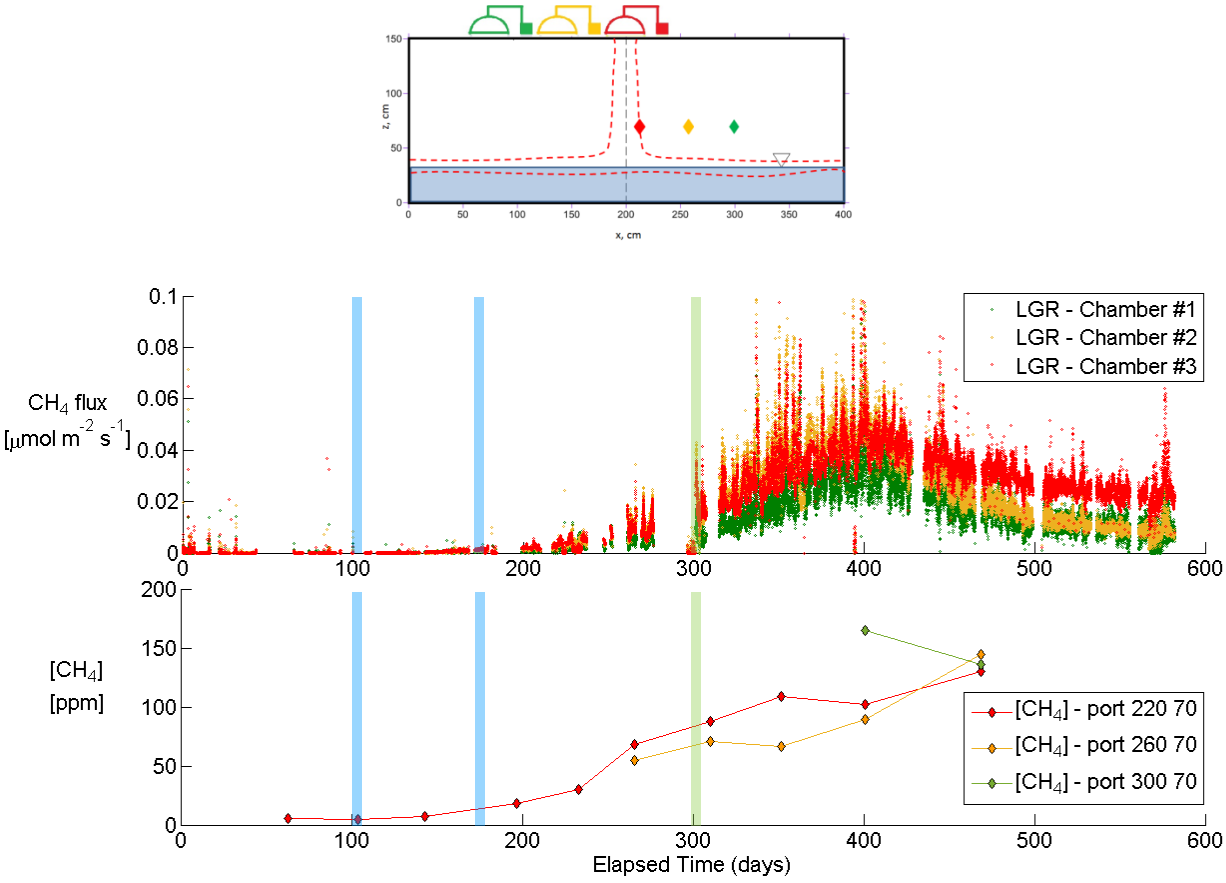

Figure 3-3: CH_4 efflux results from chambers 1, 2 and 3 (upper panel) and CO_2 concentration results from ports 0.8 m below each chamber (lower panel)

Measurable CH_4 effluxes started to occur around 200 days into the experiment. Similarly to the CO_2 flux, the CH_4 flux increased relatively rapidly then decreased after around 400 days. By the 590 day mark, the flux seemed to have reached a steady-state ranging between 0.01 and 0.03 µmol m^{-2} s^{-1}. Selected example calculations for CH_4 efflux based raw data from the LGR Greenhouse Gas analyzer can be found in Appendix A.6. Similar as for the CO_2 effluxes, the magnitude of the flux corresponds well with the distance between the chamber and the biodiesel spill zone. As in Figure 3-2, the blue bars represent the precipitation events and the green bars represent the nutrient application event. An increase of CH_4 production can be seen already before the nutrient application event; however, the largest CH_4 fluxes occurred after this event. CO_2 and CH_4 effluxes can be used as an indicator for biodiesel degradation in the sandtank. The maximum effluxes seen were $J_{CO2,max}$ = 5 µmol m^{-2} s^{-1} and $J_{CH4,max}$ = 0.08 µmol m^{-2} s^{-1}.

3.2.2 Sensor Results

Figure 3-4 shows the sensor results for O_2 and CO_2 concentrations in the sandtank. The blue bars indicate precipitation events and the green bars indicate the nutrient addition event. The maximum CO_2 concentrations observed in the tank are around 3%, with most of the sensors stabilizing between 0.5 and 2% near the end of the experiment. O_2 concentrations remained relatively close to atmospheric levels at most locations.

Similarly to the efflux results, CO_2 concentrations were low initially but gradually increased until the first precipitation event. After this precipitation event, there is a gradual decline in CO_2 concentrations, until the nutrient application event which produces a slight rise in CO_2 production. The O_2 concentrations mirror the CO_2 results; typically, increases in CO_2 are accompanied by decreases in O_2, and vice versa. Decreases in O_2 concentrations are less visible due to the relatively small decline in comparison to O_2 present in the atmosphere. The initial rise in CO_2 concentrations is likely attributable to microbial adaptation in the sandtank sediments, leading to increased biodegradation rates.

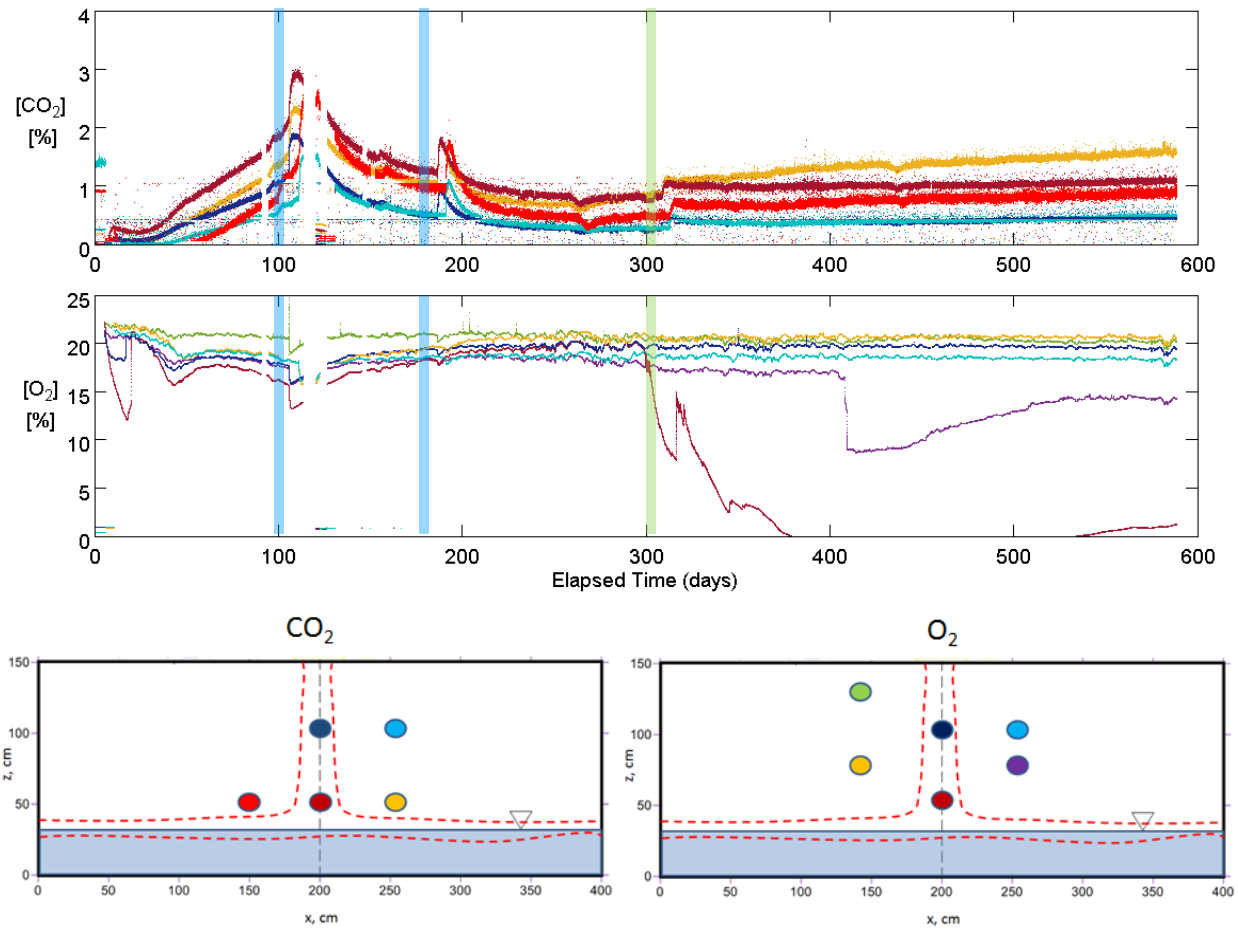

Figure 3-4: CO_2 and O_2 concentration results from the emplaced sensors in the sandtank.

The precipitation events clearly coincide with a spike in CO_2 concentrations likely related to reduced diffusion coefficients associated with higher moisture contents, resulting in entrapment of CO_2. It is unlikely that the decline in CO_2 production after the first precipitation event was caused by chemical changes, since the applied water was the same as the water initially placed in the tank. Both waters had undergone the same treatment with Nutrafin™. A more likely explanation is that the water covered the biodiesel and inhibited O_2 access, particularly to the pooled biodiesel. Decreased O_2 availability slows aerobic respiration and therefore decreases CO_2 concentrations in the vadose zone.

There are also minor temporary declines in O_2 concentrations in response to the recharge events, although all but two sensors remained above 15%, which is well in the oxic regime. The drop in O_2 concentrations is likely due to the infiltrating water, increasing moisture contents and limiting O_2 ingress.

The nutrient application, led to enhanced degradation activity, evidenced by the slight increase in CO_2 concentrations. However, the increase was relatively limited, and concentrations did not reach levels of the initial CO_2 production immediately prior to the first precipitation event. The nutrient application also coincided with substantial and rapid declines in O_2 concentrations at two of the lowermost sensors. The sensor located within the spill near the water table (represented by the dark red marker) showed decreasing O_2 concentrations immediately after the nutrient addition event; however, since this sensor was at 55 cm from the base of the sandtank. This behavior may be explained by water pooling around the sensor. Just after the 400 day mark, the sensor located offset from the spill at medium depth (x = 250 cm, z = 80 cm, represented by the purple marker) showed a pronounced drop from near atmospheric levels to around 10%. However, this behavior was not observed on the other side of the spill at the same depth (x = 150 cm, z = 80 cm, represented by the light orange marker). This asymmetrical behavior may be indicative of heterogeneities within the tank or a sensor malfunction at x = 250 cm, z = 80 cm. Since this is one of the lower sensors, it is also possible that water pooled around the sensor as it drained down following the nutrient application event, although this is less likely, since the drop occurred more than 100 days after the nutrient application and neighboring CO_2 and VWC sensors do not show any drastic changes.

Other short term peaks and fluctuations in observed gas concentrations may be caused by sample collection nearby or by normal fluctuations in barometric pressure in the laboratory. These peaks may also be caused by sensor noise.

3.2.3 Vadose Zone Gas Concentrations

Time series results of N_2, O_2, and Ar concentrations are plotted in Figure 3-5, Figure 3-6 and Figure 3-7, respectively.

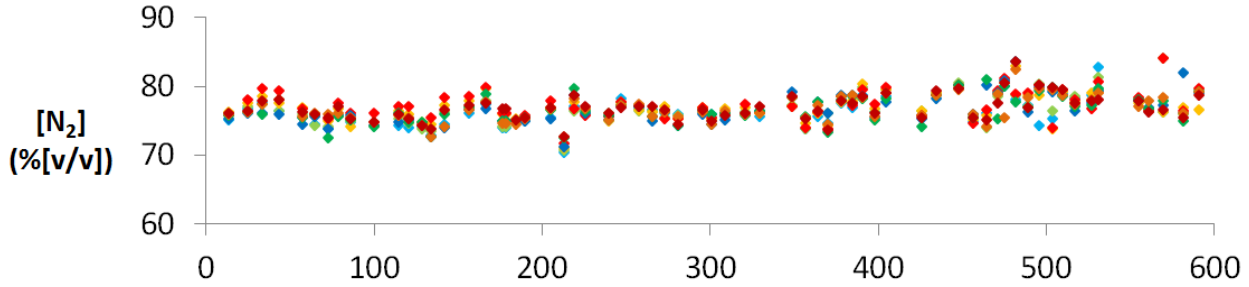

Figure 3-5: Nitrogen gas concentrations vs. elapsed time in days obtained via weekly Varian GC measurements

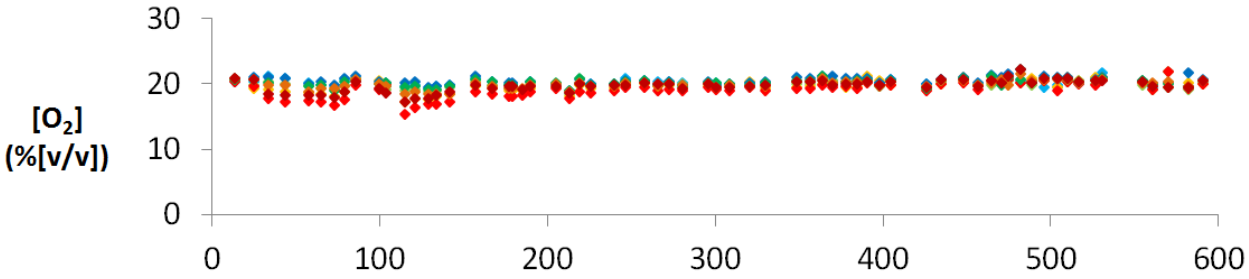

Figure 3-6: Oxygen gas concentrations vs. elapsed time in days obtained via weekly Varian GC measurements

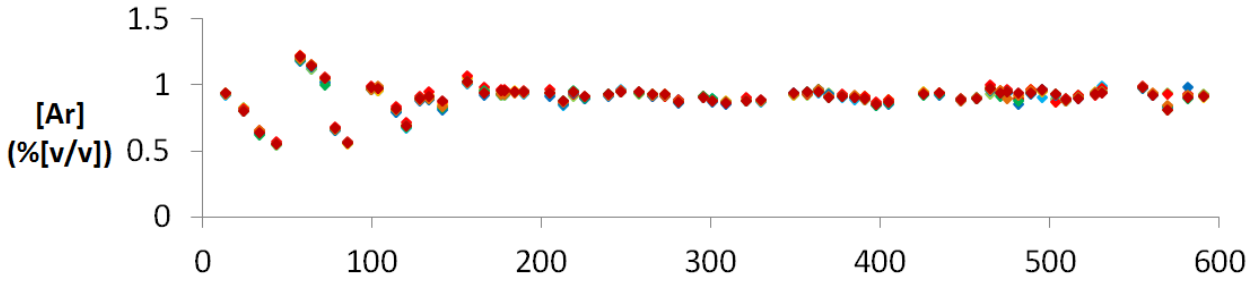

Figure 3-7: Argon gas concentrations vs. elapsed time in days obtained via weekly Varian GC measurements

There is some noise in the results; however, the most abundant gases (N_2 and O_2) remain relatively stable over the course of the experiment. The instability seen in the Ar concentrations near the start of the experiment is likely due to calibration issues with the GC (i.e. poor separation of Ar and O_2 chromatographs), as this instability is not seen in the other results. Calibration issues seem likely because the errors in the Ar results from all port locations follow the same pattern, independent of

variations in the other gas concentrations. However, the Ar/O_2 separation problems do not affect the interpretability of the data. The darker colours represent the lower horizontal transect (70 cm from the base of the tank) and the lighter colours represent the horizontal transect 100 cm from the base. The ports near the center of the sandtank are shown in red, and the orange, blue and green sensors are 60 cm, 100 cm and 140 cm from the center of the sandtank, respectively. The fact that Ar and N_2 concentrations remained close to atmospheric conditions throughout the experiment indicates that advective gas transport in the sandtank was negligible over the duration of the experiment.

CO_2 and CH_4 results are plotted in Figure 3-8. Each pair of graphs shows results from a two-point vertical transect 180 cm, 140 cm, 100 cm and 60 cm from the edge of the sandtank. GC results show significant variations in CO_2 concentrations, but the magnitude of the concentrations remained stable over the course of the experiment and was consistent with sensor data (Figure 3-2). All of the ports had CH_4 concentrations below detection limit for the initial part of the experiment. However, the onset of methanogenesis can clearly be seen approximately 250 days into the experiment with the highest concentrations seen towards the center of the tank and in proximity to the water table.

180 cm from sandtank edge:

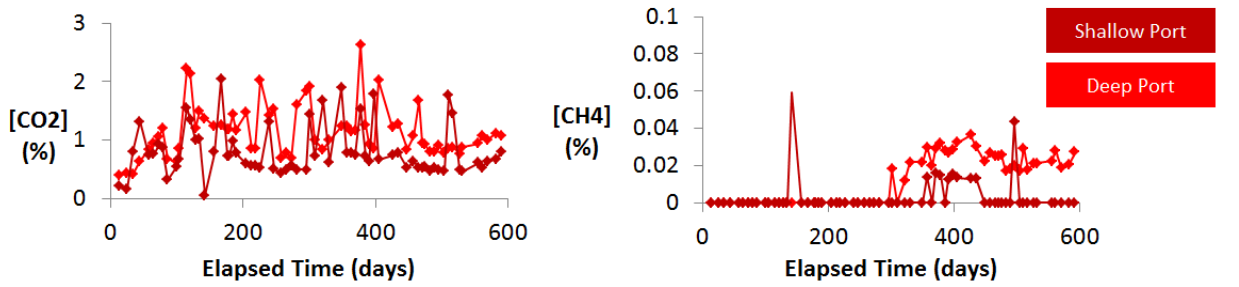

140 cm from sandtank edge:

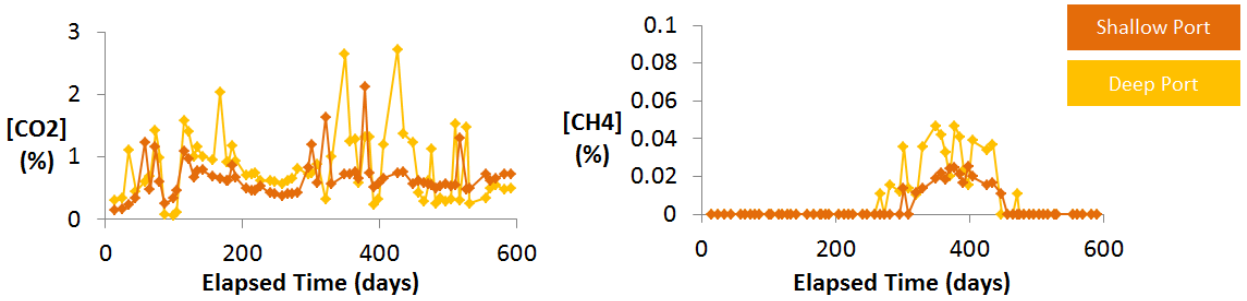

100 cm from sandtank edge:

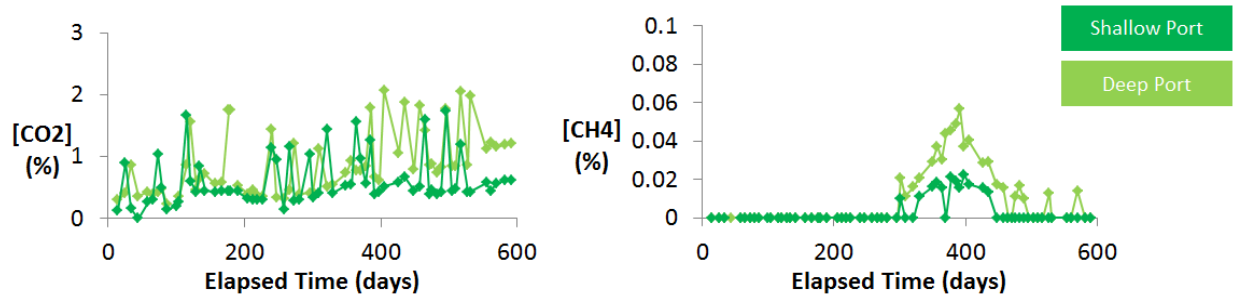

60 cm from sandtank edge:

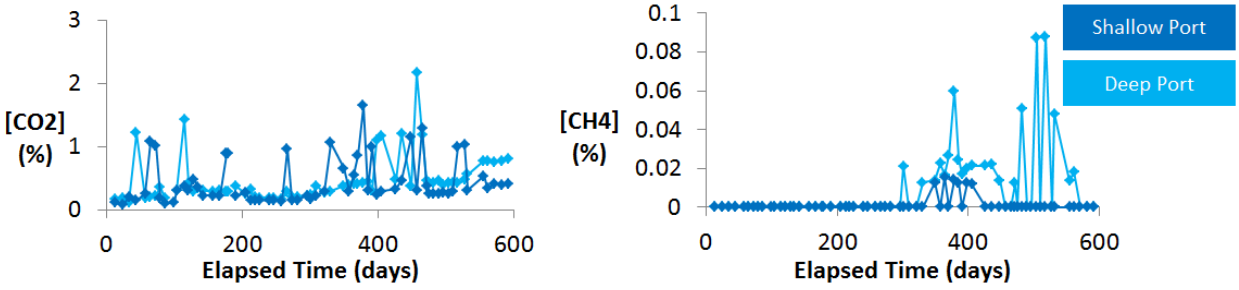

Figure 3-8: CO_2 and CH_4 results from all ports in the weekly Varian GC analysis

3.3 Saturated Zone Results

3.3.1 pH and Alkalinity Results

Five samples were taken along a horizontal transect on one half of the sandtank and alkalinity titrations were performed 407 days after the start of the experiment. The alkalinity is the acid-neutralizing capacity of the water, and can be defined as the sum of the titratable bases. The results of these titrations are shown in Table 3-5.

Table 3-5: Alkalinity results from ports in a horizontal transect 30 cm from the bottom of the tank

Port	20-30 (edge)	60-30	100-30	140-30	180-30 (center)
Alkalinity (mg L^{-1} as $CaCO_3$)	937	1406	3774	3329	2964
Alkalinity (meq L^{-1})	18.7	28.1	75.4	66.5	59.2
Sample Volume (mL)	10.3	10.3	10.3	10.3	10.3
H_2SO_4 to equivalence point (mL)	0.603	0.904	2.427	2.141	1.907
Initial pH	6.61	6.72	6.43	6.1	4.87
pH at inflection point of Gran Function	3.4	3.4	3.76	3.64	3.32

The Gran function is expected to be a straight line with a sharp inflection point at the x-axis. Unfortunately, the results of these titrations appear to be creating smooth curves. This is likely due to the presence of organic acids which contribute to alkalinity and effectively increase the alkalinity measurements. The total alkalinity is defined as the equivalents per litre of strong acid required to titrate a solution to a pH of 4.5; at this pH, all carbonate species become completely protonated (Lower, 1999). Typically, carbonate alkalinity contributes most significantly to total alkalinity. However, in this experiment there are other contributors, which causes the alkalinity of the system to be larger than would be expected based on the pH measurements. Thus, the pH at the inflection point of the Gran Function is lower than 4.5 for the sandtank samples; the inflection point pH ranges between 3.3 and 3.8 in the five ports measured. The anion scan results (section 3.3.4) also displayed interference with one

(or several) organic contaminant(s). Table 3-6 shows the alkalinity for each port, which would have been obtained had the titration been stopped at pH = 4.5.

Table 3-6: Theoretical alkalinity if titration had stopped at pH = 4.5

Port	20-30 (edge)	60-30	100-30	140-30	180-30 (center)
Alkalinity (mg L^{-1} as $CaCO_3$) for inflection point method	937	1406	3774	3329	2964
Alkalinity (mg L^{-1} as $CaCO_3$) for pH = 4.5	700	1150	2301	2052	684

The difference between the alkalinity at pH = 4.5 and the alkalinity measured using the inflection point method is largest in the center of the sandtank, and smallest near the edge. This matches the trend seen in the volatile fatty acid (VFA) results, where concentrations increase toward the center of the sandtank.

The sandtank water contained relatively high concentrations of volatile fatty acids (VFAs) as discussed in section 3.3.2, affecting the alkalinity measurements. The pKa of acetate is 4.76, the pKa of propionate is 4.88 and the pKa of butyrate is 4.82. These pKas explain why, toward the center of the tank, where there is a higher concentration of VFAs, the Gran function plot seems to form more of a curve than a straight line because of the buffering capacity of these and other organic acids, which have not been included in the suite of aqueous analyses. All Gran function plots can be found in Appendix A.7.

The pH of the samples was measured several times over the course of the experiment and the results are shown in Figure 3-9. Although all samples were obtained from the saturated zone, a distinction is made between samples obtained from above the water table (in the capillary fringe) and below the water table. The circles represent samples that were taken from deeper in the sandtank (at 30 cm from the bottom), and the diamonds represent samples that were taken from above the water table (at 50 cm from the bottom). It was possible to obtain samples from above the water table because saturation in ports was sufficient to extract water samples via gas-tight syringe.

The pH decreases steadily over the course of the experiment, particularly near the center of the tank where the lowest observed pH was found to be 4.5 in the capillary fringe. Note that the alkalinity measurements were taken from the bottom row of ports where the pH measurements were taken (the circles in the horizontal transect 30 cm from the bottom of the tank).

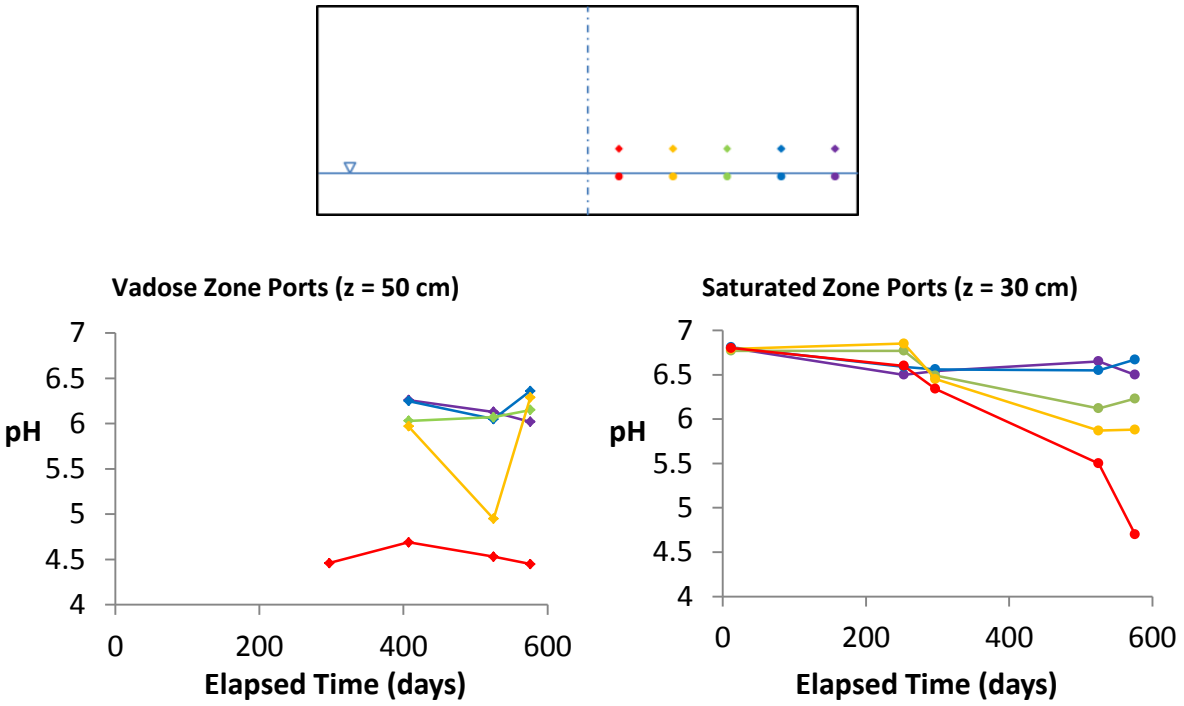

Figure 3-9: pH results over the course of the experiment. Ports sampled are shown in the schematic legend

The pH is an excellent indicator for microbial health, and it may change rapidly in response to changes in microbial growth and behaviour. A stable pH indicates system equilibrium and stability. A falling pH can point toward acid accumulation and instability (Golueke, 2002). In a typical anaerobic digestion system, gas production is the only parameter that can diagnose digester instability faster than pH. The range of acceptable pH for the bacteria participating in methanogenesis is from 5.5 to 8.5 (Golueke, 2002). Most methanogens function well in a pH range between 6.7 and 7.4, and optimally between 7.0 and 7.2.

Acid accumulation may also have affected the rate of biodiesel degradation over the course of the experiment. The sudden influx of 80 L of biodiesel likely caused bacteria to thrive, producing high

concentrations of organic acids and carbonic acid, thus lowering the pH to below 5.0 (a level lethal to methanogens). Methanogens are responsible for consuming acidity, so this creates a positive feedback loop as a declining methanogen population will in turn lead to further acid accumulation. The ankerite-dolomite identified in the sediment characterization study would be expected to provide pH-buffering capacity, but the dissolution rate of dolomite may not have been fast enough to prevent the runaway acid generation, or depletion of this phase might have occurred. According to Gautelier et al. (1999), the steady state dolomite dissolution rate at a pH of 4.6 and temperature of 25 degrees C is 1.20×10^{-6} mol m^{-2} s^{-1}. A coarse sand is expected to have a specific surface area per bulk volume of approximately 10^{-3} m^2 cm^{-3} (Bell, 2016) and in this case the dolomite surface associated with the sand would be approximately 0.9% of that value. This gives a dissolution rate for dolomite of 1.1×10^{-8} mol cm^{-3} s^{-1} in the area of the sandtank with the lowest pH and in saturated region. This rate corresponds to 4.3×10^{-6} mol L^{-1} H_2O s^{-1}. This dissolution rate is substantial and typically leads to quasi-equilibrium conditions in sediments (e.g. Mayer et al., 2002). It is therefore more likely that dolomite depletion, or possibly passivation led to the development of low pH-conditions in the sandtank.

Temperature is another important parameter to maintain in a desired range for biodegradation. Anaerobic bacteria can survive in a wide range of temperatures, from freezing to 70°C, but thrive within two ranges: from 25°C (77°F) - 40°C(104°F), the mesophilic range, and from 50°C (122°F) to 65°C (149°F), for thermophilic bacteria. Figure 3-10 shows the temperature as reported by the MPS-2 sensors distributed at various depths in the sandtank. There were some fluctuations; however, the temperature remained fairly close to 20 degrees for the duration of the experiment. Sensors near the bottom of the sandtank (at 55 cm) reported temperatures approximately 1 degrees C warmer than those near the top (at 120 cm), with the largest temperature differences occurring during times of fast degradation (i.e. at the start of the experiment up to the precipitation event at 100 days, and after the nutrient addition event at 303 days).

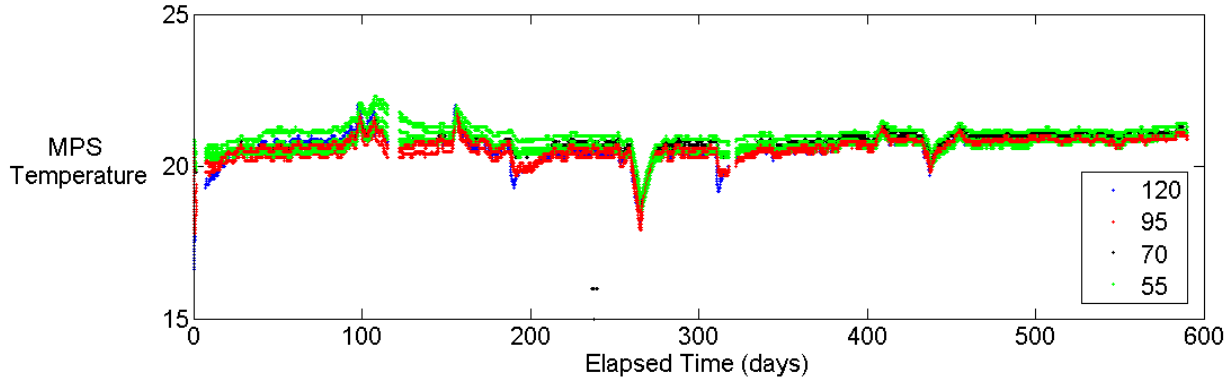

Figure 3-10: Temperature results from the emplaced sensors in the sandtank

The temperature data provides some confidence that the sensors were working normally for the duration of the experiment; if the sensor data logging frequency was too fast, sensor overheating can affect the temperatures in the surrounding experiment and affect experimental evolution. Here, the temperature increases at depth correlate with times of maximum degradation which suggests that changes in temperature are related to microbial activity, and are not correlated to the sensors generating heat over the course of the experiment.

3.3.2 Volatile Fatty Acids (VFAs)

VFA samples were collected in three horizontal transects at 30 cm, 40 cm and 50 cm from the base of the tank. Samples could only be collected at the ports where water content was sufficient to extract enough water for sampling via gas-tight syringe (50 cm from the base of the tank and below). Samples were analyzed for concentrations of acetic, propionic, and butyric acid. Overall, VFA production in the water-saturated region of the tank was high.

Figure 3-11 shows the concentrations of acetic acid in the sandtank over the course of the experiment from various ports as shown on the schematic legend. Acetic acid concentrations reached a maximum value of 2906 ppm in the centre of the sandtank at 30 cm from the base (the lowest port). This makes sense, since it is most likely that anoxic conditions would develop in this area; however, measurable amounts of acetic acid were detected in all sampled ports throughout the duration of the experiment.

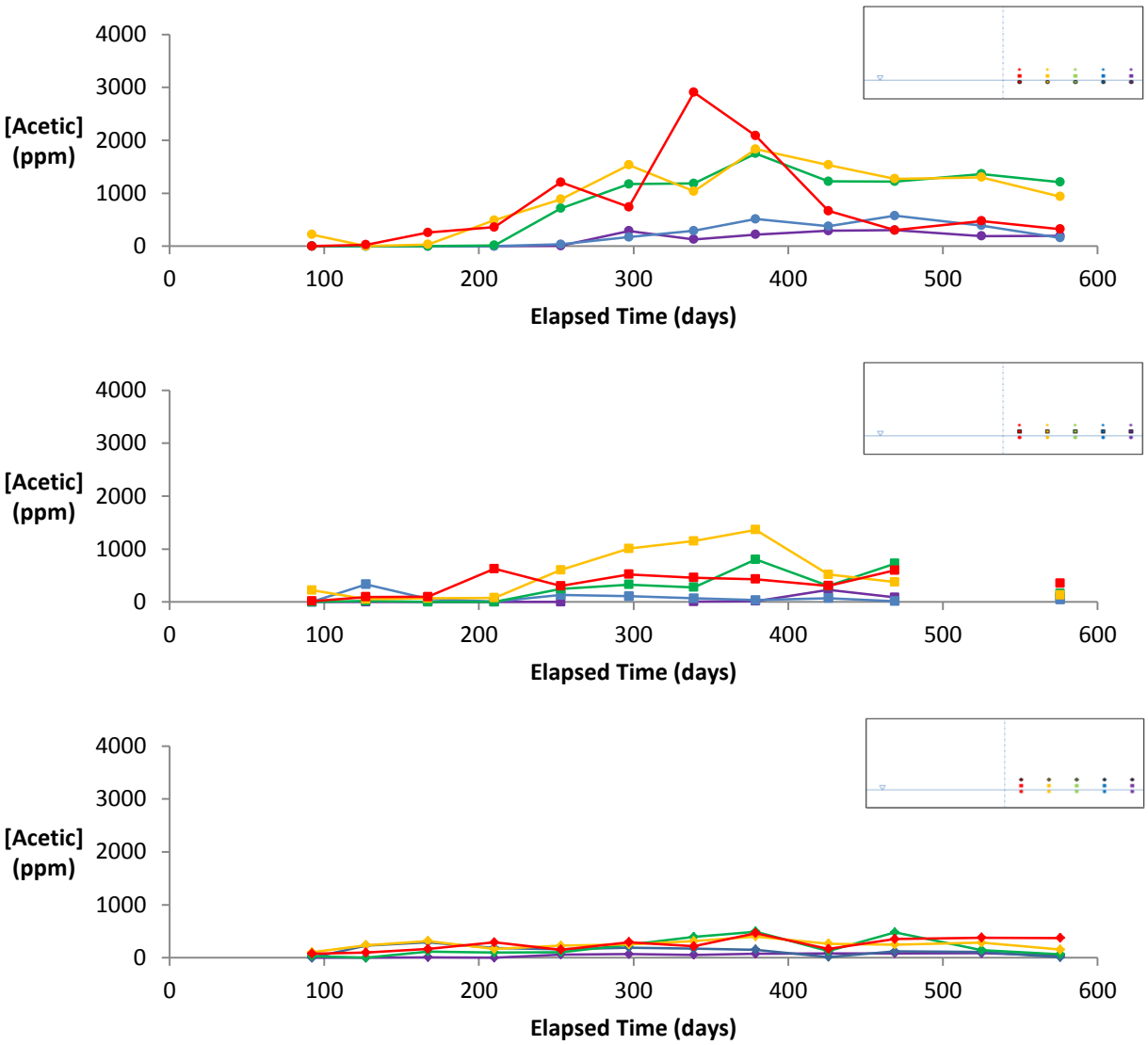

Figure 3-11: VFA results for acetate over the course of the experiment at horizontal transects of 30 cm, 40 cm and 50 cm from the base of the sandtank. Ports sampled are shown in the schematic legend

Concentrations of acetic acid increased significantly following the application of ammonium chloride and potassium orthophosphate at 303 days into the experiment. Maximum concentrations were observed in all ports between 300 and 400 days into the experiment. After 400 days, the concentrations stabilized back to the values measured before the nutrient application, presumably when the supplementary nutrient supply had been exhausted.

Figure 3-12 shows the concentrations of propionic acid over the course of the experiment.

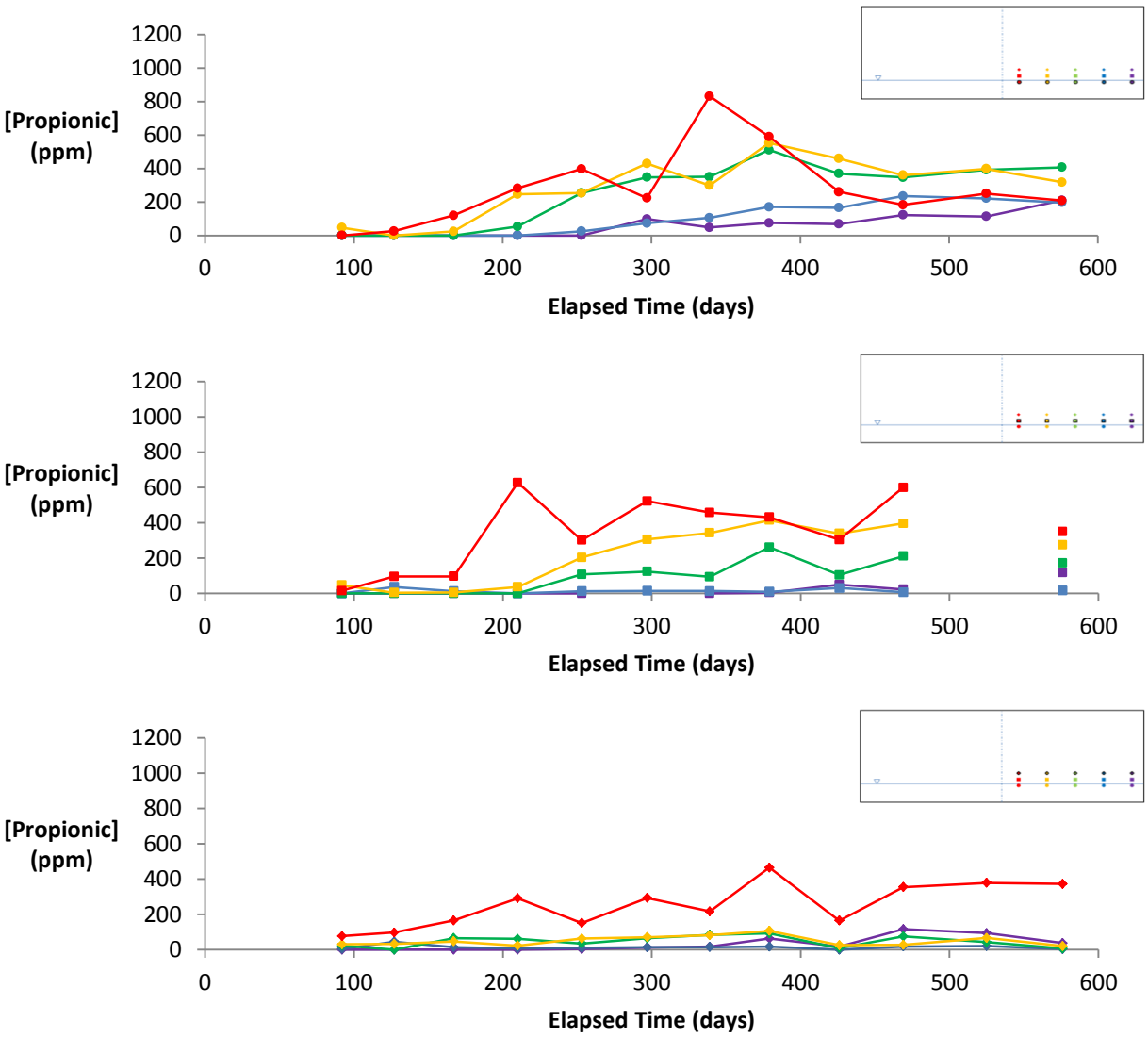

Figure 3-12: VFA results for propionate over the course of the experiment at horizontal transects of 30 cm, 40 cm and 50 cm from the base of the sandtank. Ports sampled are shown in the schematic legend

Concentrations of propionic acid were much lower than acetic acid concentrations; however, concentrations were still relatively high with a maximum concentration of 831 ppm in the center bottom port. The concentrations were similar between the two lower transects (at 30 cm and 40 cm) unlike the acetic acid concentrations, which were much higher at 30 cm. Concentrations in the vadose zone (at 50 cm from the bottom) were similar in all ports except the center port at 180 cm, which presented consistently higher propionic acid concentrations.

Figure 3-13 shows the concentrations of butyric acid over the course of the experiment.

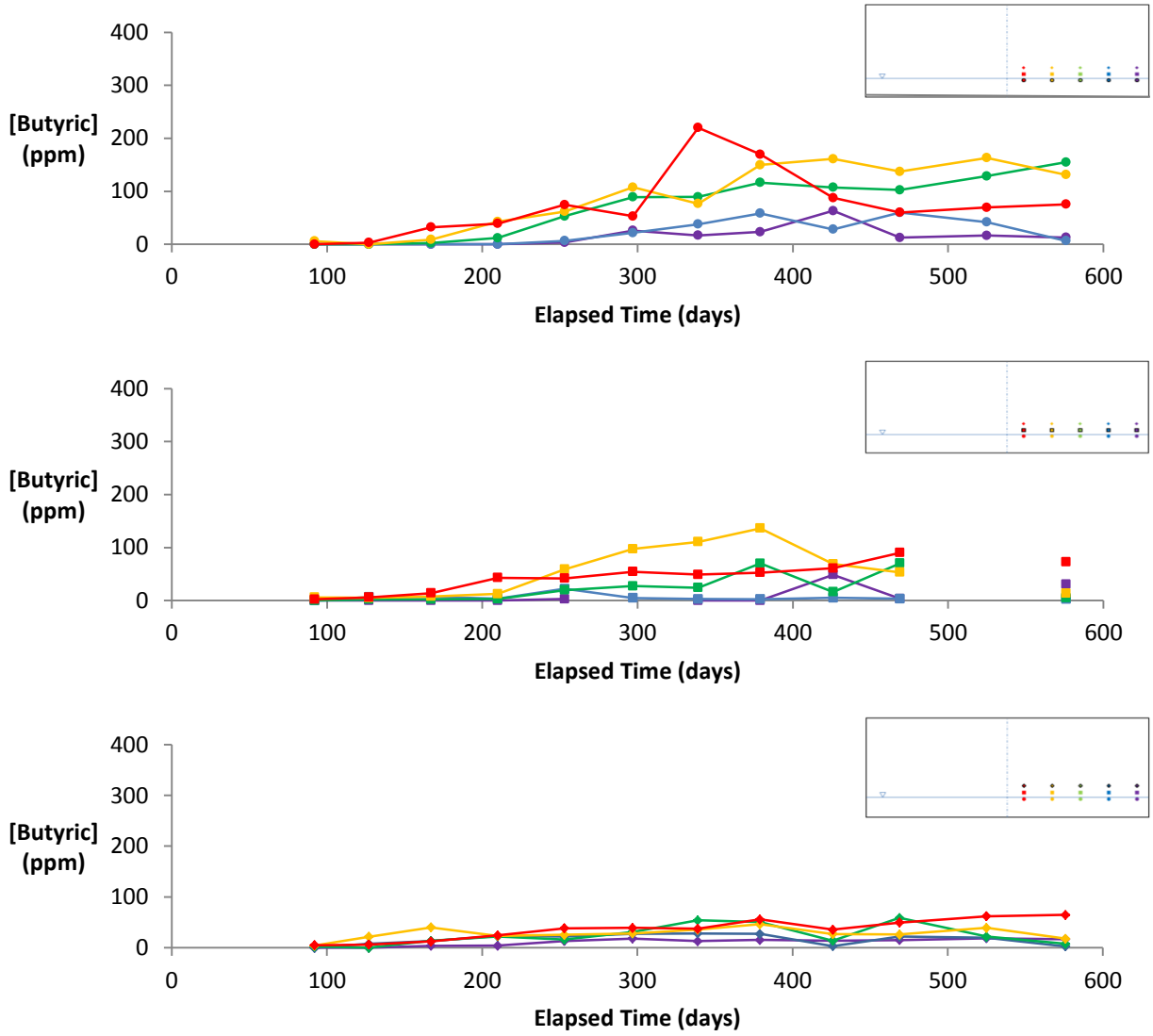

Figure 3-13: VFA results for butyrate over the course of the experiment at horizontal transects of 30 cm, 40 cm and 50 cm from the base of the sandtank. Ports sampled are shown in the schematic legend

Butyric acid concentrations were lower than propionic acid concentrations, with a maximum concentration of 220 ppm observed in the centre bottom port.

Overall VFA production in the lower portion of the sandtank was very substantial. Acetate, propionate and butyrate formation are acid generating reactions; however, the very low pH values seen in the center of the sandtank are likely not only caused by these reactions. The high acid generating reactions are also occurring in the unsaturated zone. The biodiesel undergoes aerobic degradation in the vadose

zone which generates approximately two moles of H^+ per mole of CO_2. The acidity generated in these reactions appears to be diffusing downward into the saturated zone and causing lower pH values in the saturated zone. Acetate, propionate and butyrate dissociate to weak acids and therefore they may provide additional pH-buffering capacity if they are present in the deprotonated state and acidity enters the system from the unsaturated zone. However, this will depend on whether or not the pKa of the fermentation reactions are higher than the pKa of H_2CO_3/HCO_3^-.

3.3.3 Cations

Figure 3-14 shows the cation concentrations of calcium, magnesium, potassium, sodium, iron, manganese and aluminum in the sandtank through time. The plots in Figure 3-14 were created from ports sampled in the saturated zone of the sandtank, in a horizontal transect at 30 cm from the bottom of the tank.

Increased concentrations of Ca and Mg are most likely due to carbonate mineral dissolution occurring in the sandtank. Biodiesel from used cooking oil may contain small concentrations of Mg and Ca; however, the combined total cannot exceed 5 ppm according to ASTM D6751 (Sanford et al., 2009). Mineral phases in the sand grains which contained Ca and Mg were fairly numerous: Ca and Mg may have resulted from the dissolution of dolomite or possibly also actinolite, and Mg was found in cordierite and spinel. These mineral phases are relatively stable, with the exception of dolomite. The reactivity of dolomite is expected to increase in response to acid generation in a system particularly below a pH of 5 as is the case in the center of the sandtank. Generally, the release of metals correlates well with the evolution of pH towards lower values (Figure 3-9).

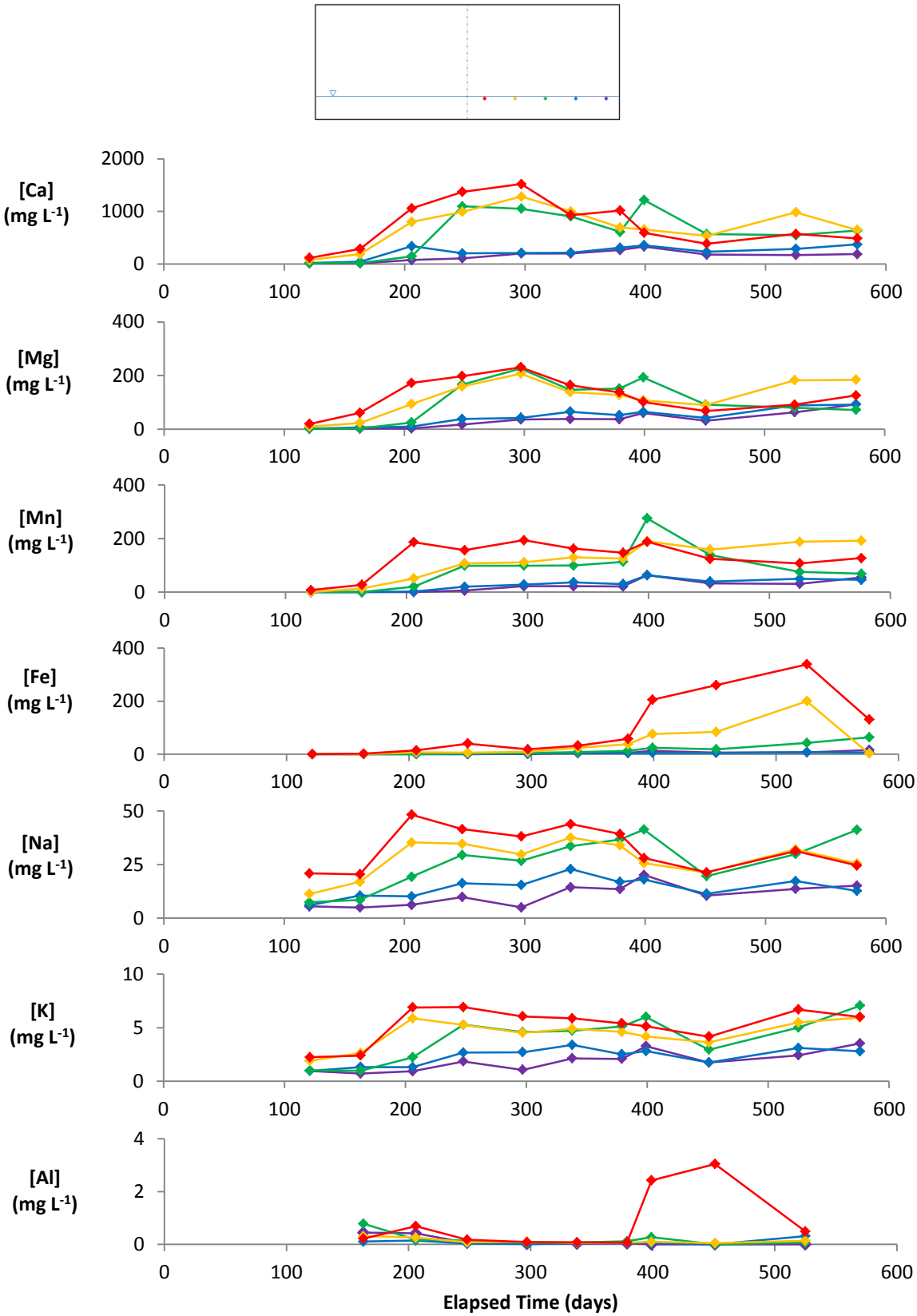

Figure 3-14: Elemental concentrations of cations: Ca, Mg, Mn, Fe, K, Na, and Al

K and Na concentrations increased slightly – this may be attributable to ion exchange reactions on the sediment grains due to the increased Ca and Mg. Albite dissolution may have led to an increase in concentrations of Na. Many of the silicate minerals contained K and Na including illite-muscovite, plagioclase and potassium feldspar. These minerals are fairly crystalline phases; however, the decrease in pH may have led to some dissolution contributing to the slight increase of dissolved concentrations of K and Na.

Fe and Mn concentrations were elevated in the saturated zone. Mn concentrations increased after the second precipitation event, at around 200 days, to 200 ppm and remained relatively stable for the duration of the experiment. In particular, Fe concentrations increased after the nutrient application event 303 days into the experiment to 338 ppm. The concentrations of these elements may be increasing in the water due to the reductive dissolution of Fe- and Mn-hydroxides. Fe and Mn reduction may have become dominant in areas of the sandtank where O_2 became depleted (i.e. in the saturated zone near the water table where the biodiesel is pooling). This is particularly likely for Fe, since the higher concentrations are strongly correlated with the nutrient addition event and less strongly correlated with pH values. Fe and Mn may also be produced via ankerite dissolution. Aerobic degradation in the vadose zone and the generation of organic acids in the saturated zone may have lowered the pH of the water and enhanced dissolution of the ankerite-dolomite phase. Ankerite dissolution is expected in areas where the pH decreases. Some other phases, such as magnetite, may contain Fe; however, such phases are very stable phases and the dissolution kinetics likely prevented these phases from becoming major sources of dissolved Fe.

Si-concentrations hovered around 40-50 mg L^{-1}. According to PHREEQCi simulations, quartz reached saturation at all ports, however, SiO_2 (am) remained just undersaturated (approximately -0.5). Si solubility was likely limited by the formation of SiO_2 and/or clays.

Al concentrations remained relatively low throughout the duration of the experiment, although there was a clear spike in the center port at 399 days where concentrations increased to 3 ppm. According to PHREEQCi simulations, Al-silicates such as kaolinite and halloycite became supersaturated for all ports across the horizontal transect at 30 cm; therefore it is possible that Al-silicate dissolution was occurring locally in the saturated zone (to a lesser extent), with Al solubility controlled by Al-hydroxide phases and clays.

The pH in the central port at 399 days (during the Al^{3+} spike) was 5.5, which would help explain the elevated Al concentrations; Al^{3+} solubility begins to increase below a pH of 6 and increases significantly below a pH of 5. It is possible that the dissolution of Al-silicates was occurring in the more acidic vadose zone waters, leading to the downward diffusion of Al and Si into the saturated zone. At 576 days into the experiment, the center vadose zone port at 50 cm had a pH of 4.7 and an Al concentration of 13.6 ppm, supporting this argument

PHREEQCi simulation results for a batch reaction at each individual port showed saturation indices of gibbsite increasing slightly in most ports to between 1 and 2.65. This may form as a secondary phase and control Al solubility. $Al(OH)_3(am)$ remained undersaturated.

3.3.4 Anions

Anion scans were completed on aqueous samples from 10 ports in the sandtank at 399, 525 and 576 days after the start of the experiment. The results of Cl^-, NO_3^- and SO_4^{2-} in the tank are plotted in Figure 3-15.

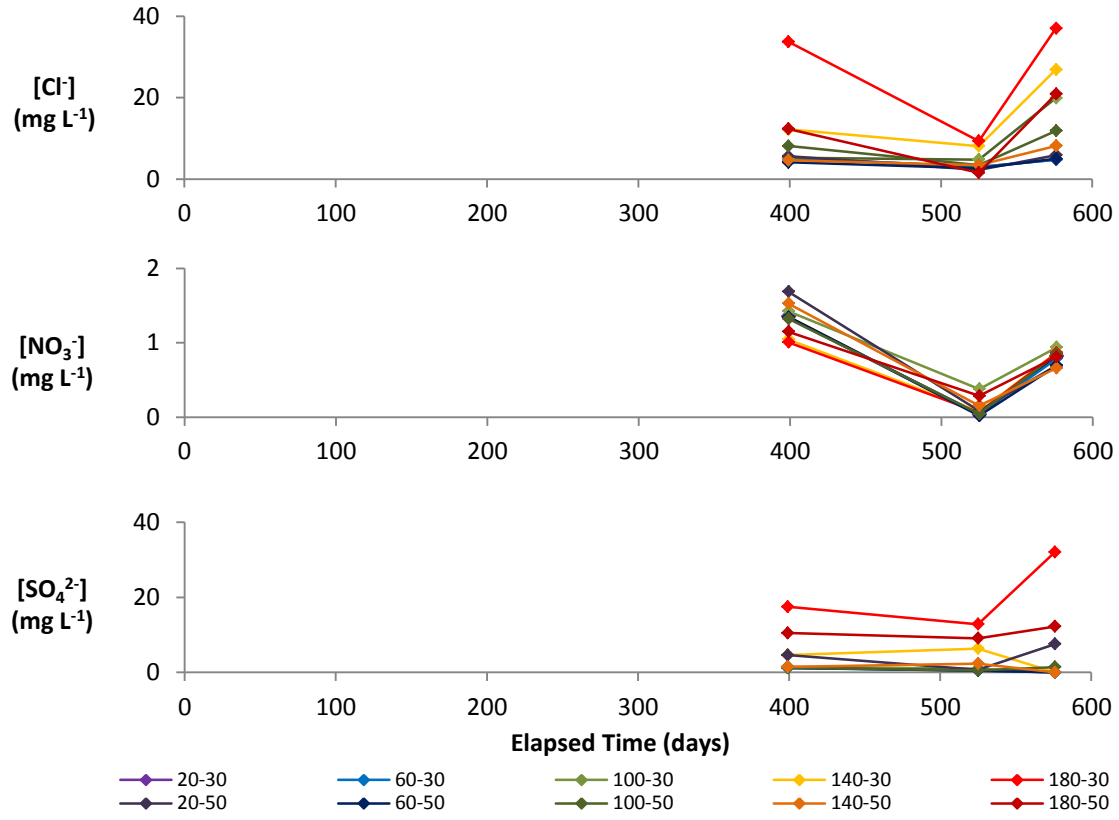

Figure 3-15: Elemental concentrations of anions: Cl, NO_3 and SO_4

Concentrations of Br^-, NO_2^-, PO_4^{3-} and F^- were below the detection limits of the instrument; this was <1 mg L^{-1} for F^- and <0.10 mg L^{-1} for Br^-, NO_2^-, and PO_4^{3-}. Sampling for anion analysis was not initiated until quite late in the experiment and temporal trends are somewhat difficult to establish from the data. In general, concentrations of Cl^-, $NO_3^-$and SO_4^{2-} tended to increase near the center of the tank and decrease toward the edges, which is a similar trend to the cation data. Notably, the concentrations in the deeper port (at 30 cm) were slightly higher than in the higher port (50 cm) which is the opposite trend as the cation data. The concentrations from the samples collected at 525 days do not seem to align with the concentrations from the samples taken at 399 and 576 days. This may be a dilution issue or an artefact caused by the increased error due to VFA interference. Overall, anion concentrations did not vary significantly across the different ports in the tank; maximum observed concentrations were 37 ppm, 1.7 ppm and 32 ppm for Cl^-, NO_3^- and SO_4^{2-} respectively.

NO_3^- may originate from the biodiesel itself, since there are no particular standards for nitrogen content in biodiesel. Lisiecki et al. (2013) estimated that biodiesel contained approximately 0.31% nitrogen. All anion scans were completed after the nutrient addition event; therefore NO_3^- may be from the nutrient application itself, which contained NH_4Cl at 7.5 mg L^{-1}. Unfortunately, there are no NO_3^- concentrations before the nutrient application which could be used to confirm this hypothesis.

SO_4^{2-} may have come from the sediments, although sulfide oxidation seems unlikely since according to the whole rock analysis, there is almost no sulfur present in the sediments (concentrations were below detection limit). The sulfate may also have originated from the sulfur in the biodiesel itself; according to ASTM D6751 the maximum sulfur concentration permitted in biodiesel is 15 ppm.

The source of Cl^- is probably also from the nutrient addition event, which involved the application of NH_4Cl as mentioned. It may also result from the Vancouver tap water. The Nutrafin™ converts Cl_2 or other chlorine based oxidants to Cl^-, which could then be picked up by the anion scan. The Cl^- may come from silicate dissolution; however, none of the mineral phases identified during the XRD analysis or the Rietveld refinements contain Cl.

3.4 Compound Specific Isotope Analysis (CSIA)

Compound specific isotope analysis (CSIA) provides a tool to assess microbial degradation reactions and pathways in contaminated environments (Elsner et al., 2005). This analysis assumes that molecules with heavier isotopes in their reactive positions (eg. ^{13}C and ^{2}H) are generally more slowly degraded than those with lighter isotope in their reactive positions (eg. ^{12}C and ^{1}H). This is due to the slight increase in the strengths of the bonds with the larger, slightly higher massed elements. Since the lighter isotopes are likely to react more quickly, a shift in isotopic composition of the remaining contaminant fractions toward enrichment in heavier isotopes is expected in the course of biodegradation. Isotopic enrichment

results almost entirely from biodegradation processes and its effect on abiotic physical processes such as sorption is considered negligible in comparison (Dempster et al., 1997, Harrington et al., 1999).

Biodegradation and biotransformation both include cycling of carbon; carbon is an essential molecular building block and a component of organic contaminants. Stable isotope data are reported as isotope ratios i.e. ratios of two compounds, one of which carries a rare stable isotope. Isotope ratios in gaseous and aqueous samples are not affected by most physical processes, including dilution, volatilization, and sorption, because these processes affect both compounds equally (Aelion et al., 2009).

Stable isotopes are often used to identify substrate in methanogenesis because the two major substrates, acetate and CO_2, react with H_2(g) and are easily distinguished based on stable carbon and hydrogen analysis of methane (Aelion et al., 2009).

Isotopes of elements such as carbon and hydrogen react at slightly dissimilar rates during mass differentiating reactions such as biodegradation. During biodegradation processes, isotopic fractionation of organic contaminants occurs because it is easier for microorganisms metabolizing these compounds to break bonds containing the light isotope. Therefore, while the gaseous compounds become enriched in the lighter isotopes it would be expected that the remaining biodiesel would become enriched in the heavier carbon isotopes compared to the original isotopic value of the parent compound. The initial $\delta^{13}C$ signature of the biodiesel is -29.9‰.

The CSIA data presented in the following figures was obtained from the vadose zone in ports above the capillary fringe. However, oxygen concentrations remained close to atmospheric for the duration of the experiment, making CH_4 generation unlikely. The CH_4 is believed to have been mostly generated in the saturated zone where anaerobic conditions were more likely to develop and methanogenesis was made possible. Since it was not part of the experimental program to sample CH_4 in the saturated zone, the CSIA was performed on the CH_4 that migrated through the unsaturated zone.

3.4.1 CO_2 Results ($\delta^{13}C$)

Figure 3-16 shows the $\delta^{13}C$ results for the CO_2 obtained from a vertical transect in the sandtank. The isotope signature from three ports near the center of the sandtank at depths of 70 cm, 90 cm and 110 cm are represented by the triangular blue, red and green markers, respectively). The CO_2 concentrations from the same ports are represented by the diamond markers.

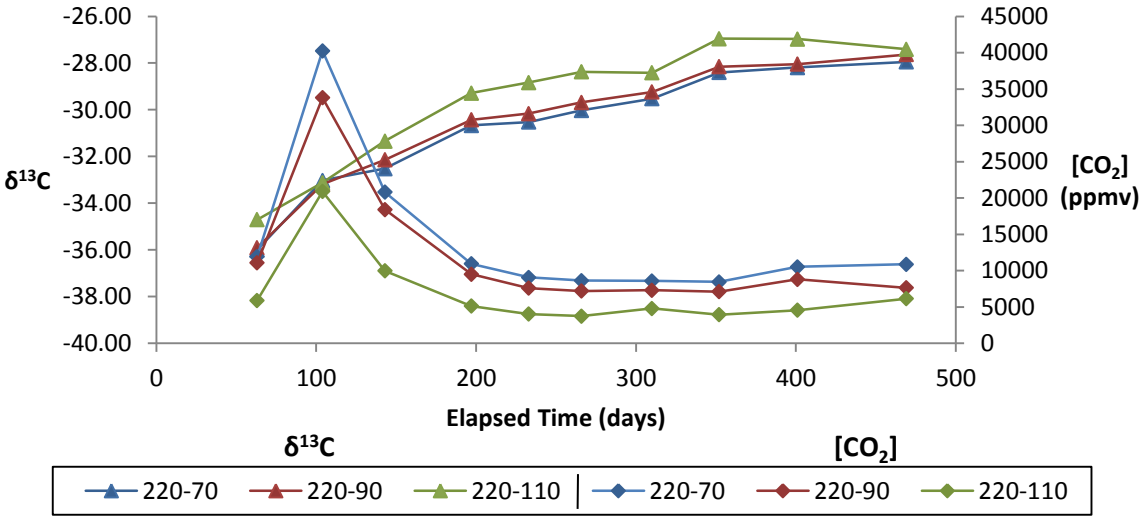

Figure 3-16: $\delta^{13}C$ results for the CO_2 obtained from a vertical transect of three ports near the center of the sandtank

Initially, the $\delta^{13}C$ value is very negative relative to the isotopic signature of the biodiesel free product, which is -29.9‰. This is because the gaseous CO_2 is enriched in the lighter carbon isotopes present in the biodiesel. The $\delta^{13}C$ value for CO_2 in air is approximately -26‰ (Aelion, 2009). The light isotopic signature of the CO_2 at the start of the experiment may help explain the high CO_2 concentrations observed at early time. Initially, high CO_2 production is likely a result of degradation of more labile compounds in the biodiesel; however, the isotopic effect is possibly also a small contributor to the faster aerobic degradation at early time. Since the isotopically lighter biodiesel molecules are expected to react more quickly, this easily degradable fraction is metabolized by the microbes more quickly at early time. Eventually, the ^{12}C concentrations begin to decrease.

At later time, the rate of CO_2 production stabilizes at a lower level and the isotopic signature of the CO_2 becomes more similar to the source signature (-29.9‰). Eventually, the source signature is expected to become heavier; however the $\delta^{13}C$ value for the biodiesel was measured three times at 0 days (-29.9‰), at 65 days (-29.9‰) and at 399 days (-29.7‰). The signature remained fairly constant over the time scale of this experiment at the measurement location, although it was slightly heavier at 399 days. Note biodiesel could only be effectively extracted from one port in the saturated zone where degradation is much slower, therefore this result is not surprising.

Over time, the $\delta^{13}C$ value for CO_2 becomes heavier than the original source, and approaches -28‰. Therefore, at later time the CO_2 in the sandtank may be mixing with the CO_2 in the ambient air. This is unlikely to provide a complete explanation, since there is only 400 ppm in ambient air ($\delta^{13}C$ = -26‰), while CO_2 concentrations between 5000-10000 ppm were measured in the sandtank. CO_2 from air would have to make up approximately half of the CO_2 in order to bring the biodiesel signature of -29.9‰ down to -28‰.

There is a discernible change in isotopic signature with depth and the $\delta^{13}C$ value at the lower ports is slightly lighter than at the higher ports. Since lighter CO_2 was observed closer to the water table, it is possible that biodiesel is heavier in the vadose zone (< -28‰), where it has been more quickly degraded. The CO_2 from the heavier vadose zone biodiesel may combine with the CO_2 diffusing up from the saturated zone causing the isotopic signature to become heavier. Although this conceptual model would explain the $\delta^{13}C$ profile for CO_2, a sample of biodiesel could not be obtained from the vadose zone. Thus, it is difficult to confirm this hypothesis for certain.

The results shown in Figure 3-17 and Figure 3-18 show a similar, more muted pattern to the results in Figure 3-16. Again, molecules with lighter isotopes seem to be degraded preferentially at early time and the isotopic signature of the CO_2 gas becomes heavier over time, approaching the isotopic signature of

the biodiesel. The data are from vertical transects at 60 cm and 100 cm from the center of the sandtank, respectively. The change in isotopic signature with depth is less clear on these plots than in Figure 3-16.

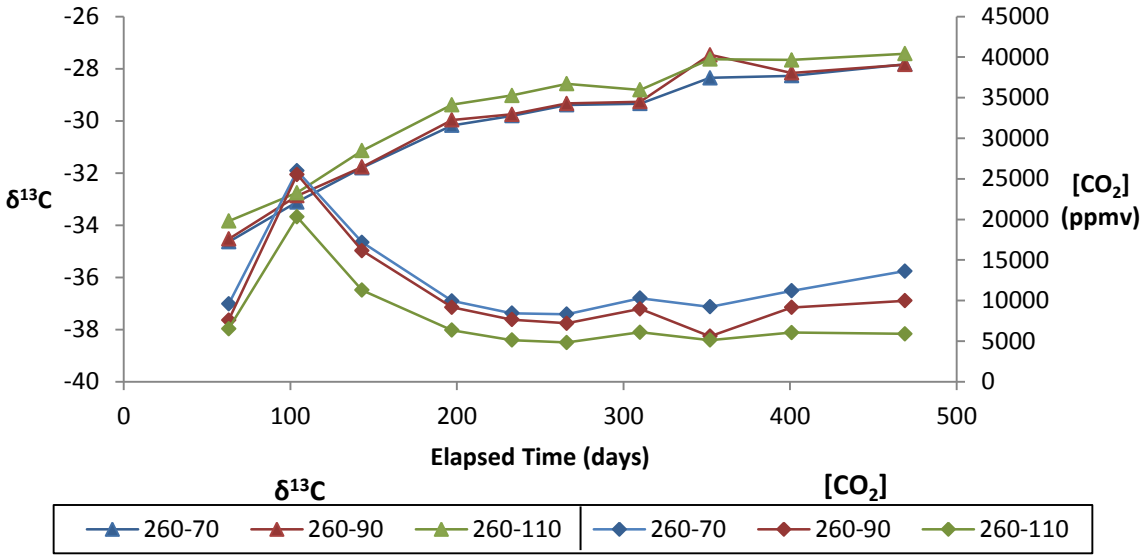

Figure 3-17: $\delta^{13}C$ results for the CO_2 obtained from a vertical transect of three ports 60 cm from the center of the sandtank

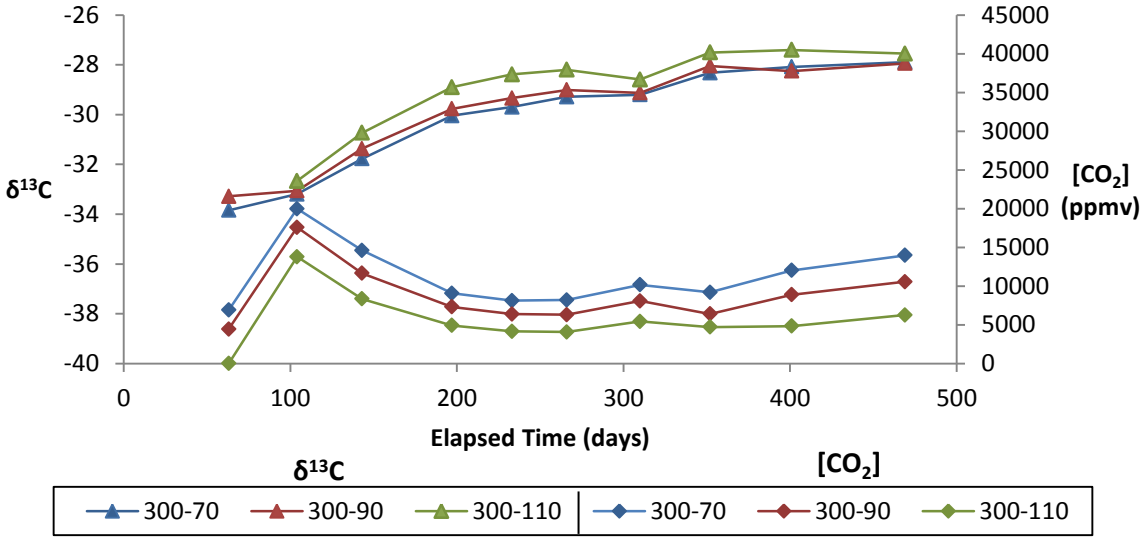

Figure 3-18: $\delta^{13}C$ results for the CO_2 obtained from a vertical transect of three ports 100 cm from the center of the sandtank

According to Meckenstock et al. (2004), the quantification of aerobic degradation based on stable isotope analysis is not possible because there are many enzyme systems which can produce large

differences in fractionation values. Nevertheless, the observation of isotope fractionation can be taken as a qualitative indicator that biodegradation is occurring.

3.4.2 CH_4 Results ($\delta^{13}C$ and $\delta^{2}H$)

The application of isotopes can be used to evaluate the origin and fate of CH_4 in the vadose zone. The isotopic composition is an indication of the isotopic composition of the carbon source, the carbon pathway for CH_4 production, and the effect of oxidation (Whiticar, 1999). There may be some organic carbon in the soil, but it is likely negligible and it was not observed in the sediment analysis. Since there are no other significant potential carbon sources for CH_4 in the sandtank system, this analysis will focus on the carbon pathway and the effect of oxidation.

Microbial CH_4 production typically occurs in organic-rich, anoxic, freshwater environments. In the sandtank, anoxic conditions developed in the saturated zone, and CH_4 production predominantly occurred at or below the water table. The CH_4 concentration and isotope data were obtained above the water table, from the vadose zone, and may be representative of gases which have migrated up from the lower section of the sandtank. Conversely, anaerobic micro-niches may develop in the vadose zone allowing CH_4 production to occur locally, even within a mostly oxic regime.

CH_4 production requires microbial consortia composed of at least three interacting groups.

1. Fermentative bacteria hydrolyze large organic polymers to long chain volatile fatty acids, alcohols, H_2, CO_2, formate and acetate.
2. Acetogenic bacteria oxidize the higher VFAs and alcohols to acetate and H_2 or formate
3. Methanogens represent the terminal step in the anaerobic chain of decay. CH_4 may be generated from acetate or from a CO_2 reduction pathway where H_2 or formate is oxidized to generate electrons.

According to Wolfemate et al. (1984), acetate fermentation typically dominates in freshwater environments; however, CO_2 reduction can become important if organic matter is recalcitrant and pH is low. CH_4 from anaerobic environments is typically depleted in ^{13}C and ^{2}H. In the sandtank, pH conditions were relatively acidic (ranging between 4.5 and 6 at later time), so CO_2 reduction is a likely possibility.

CSIA data can provide information about the processes affecting CH_4 in the vadose zone and may help determine the occurrence of CH_4 oxidation. It is essential to evaluate the CH_4 isotopic signature in the vadose zone in order to quantify whether CH_4 oxidation is occurring. It is well documented that during oxidation of CH_4, residual CH_4 becomes enriched in the heavy isotopes ^{13}C and ^{2}H since the oxidation reaction rate is faster for the CH_4 molecules with the light isotopes ^{12}C and ^{1}H compared with the CH_4 composed of heavy isotopes (Whiticar, 1999). The isotope pattern observed during the aerobic oxidation of CH_4 is larger for C than for H (Hunkeler et al., 2001), and is very different than the isotope pattern obtained during anaerobic degradation, which is larger for H than for C (Mancini et al., 2003).

Figure 3-19 shows the $\delta^{13}C$ results for CH_4 from the vertical transect near the center of the sandtank. Since these measurements were made in the vadose zone, where conditions are aerobic for the duration of the experiment, it is expected that the CH_4 is generated in the saturated zone and released from the capillary fringe region. The CH_4 then migrates up towards the surface, passing the monitoring ports. Along this path, it may be affected by isotopic fractionation due to oxidation as CH_4 moves through the vadose zone and encounters O_2.

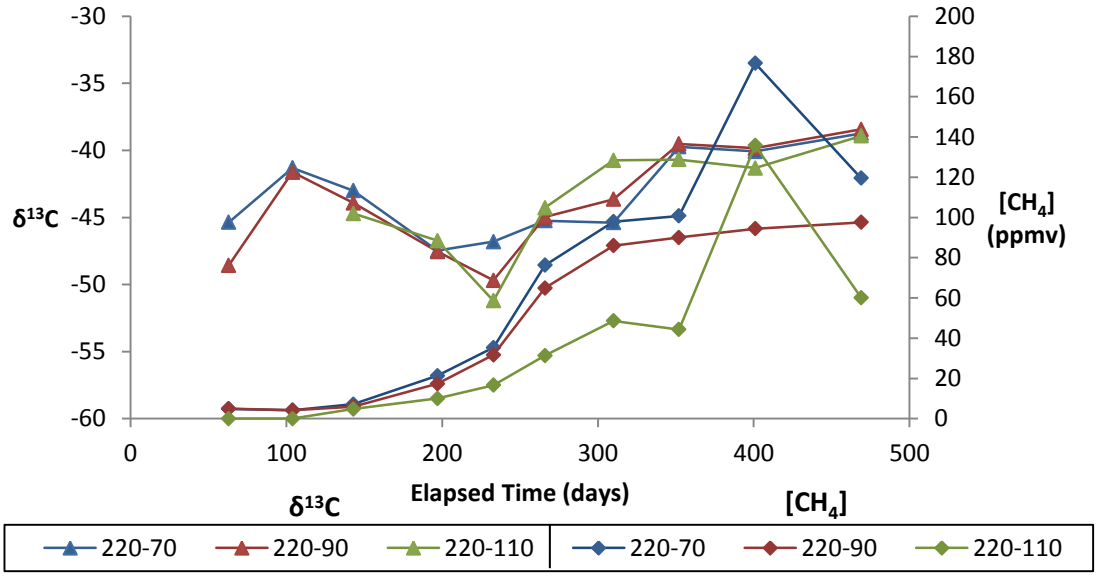

Figure 3-19: $\delta^{13}C$ results for the CH_4 obtained from a vertical transect of three ports 20 cm from the center of the sandtank

There is approximately 2 ppm of CH_4 in air, and the $\delta^{13}C$ value is approximately -48.5‰ (Yu et al., 2015). The $\delta^{13}C$ results for CH_4 in the sandtank start at around this value, which makes sense since concentrations in these ports are only around 4-5 ppm and therefore likely dominated by the signal from ambient air. The $\delta^{13}C$ become slightly lighter as CH_4 concentrations begin to increase, presumably for the same reasons as explained for CO_2, where the light biodiesel compounds are preferentially degraded. The signature becomes slightly heavier, approximately -40‰ near the end. This may be because the ^{12}C compounds become scarcer in the biodiesel.

The $\delta^{13}C$ value for CH_4 is consistently much lighter than the source isotope concentration ($\delta^{13}C$ = -29.9‰). The oxidation process would lead to enrichment of ^{13}C in CH_4. However, there is no visible trend in the $\delta^{13}C$ signature versus depth, which provides evidence that oxidation of CH_4 in the vadose zone is not a significant process (R. Aravena, personal communication, Nov. 28, 2016).

In general, obtaining a clear trend in $\delta^{13}C$ values for CH_4 at low concentrations is difficult because the mass difference between the ^{13}C and the ^{12}C is not as pronounced as the mass difference between ^{2}H

and ^{1}H. The relative mass difference is 1.08 for $^{13}C/^{12}C$ and 2.00 for $^{2}H/^{1}H$ (Hoefs, 1997). Still, it is important to collect $\delta^{13}C$ results despite possible noise in the data for comparison with the $\delta^{2}H$ results.

Figure 3-20 shows the $\delta^{13}C$ results for CH_4 from the vertical transect 60 cm from the center of the sandtank plotted versus time. These results are similar to those in Figure 3-19; the $\delta^{13}C$ values are consistently lighter than the source biodiesel signature, and the values become slightly heavier over the experimental period, which is consistent with earlier findings. There is no strong discernible trend with depth in the sandtank.

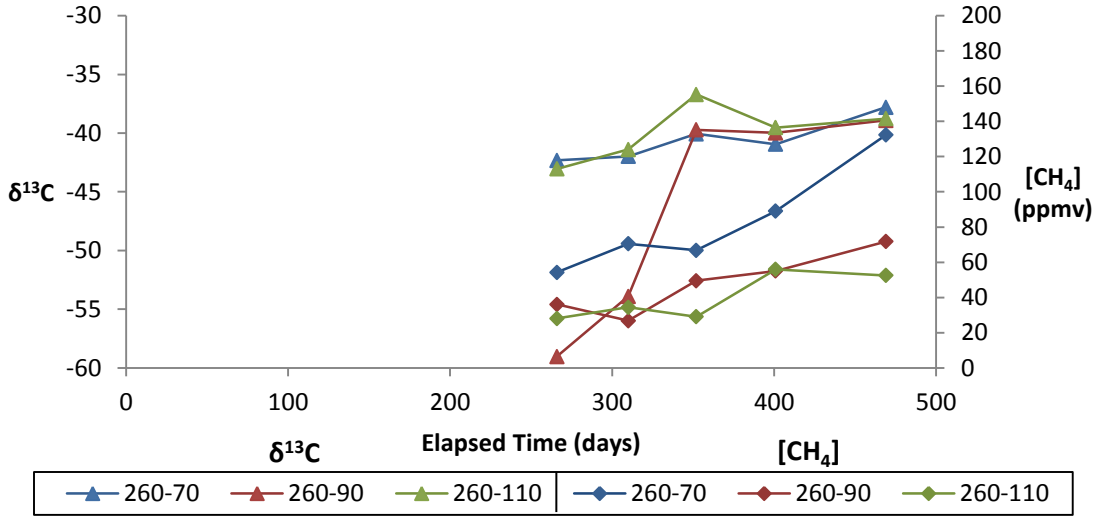

Figure 3-20: $\delta^{2}H$ results for the CH_4 obtained from a vertical transect of three ports 60 cm from the center of the sandtank

Figure 3-21 and Figure 3-22 show the $\delta^{2}H$ results for CH_4 plotted versus time over vertical transects 20 cm and 60 cm from the center of the sandtank, respectively. The $\delta^{2}H$ values become progressively lighter as CH_4 production increases and stabilize at between -267‰ and -315‰.

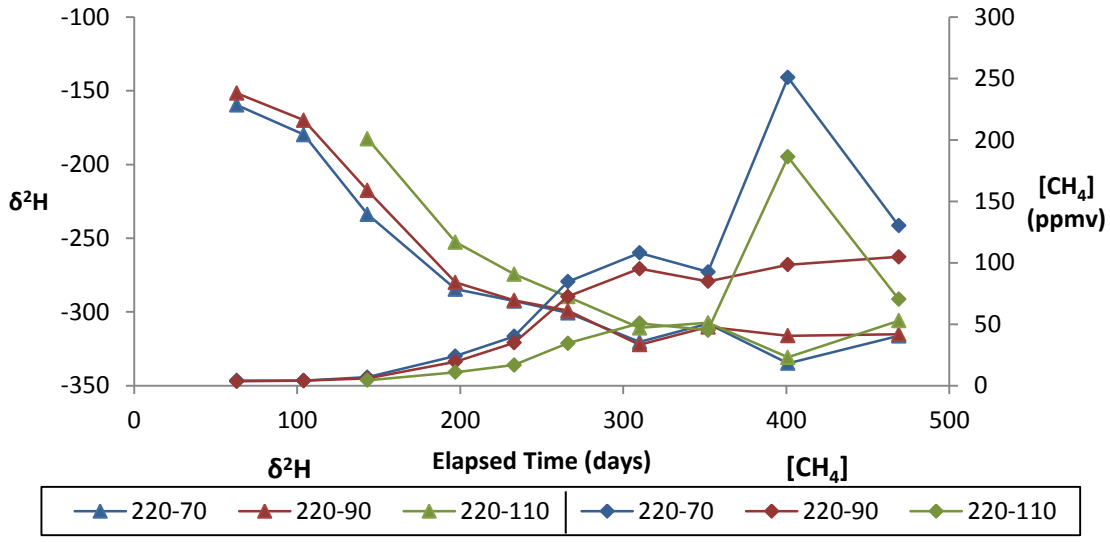

Figure 3-21: δ^2H results for the CH_4 obtained from a vertical transect of three ports 20 cm from the center of the sandtank

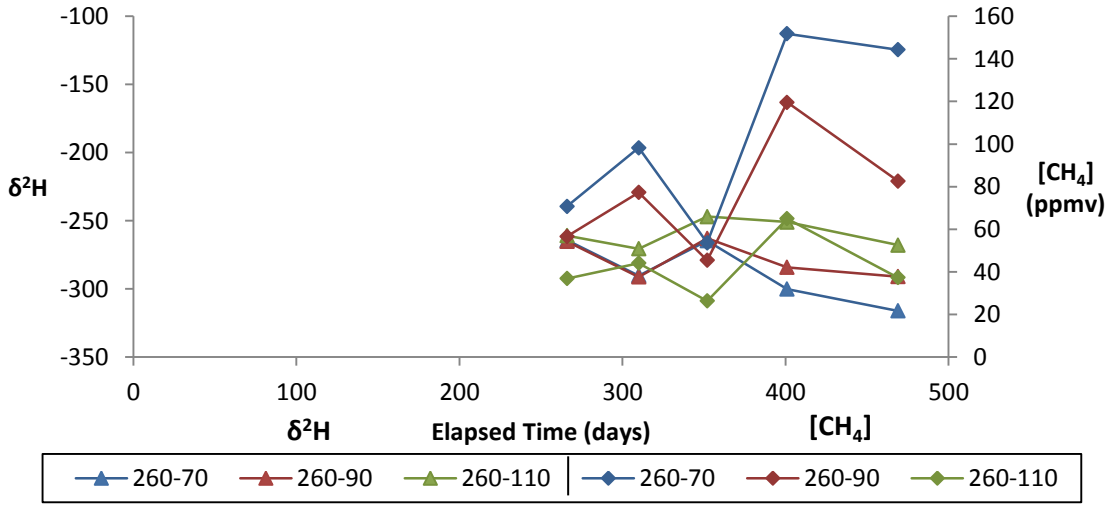

Figure 3-22: δ^2H results for the CH_4 obtained from a vertical transect of three ports 60 cm from the center of the sandtank

All plotted values are very light, considering the isotopic signature of Vancouver tap water is -84‰. The origin of the H molecules in the CH_4 may be from the biodiesel itself, in which the δ^2H value is unknown. Near the beginning of the experiment, the δ^2H isotopic signature is slightly heavier at the deeper ports and lighter at the shallower ports. This vertical trend may point toward small amounts of CH_4 oxidation occurring as the CH_4 migrates upward through the aerobic vadose zone. After 233 days, the trend is less

visible and the δ^2H value is similar at all depths, which may indicate that CH_4 oxidation weakens or is no longer occurring at later time.

According to Aelion et al. (2009), methane oxidation in an aerobic environment (i.e. methanotrophic conditions) will lead to enrichment in ^{13}C for CH_4. This will cause $\delta^{13}C$ values to become less negative. O_2 levels have remained relatively high in the sandtank over the course of the experiment, so we expect the results to indicate aerobic methane oxidation. Near the beginning of the experiment, this is confirmed by the CH_4 $\delta^{13}C$ isotope data becoming slightly lighter at shallower depths. Over time, however, the $\delta^{13}C$ values stop changing and eventually become heavier. This may be due to the generation of acidity in the unsaturated zone porewater, which prevents methanotrophic bacteria from establishing themselves effectively.

Figure 3-23 shows the $\delta^{13}C$ values in CO_2 vs $\delta^{13}C$ values in CH_4 for all ports. All points fall in zone of methane oxidation according to Whiticar (1999). However, the source C in biodiesel is heavier than the C in CH_4, which further implies that CH_4 oxidation is weak. This may be due to unfavorable, low pH conditions for the methanotrophic microbes. In the vadose zone, there is water and O_2 concentrations are high, therefore a CH_4 efflux, even a small one, is a surprising result. According to Sihota et al. (2013), a vadose zone of 1 m or more will lead to very limited CH_4 effluxes unless CH_4 production is high. Sihota et al. (2013) showed that the development of large CH_4 effluxes requires high soil moisture, poorly aerated conditions, and close proximity to the source zone.

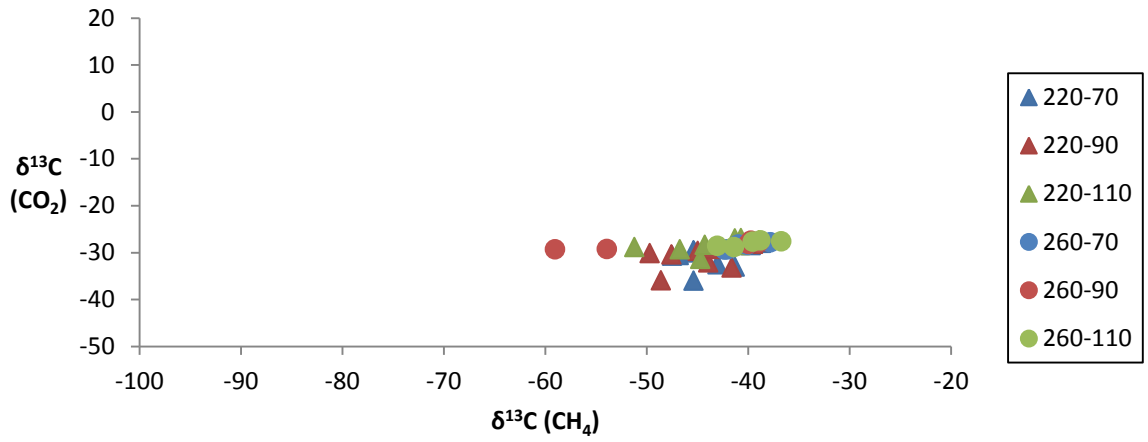

Figure 3-23: $\delta^{13}C$ values in CO_2 vs $\delta^{13}C$ values in CH_4 for all ports

Overall, the isotope data indicates that methane oxidation in the vadose zone is weak in general, but is occurring to some degree, particularly at early time. This makes sense, since the pH is relatively neutral across all ports at early time. The $\delta^{13}C$ and $\delta^{2}H$ data from CH_4 and the dual isotope plot indicates that weak oxidation is occurring; however, the data become less clear at later time.

In summary, Figure 3-24, Figure 3-25 and Figure 3-26 show the vertical profiles for the stable isotope values over time. The $\delta^{13}C$ value in CO_2 becomes heavier over the course of the experiment, the $\delta^{13}C$ value in CH_4 shows an initial phase where the values become lighter (likely deviating from an air dominated signal) but then becomes heavier as time progresses and CH_4 concentrations increase. The $\delta^{2}H$ value in CH_4 becomes lighter over the course of the experiment. This would point to a depletion of lighter isotopes in the source (biodiesel) over time, particularly the easily degradable compounds, both in the aerobic and anaerobic environment. This was not seen in the source isotopic signature which remained at approximately -29.9‰ although samples were only collected at one port in the saturated zone. This also may be because so little of the biodiesel is degraded relative to the 80 L present in the tank, in particular at the location where the biodiesel isotope samples were collected from.

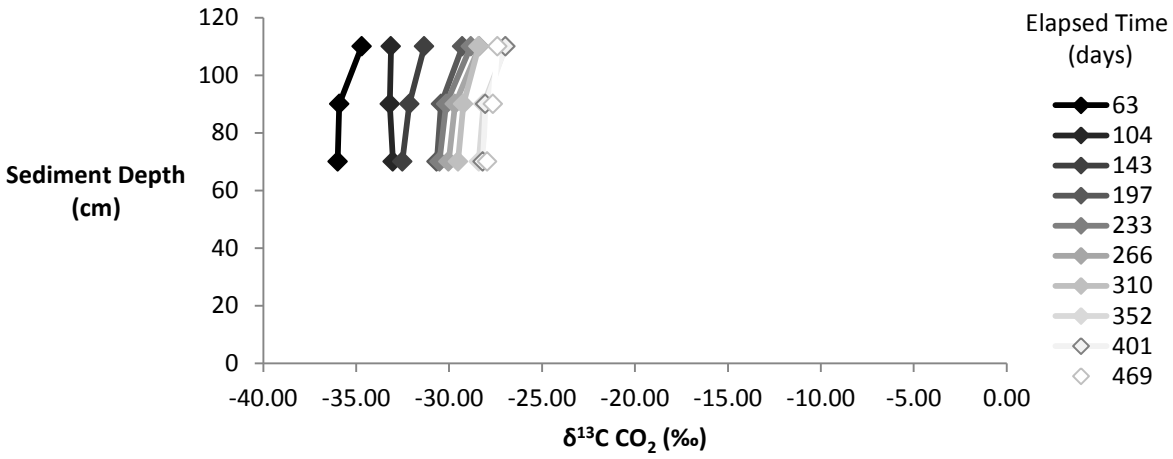

Figure 3-24: Vertical profiles of $\delta^{13}C$ in CO_2 values over time

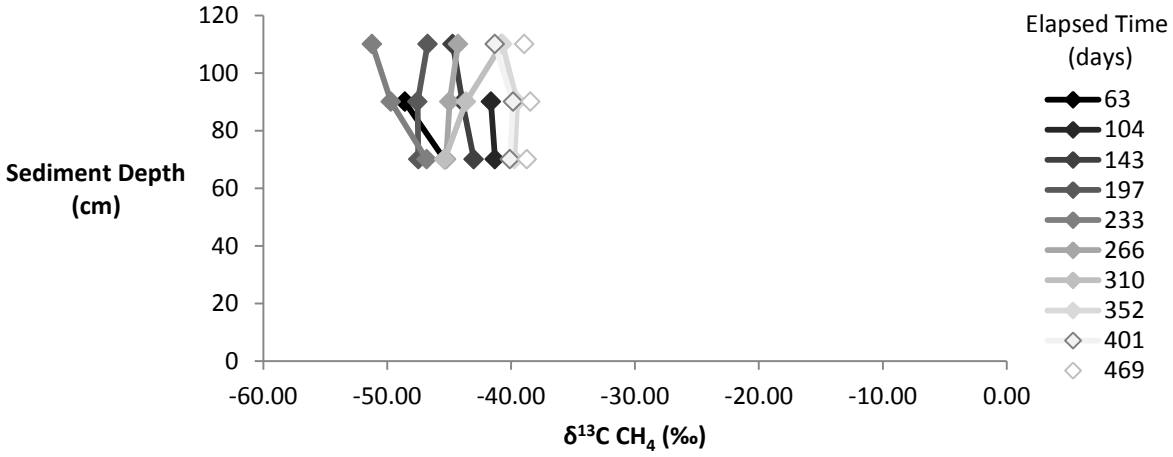

Figure 3-25: Vertical profiles of $\delta^{13}C$ in CH_4 values over time

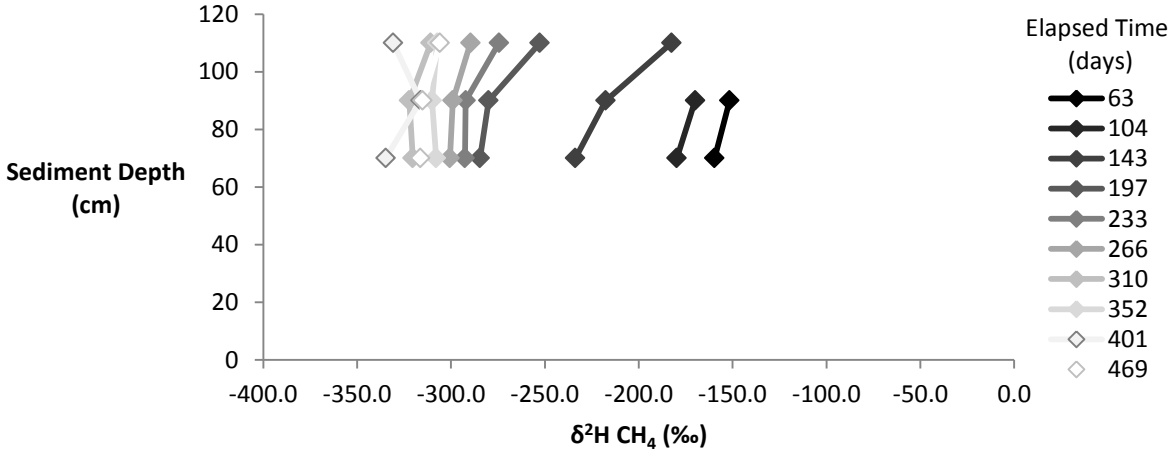

Figure 3-26: Vertical profiles of $\delta^{2}H$ in CH_4 values over time

3.5 Synthesis

3.5.1 Biodiesel Persistence and Rate of Degradation

(ii) Which processes affect/control biodiesel degradation under the given experimental conditions, and how do these processes evolve? What are the dominant terminal electron accepting processes (TEAPs)?

When the biodiesel was settled, distinguishable redox zones began to develop in the tank, which are described in the following sections. The rate and magnitude of degradation is mediated by the redox buffering capacity of the sediments. In theory, following the consumption of an oxidized element within a volume of sediments, the reaction with the next highest energy yield becomes predominant. These reactions occur sequentially according to the redox ladder and may involve gases, aqueous compounds as well as solids and associated ion exchange components (Christensen et al., 2000). Based on the sediment characterization results, it was anticipated that iron reduction and methanogenesis may become the dominant redox processes occurring in the sediments once anaerobic conditions are established (Klassen, 2015).

This experiment focused on the vadose zone, therefore the water content was unevenly distributed in the tank resulting in variable reaction rates and characteristics. The dominant TEAPs for the sandtank will be examined for two general zones: the aerobic unsaturated zone and the anaerobic saturated zone.

3.5.1.1 Unsaturated Zone

The most important TEAP in the unsaturated zone is aerobic respiration. Gas concentrations from samples obtained at all locations in the unsaturated zone revealed high O_2 concentrations for the duration of the experiment. Since aerobic degradation is an acid-generating reaction, pH levels in the pore water likely began to decline. Aerobic degradation rates increased initially then decreased following the precipitation event, as evidenced by a reduced CO_2 efflux. Some of the biodiesel

(particularly in the pool) was likely covered by water which limited O_2 access for aerobic degradation of the biodiesel. Since biodiesel is a fairly complex molecule, the aerobic degradation of biodiesel may have occurred in two stages: first, the biodiesel is broken down into simpler organic monomers, and second, the simple sugars are degraded to CO_2. Examples of these two reactions are:

$$3C_{16}H_{32}O_2 + 21O_2 \rightarrow 8C_6H_{12}O_6$$

$$C_6H_{12}O_6 + 6O_2 \rightarrow 6CO_2 + 6H_2O$$

These are examples of general reactions since biodiesel consists of many complex molecules, which may have different carbon chain lengths. Although aerobic degradation appears to be proceeding for the duration of the experiment, rates did fluctuate. It is hypothesized that these fluctuations were caused by a combination of pH changes, soil moisture content changes and the depletion of the most highly degradable substrate material as time progressed.

Although multiple attempts were made (using soil water solution samplers, core collection and centrifuging), the vadose zone pore water could not be sampled for measurement of cation or VFA content. It is unlikely that VFA production was significant in the vadose zone, since it remained aerobic for the duration of the experiment. However, it is possible that small amounts of VFA generation occurred in local anaerobic micro-niches of the unsaturated zone.

Fe and Mn reduction were also unlikely to be occurring in the unsaturated zone due to the high O_2 content. However, dolomite dissolution as a result of the high acid generation from aerobic degradation may have mobilized higher concentrations of Ca^{2+}, Mg^{2+}, Mn^{2+} and Fe^{2+}.

Small CH_4 concentrations were measured in the unsaturated zone. Methanogenesis may have occurred in small anaerobic micro-niches of the vadose zone. However, it is more likely that CH_4 was generated in the anaerobic saturated zone and diffused up through the unsaturated zone. It is possible that the

methane is being produced below the "perched" water table, located on the biodiesel pool, and diffusing up through the vadose zone. Overall, the results support aerobic degradation dominates in the vadose zone, possibly self-limited by the generation of acidity, which also inhibits the degradation of CH_4 entering the vadose zone from the underlying capillary fringe and pool region.

3.5.1.2 Saturated Zone

In the saturated zone, the water and biodiesel filled the pore spaces, therefore O_2 ingress was inhibited. It should be noted that O_2 concentrations were not measured in the sandtank water. Therefore, the aqueous chemistry results were central in determining the dominant redox processes occurring in the saturated zone of the sandtank. The implication of water with a low initial conductivity is that the initial composition does not matter very much – the final water composition results were a direct consequence of the interaction between the water, the sediments and the biodiesel.

After the initial O_2 was consumed in the saturated zone of the sandtank, Fe and Mn reduction was the likely dominant redox process as evidenced by the high concentrations of Fe^{2+} and Mn^{2+} in the water. Fe and, in particular, Mn concentrations were noticeably higher after 206 days. The presence of ankerite from the sediment characterization results lead to some uncertainty regarding the origin of the aqueous Fe and Mn. VFA concentrations also increased steadily once anaerobic conditions were established, beginning at around 167 days.

Finally, after approximately 250 days low concentrations of CH_4 were detected in the unsaturated zone sampling ports. Therefore, a small contribution to the biodiesel degradation seems to be occurring due to methanogenesis at and below the water table.

In anaerobic systems, there are several stages of microbial digestion of complex organic material such as biodiesel (Ostrem, 2004). These stages can be applied to the conceptual model of the saturated zone of the sandtank.

In the first stage, hydrolysis, the biodiesel is broken down into smaller, more easily degradable organic carbon molecules. Fermentative bacteria are responsible for the creation of monomers, which are then available to the next group of bacteria. The occurrence of this step was not measured, and it would have been difficult to quantify the rate of biodiesel hydrolysis. Nevertheless, this step can be inferred based on the continued progress of the following steps (i.e. VFA production).

In general, hydrolysis is catalyzed by enzymes excreted from the bacteria. If the feedstock is complex, the hydrolytic phase is relatively slow (Ostrem, 2004). The following equation shows an example formula for the hydrolysis of biodiesel (although it should be noted that biodiesel contains more than one type of molecule).

$$3C_{16}H_{32}O_2 + 42H_2O \rightarrow 8C_6H_{12}O_6 + 42H_2$$

The next stage is acidogenesis. Acidogenic bacteria turn the products of hydrolysis into simple organic compounds, mostly short chain volatile fatty acids (eg. propionic, butyric, formic, lactic or succinic acid), ketones and alcohols. The products of acidogenesis as well as their concentrations vary with culture conditions, such as pH and temperature (United Tech 2003). VFA data was collected in the saturated zone (both in the capillary fringe and at the water table) and high concentrations of acetic, propionic and butyric acids were reported. The following equations show example reactions where glucose is degraded to propionate and butyrate, respectively.

$$C_6H_{12}O_6 + 2H_2 \rightarrow 2CH_3CH_2COOH + 2H_2O$$

$$2C_6H_{12}O_6 + 6H_2 \rightarrow 3CH_3CH_2CH_2COOH + 6H_2O$$

The next stage is acetogenesis which is often considered with acidogenesis to be part of a single acid forming stage. The biological oxygen demand (BOD) and chemical oxygen demand (COD) of a system are

reduced through these pathways (Ostrem, 2004). Acetogenesis is a process of carbohydrate fermentation, and the main product is acetate along with CO_2 and H_2.

Hydrogen is an important intermediary in the anaerobic zone. Long chain fatty acids, formed from the hydrolysis of lipids, are oxidized to acetate or propionate and hydrogen gas is formed. Under standard conditions, the presence of hydrogen in the solution inhibits the oxidation. Thus, the reaction only proceeds if the hydrogen partial pressure is low enough to make the reaction thermodynamically feasible. The presence of hydrogen scavenging bacteria that consume hydrogen is necessary to reduce the partial pressure of hydrogen and ensure the conversion of all acids (Mata-Alvarez, 2003).

The equation below shows the reaction that converts propionate to acetate. The free energy value of this reaction is +76.1 kJ, making the transformation thermodynamically unfavorable. However, as long as the acetate and hydrogen are consumed by bacteria, the reaction will proceed (Ostrem, 2004). Since propionate concentrations peaked and eventually decreased, it is very likely this reaction was occurring in the sandtank.

$$CH_3CH_2COO^- + 3H_2O \rightarrow CH_3COO^- + H^+ + HCO_3{}^- + 3H_2$$

However, acetate concentrations were an order of magnitude higher than propionate concentrations throughout the experiment. Acetate can also be formed directly from glucose, as seen in the equation (Ostrem, 2004):

$$C_6H_{12}O_6 + 2H_2O \rightarrow 2CH_3COOH + 2CO_2 + 4H_2$$

These acid forming stages cause the pH of the system to drop. This is beneficial for the acidogenic and acetogenic bacteria that prefer a slightly acidic environment, with a pH of 4.5 to 5.5, and are less sensitive to changes in the environment, but it is problematic for the bacteria involved in the next stage:

methanogenesis (Verma, 2002). This may explain the relatively low methane formation rates observed in the experiment (section 3.2.1).

CH_4 is the product of the last stage of fermentation, methanogenesis, which causes the transformation of soluble organic matter to methane. According to Ostrem, 2004, about two thirds of the methane is expected to be derived from acetate conversion, and one third is the result of carbon dioxide reduction by hydrogen. The following equations show the balanced chemical reactions involved in methanogenesis in the saturated zone of the sandtank, based on the species present in the tank. The first equation shows methanogenesis via acetate fermentation, and the second reaction shows methanogenesis via CO_2 reduction.

$$CH_3COOH \leftrightarrow CH_4 + CO_2$$

$$CO_2 + 4H_2 \leftrightarrow CH_4 + 2H_2O$$

Changes to their environment can have a large impact on methanogens; they tend to thrive in a neutral to slightly alkaline environment (Van Ginkel et al., 2001). In the presence of O_2, methanogenesis does not proceed. Clearly, some methane was being produced in the sandtank in areas where biodiesel was present as free product; this may have occurred in the saturated zone (both in the capillary fringe and below the water table) and possibly as well in locally anoxic vadose zone micro-niches. Although methanogenesis did proceed in the anoxic areas of the sandtank, CH_4 production may still have become severely inhibited if the pH fell below 6. Since methanogens typically have a much slower growth rate than acidogens (Davis and Cornwell, 1998), decreasing pH values are of concern and may cause the methanogenic microbes to die. Because of its slower rate, methanogenesis is the rate-controlling portion of the biodiesel degradation. CH_4 production appears to commence after the VFA concentrations have peaked, which is consistent with literature results (Verma, 2002).

Figure 3-27 shows a simplified summary of the processes occurring in the sandtank according to the conceptual model described above.

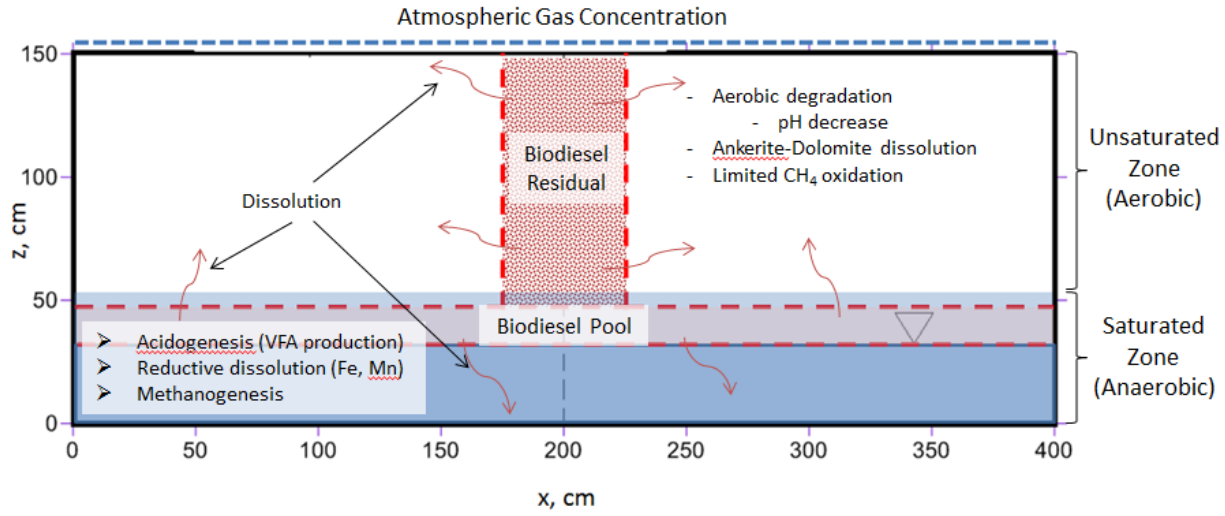

Figure 3-27: Simplified summary of conceptual model for sandtank processes

(iii) Does biodiesel degradation lead to significant generation of CO_2 and CH_4 in the subsurface?

In this experiment, biodiesel degradation did not lead to substantial CO_2 and CH_4 generation in the subsurface. Most of the CO_2 sensors seemed to stabilize between 0.5 and 2% near the end of the experiment at 590 days; maximum CO_2 concentrations observed in the tank near the beginning of the experiment were around 3%. The maximum CH_4 concentration obtained from ports within the tank was approximately 800 ppm, with most values ranging from 130 ppm to 300 ppm.

This is quite a bit lower than CO_2 and CH_4 concentrations which have previously been observed at field sites. At an ethanol-blended fuel site described by Ma et al. (2013), subsurface deep soil gas reached concentrations of 68% v/v CH_4. A crude oil spill site in Bemidji, MN, showed depletion of O_2 as well as elevated CO_2 and CH_4. Average subsurface O_2 concentrations were 7.1% and average CO_2 and CH_4 concentrations were 10.1% and 4.7% respectively (Sihota and Mayer, 2012). Obviously, this is not a perfect comparison; the study at Bemidji was a field-scale study and involved crude oil instead of

biodiesel. It also took approximately 20 years for CH_4 production to occur at the Bemidji site in significant concentrations, and the water table is much deeper (approximately 6 m below ground surface).

Unfortunately, studies focusing on gas generation from biodiesel degradation are scarce. Tyson (2001) stated that pure biodiesel degrades 85 to 88% in water within 28 days, but did not report methane generation results. Experimental conditions were idealized for degradation in this small-scale experiment. In another study, a B20 field release was conducted by Ramos et al. (2013) (in the sandtank experiment described in this thesis, B100 was used). Ramos et al. (2013) reported maximum methane concentrations of 10 mg L^{-1} in the saturated zone after 2.25 years. Methane concentrations reached 20 mg L^{-1} in the zone biostimulated with ammonium acetate after 1.75 years. These values are close to CH_4 solubility; however, it is difficult to compare with the results of the sandtank experiment since CH_4 (aqueous) data was not collected here. Although these studies provide some context for the results of this experiment, very few studies have been done which focus on vadose zone degradation of biodiesel , so comparable data is not available.

Although CO_2 and CH_4 generation in the vadose zone were relatively low in this experiment, it is challenging to extrapolate these results to field conditions with much larger releases, deeper water tables, different sediment characteristics, possibly with higher moisture retention capacity and higher carbonate mineral content. The results obtained here are valid only for the experimental conditions and should not be generalized.

3.5.2 Carbon Mass Balance and Risk of Soil Vapour Intrusion

The CO_2 and CH_4 effluxes can be used to quantify the relative amount of biodiesel which had been degraded and removed from the sandtank during the duration of the experiment. To this end, a rough

carbon mass balance calculation was completed to determine the mass of biodiesel transformed to gaseous end products. This rate can be used to help determine the risk of soil vapour intrusion.

3.5.1.3 Carbon Mass Balance

Each chamber was assigned a volume of the tank as seen in Figure 3-28, with the assumption that the chemistry and transport in the sandtank was taking place symmetrically from the center.

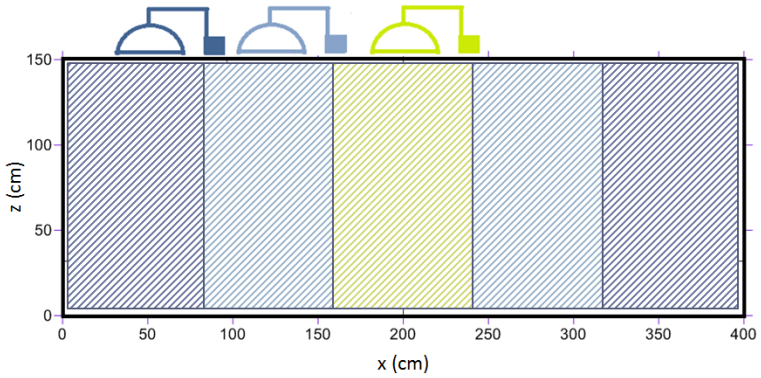

Figure 3-28: sandtank surface areas assigned to each LiCOR chamber for the purpose of the carbon mass balance calculations

As seen in section 3.2.1, the flux from each port is reported in µmol m^{-2} s^{-1}. To calculate the flux of carbon exiting the tank, the flux of CO_2 was multiplied by the time step (Δt) and the area assigned to the chamber (1.75 m^2, 1.5 m^2 and 0.75 m^2 for chamber 1, 2 and 3 respectively). These values were summed across all time steps to determine the cumulative carbon flux, and converted to kg of C using the molar ratio for carbon of 12 g mol^{-1}. This value can be reported as a % biodiesel degraded using several reasonable assumptions. First, an average biodiesel molecule was assumed to be represented by the chemical formula $C_{17}H_{34}O_2$ based on an average carbon chain length. By unit conversion, 80 L of biodiesel present in the sandtank can be converted to 51.98 kg of carbon. This value was used to normalize the carbon flux from the sandtank and represent it as “biodiesel degraded”. This value, through time, is plotted in Figure 3-29. The cumulative biodiesel degraded 590 days after initiation of the experiment is 3.7% of the 80 L initially present in the sandtank.

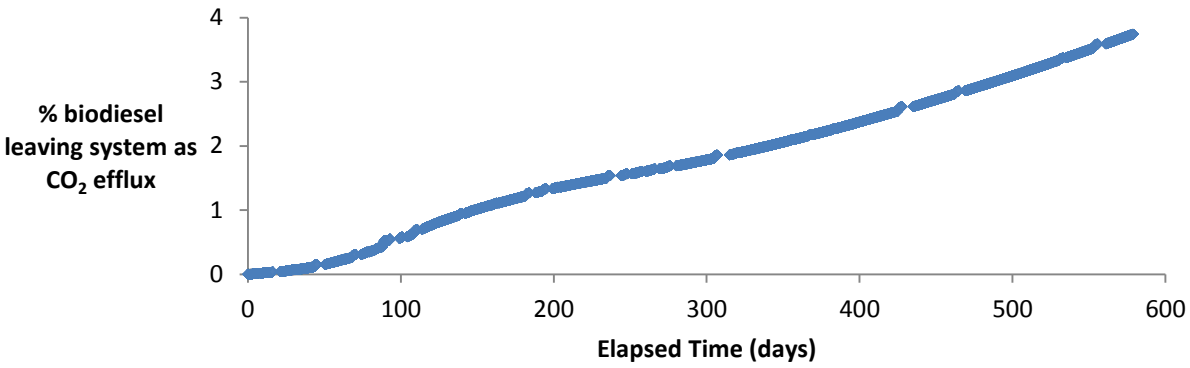

Figure 3-29: Cumulative % of biodiesel leaving system as CO_2 efflux

This calculation was repeated for the CH_4 efflux. It is evident that the amount of carbon leaving the tank as CH_4 was negligible relative to the CO_2 efflux; however, the results were plotted for completeness in Figure 3-30. Indeed, the total biodiesel which has exited the tank as CH_4 to date is only 0.06% of the 80 L initially present in the tank.

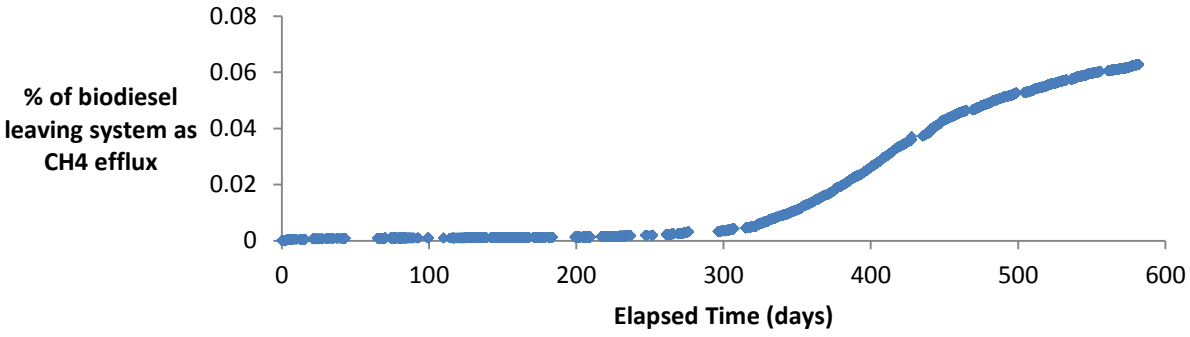

Figure 3-30: Cumulative % of biodiesel leaving system as CH_4 efflux

Finally, VFA production was substantial in the sandtank and therefore it was deemed necessary to calculate the amount of biodiesel transformed to VFAs. Since VFAs in the tank are only present as intermediary products (eventually, the carbon is transformed to CO_2 or CH_4 based on the system of chemical reactions occurring in the tank), the amount of biodiesel converted to VFAs is plotted as a "snapshot" at several times throughout the experiment, showing the % biodiesel-derived carbon held in VFA form at a given time. The VFA concentration obtained from each port was applied over a representative volume of the saturated zone assigned to that port, and the moles of C for each VFA was

calculated based on the molar mass of the compounds. It is assumed that VFA production in the unsaturated zone was negligible. Figure 3-31 shows the % biodiesel as VFA at various stages in the experiment. At most, this value reached 1.0% and the most recent result is 0.5% of the 80 L of biodiesel as VFAs. This is a substantial amount relative to the amount of carbon emitted as CO_2 efflux (3.7%).

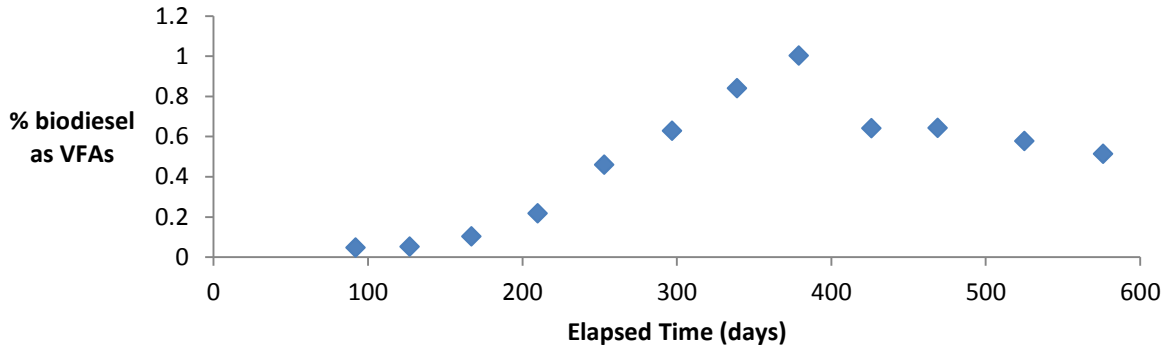

Figure 3-31: snapshots through time of % biodiesel as VFAs

At 590 days into the experiment, it is estimated from these mass balance calculations that only 4.2% of the biodiesel had been transformed to VFAs, CO_2 or CH_4 and only 3.7% had effluxed from the tank as CO_2 or CH_4. Other sources of carbon which may be present in the sandtank due to biodiesel degradation include biomass and dissolved CO_2 (TIC); however, the overall rate of biodiesel degradation was clearly very limited.

(iv) How persistent is biodiesel under the experimental conditions and what is its rate of degradation?

Based on the carbon mass balance results, an attempt was made to estimate an average biodegradation rate for the biodiesel. In this context, it was not possible to distinguish between aerobic and anaerobic degradation rates, since carbon loss from biodiesel involves both saturated and unsaturated zone data, as well as gas effluxes.

The volume used was from the top of the tank to the base of the spill in the center of the tank (which includes the smear zone) and the thickness of the pool for the outskirts of the tank (outside the spill zone). There are 2D effects due to lateral gas transport; however these effects were neglected for this

calculation. A rough rate was estimated based on the surface integrated CO_2 efflux; according to the cumulative biodiesel degraded from CO_2 efflux, this rate was approximately 3.1 x 10^{-6} mol s^{-1} for the entire tank. This value was divided by the volume of sediments impacted by the spill (residual, smear zone and pool) to obtain a rate of 5.0 x 10^{-6} mol m^{-3} s^{-1}. Normalizing to the porosity of the sediments (0.4), where degradation must be occurring, this rate is 1.3 x 10^{-5} mol m^{-3} H_2O s^{-1}, corresponding to 1.3 x 10^{-8} mol L^{-1} H_2O s^{-1}. The full rate calculation can be found in Appendix C.1.

Recall that the estimated rate of dolomite dissolution in the tank was 4.32 x 10^{-6} mol L^{-1} H_2O s^{-1} in acidic regions of the tank. This rate is significantly higher than the rate of biodiesel degradation, which means that dolomite dissolution should just provide ample pH-buffering capacity for the rate calculated. Obviously, there is considerable uncertainty associated with both rate estimates.

The rate of biodiesel biodegradation is comparable to those found in other studies. Zhang et al. (1998) found that the maximum mineralization rate for rapeseed oil biodiesel determined by CO_2 evolution in 2 L aerobic microcosm experiments was 2.4 x 10^{-5} mol m^{-3} s^{-1}, within a factor of 2 of the rate estimated here. This is somewhat faster than what was seen in this experiment; however, the microcosm experiments were conducted at a much smaller scale and under fully oxic conditions. Biodegradation rates for soybean biodiesel and castor oil biodiesel in 100 mL microcosms were 6.4 x 10^{-8} mol L^{-1} H_2O s^{-1} and 1.5 x 10^{-8} mol L^{-1} H_2O s^{-1}, respectively (Corseuil et al., 2011). These rates are slightly faster than what was seen in the sandtank by a factor of 1.2-5. Lisiecki et al. (2013) determined that the rate of biodiesel degradation in inoculated, saturated sandy microcosms was 1.36 x 10^{-7} mol L^{-1} H_2O s^{-1} for a B100 blend, and 3.7 x 10^{-8} mol L^{-1} H_2O s^{-1} for a diesel fuel, as determined by CO_2 evolution. The experiment was run for a similar length of time as the sandtank experiment (578 days). Suflita and Mormile (1993) measured the anaerobic biodegradation rate of ethanol with an initial concentration of 50 mg L^{-1} to be 4.5 x 10^{-9}

mol L^{-1} H_2O s^{-1}, 2.9 times lower than observed here. Overall, the degradation estimates derived here compare favorably with literature data.

Despite the average degradation rate, the biodiesel in this experiment was very persistent due to the relatively large volume applied. It is estimated in section 3.5.1.1 that less than 5% of the biodiesel had been biotransformed by the end of the experiment at 580 days. The rate of biodiesel degradation appears to slow as a result of the precipitation events; since the biodiesel covers the entire water table, the precipitation events likely caused water to pool on the biodiesel. If the water was not able to overcome the displacement entry pressure of the biodiesel, it would remain above the biodiesel and form a layer which prevented O_2 from reaching the substrate and degrading the fuel. This would have significant repercussions for the long-term rate of biodiesel degradation, since below the perched water table, where most of the biodiesel is present, conditions would quickly become anoxic. Anaerobic degradation rates are much slower than aerobic rates. However, it still should be possible for biodiesel degradation to proceed in the vadose zone, where the fuel is present at residual saturation. This appears to have been sufficient to maintain reasonably fast degradation rates in the sandtank overall.

Typically, a high moisture content is considered a problem if it shuts out O_2; this does not seem to be the case in most of the sandtank; however, since O_2 concentrations remain high across all ports and sensors. Nevertheless, the pool of biodiesel in the capillary fringe, which likely contained the majority of the 80 L of biodiesel (approximately 48 L, but calculations range from 16 to 64 L), may have been covered by the water from the precipitation event, which would have limited O_2 ingress into that region. This cannot be verified, since the biodiesel pool is lower in the sandtank than the lowest sensors.

As mentioned, there may be a chemical reason for the decrease in CO_2 production following the precipitation event; however, the water used in the precipitation events was identical to the initial water in the sandtank (i.e. Vancouver tap water amended with Nutrafin™).

(v) What is the composition and magnitude of surface gas effluxes above and in the vicinity of the spill?

The composition of surface gas effluxes in the vicinity of the spill is clearly dominated by CO_2. The CO_2 flux initially increased to around 4.2 µmol $m^{-2} s^{-1}$ before a rapid decrease which coincided with the first precipitation event. The CO_2 effluxes seemed to reach a quasi-steady state ranging between 0.5 and 2 µmol $m^{-2} s^{-1}$; values increased according to the proximity of the chamber to the spill zone. The first signs of CH_4 effluxes began around 145 days into the experiment. The first signs of CH_4 generation according to the Varian GC analysis began approximately 250 days into the experiment. Similarly to the CO_2 flux, the CH_4 flux increased relatively rapidly and then decreased after around 400 days. By the 590 day mark, the flux seemed to have reached a steady-state ranging between 0.01 and 0.03 µmol $m^{-2} s^{-1}$.

In the source zone of the Bemidji field site described above, average CO_2 effluxes were estimated to be 2.6 µmol $m^{-2} s^{-1}$ (Sihota and Mayer, 2012). At a rail line in Balaton, a large release of EtOH denatured with 5% gasoline and soybean oil. CO_2 effluxes ranged from 0.6 to 178.4 µmol $m^{-2} s^{-1}$. CH_4 effluxes were above 0.3 µmol $m^{-2} s^{-1}$ in 25 locations and reached a maximum value of 9.1 µmol $m^{-2} s^{-1}$ (Sihota et al., 2013). At a site in Cambria in the Minnesota River valley, a large release of DFE occurred following a multi-railcar derailment in November, 2006. CO_2 effluxes ranged from 0.5 to 179 µmol $m^{-2} s^{-1}$ and CH_4 effluxes ranged from 0.2 to 393 µmol $m^{-2} s^{-1}$ (Sihota et al., 2013).

There are many reasons that these results would be different. First these describe different fuel types than biodiesel: the first two were ethanol blended fuel spills and Bemidji examined a crude oil spill. Studies which measured CO_2 effluxes from biodiesel were not found. It should also be noted that these large field spills occurred in 2004 and 2006 in Balaton and Cambria, respectively, therefore the microbial populations have had significant time to establish themselves in the subsurface relative to the sandtank experiment which lasted only 590 days. The soil type in Balaton was silty sand, and in Cambria was a silty loam, therefore O_2 ingress from the atmosphere into the subsurface would have been slower than

in the sandtank and may have allowed anoxic conditions to occur more readily. It should be noted that at these sites CH_4 was generated below the water table and seasonal effects were difficult to quantify. Largely, the scale of the site and volume of spill was much larger at these sites, making a comparison with results from a laboratory experiment difficult.

(vi) Based on subsurface gas concentrations, what is the risk for soil vapor intrusion of CH_4 in response to biodiesel spills?

The dominant gas transport process in the sandtank is likely diffusion as confirmed by the steady concentrations of Ar and N_2. These are typically considered non-reactive and conservative gases, and their concentrations would be expected to change due to biogenic gas production if diffusion were not the dominant process. According to Molins and Mayer (2007), gas-phase diffusion occurs at velocities approximately four orders of magnitude faster than liquid diffusion and is the dominant transport process in the unsaturated zone under most natural settings. Due to the highly labile nature of biodiesel compounds, degradation may occur relatively quickly and, as seen here, methanogenesis will begin in anaerobic zones.

Methane generation is a serious concern due to the explosion risk of this gas. Methane can pose an explosion risk when it accumulates in air at concentrations between 50,000 and 150,000 ppm_v (Bjerkevedt et al., 1997). CH_4 concentrations in this experiment were significantly lower than these values (maximum values of 800 ppm); therefore the risk is low according to these results. However, the results also indicate that acidic conditions in the vadose zone may decrease rates of methane oxidation. At a site with higher CH_4 production and high acidity in the vadose zone, CH_4 intrusion could be a greater concern.

Under these experimental conditions, CO_2 and CH_4 gas fluxes generated by biodiesel degradation were limited, suggesting a low risk for soil vapor intrusion. However, several circumstances have to be taken

into consideration before drawing generally applicable conclusions. First, although the dimensions of the experiment and the volume of biodiesel applied were relatively large, they are still much smaller than at many spills occurring in the field. Larger dimensions, a deeper vadose zone, and less permeable sediments will likely increase the fluxes or affect the ratio between the CO_2 and CH_4 effluxes at field sites and increase vapor intrusion issues. In addition, low pH conditions and slow microbial acclimatization may have limited degradation rates in this experiment.

3.5.3 Secondary Impacts due to TEAPs

(vii) What are the secondary impacts of biodiesel degradation on aqueous and gaseous geochemistry in the spill zone?

The main secondary impact of biodiesel degradation was the impact on water quality. An abundance of degradable substrate may cause the aerobic and acidogenic bacteria to multiply and produce acids rapidly. The aerobic and acidogenic bacteria typically reproduce quickly given enough substrate. The methanogenic bacteria, which take longer to increase their populations, may be unable to consume the acids at the same pace. This scenario causes the pH of the system to drop, killing more of the methanogenic bacteria and leading to a positive feedback loop. An early indication of this in a sludge digester is low CH_4 production and eventually a lower pH (Van Rollegham 2003). In the sandtank, both pH and methane formation were monitored. As discussed, both parameters were low.

In the vadose zone, aerobic degradation likely generated significant acidity which migrated toward the saturated zone. In the saturated zone, acidity from the unsaturated zone as well as high VFA production seem to have lowered the pH enough to slow methanogenesis. The slow CH_4 production may have been aggravated by reductive dissolution reactions, as evidenced by the increase in Fe and Mn concentrations in the saturated zone; however, these species may also be in solution due to the dissolution of ankerite-dolomite phases in the sediment grains.

Clean Vancouver tap water with low initial EC was used in this experiment, and results showed evidence of degrading water quality. Aerobic degradation of biodiesel in the vadose zone appears to have generated significant acidity based on the vertical pH profiles. Unfortunately, it was not possible to obtain aqueous samples above the 50 cm horizontal transect in the sandtank. Still, the zone at 50 cm appears to be a mixing zone where acidity from the vadose zone moves downward and VFAs from the saturated zone migrate upward. VFA production was very high in the saturated zone, and led to the generation of acidity in the capillary fringe and below the water table. The pH of the water decreased significantly, with minimum values of 4.5 in the center of the tank near the biodiesel pool.

The acidity had significant consequences related to dissolution of buffering minerals in the sediments, leading to increased concentrations of several major cations including Ca^{2+}, Mg^{2+}, and possibly also Fe^{2+} and Mn^{2+}. Further pH decreases may have mobilized larger amounts of Al^{3+}. In sediments with large concentrations of more dangerous metals, such as As or Pb, this may have significant health repercussions for organisms dependent on the water.

In Chapter 4, two reactive transport simulations are compared to help determine the origin of the Fe^{2+} and Mn^{2+} in the sandtank water; it is hypothesized that amorphous Fe and Mn oxides present in the tank are providing electron acceptors undergoing reductive dissolution, or that ankerite dissolution is buffering the pH and releasing Fe and Mn over time.

4 Preliminary Reactive Transport Modeling Analysis

The results of the sandtank laboratory experiment from Chapter 3 were used to create two preliminary 2D reactive transport models using the MIN3P code (Mayer et al., 2002) which include multicomponent gas transport, solute transport, and relevant biogeochemical reactions. The systems of reactions began with the dissolution of biodiesel, followed by aerobic and anaerobic degradation reactions coupled with sequential electron acceptor consumption. The ingress of atmospheric O_2 and the release of CH_4 and CO_2 from the smear zone generated by the biodiesel were considered. The models are described in more detail in the following sections.

The MIN3P code has been used previously for several similar applications; e.g.: Molins et al. (2010) used the code to integrate a large field data set from a crude oil spill site with a focus on vadose zone processes, and Sihota et al. (2011) used MIN3P to simulate reactive gas transport at a hydrocarbon spill constrained by stable carbon isotopes, radiocarbon, and CO_2 efflux data.

4.1 Model Formulation

The models describe a two-dimensional cross-section of the sandtank under variably saturated, steady state flow conditions including reactive transport. The biodiesel was modeled as an immobile phase which dissolves, and subsequently diffuses into the surrounding water and undergoes degradation. The starting point for the model was after the biodiesel had been injected and reached a quasi-steady state distribution - the injection itself was not simulated. This is a reasonable approximation since observations have shown that it only took a few days for the biodiesel to reach a steady-state distribution, and reaction progress during that time would be negligible relative to the length of the experiment. The steady-state distribution was inferred when the visual migration of LNAPL dyed red with Sudan IV had stopped.

Since the water table was held constant at 30 cm from the base of the tank, advective solute transport was not considered in this simulation. Furthermore, the precipitation events and nutrient addition event were not included in the simulation since capturing the complex transient effects were beyond the scope of this analysis.

In the center of the tank, the biodiesel was assumed to be present at residual saturation where it has filtered down to the water table. It was approximated as a pool on the water table. The simulated tank area was 400 cm wide and 150 cm tall. The water table was set at 30 cm from the bottom. The domain was discretized in a 4 cm x 4 cm mesh (i.e. the control volumes were set up in a 101 x 38 grid). The 80 L of biodiesel applied at surface was accounted for using the dimensions/residual content values shown in Figure 4-1.

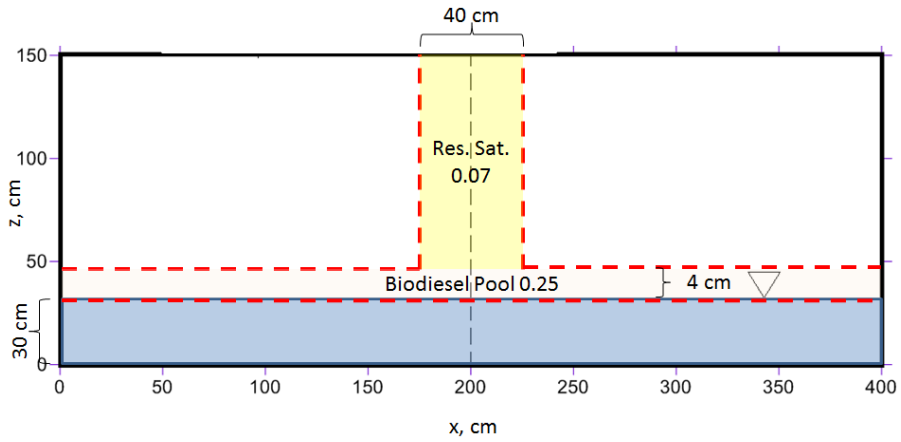

Figure 4-1: Biodiesel distribution content values for model

The dimensions are approximate and were determined by measuring the biodiesel extent seen through the glass panel of the sandtank. The residual saturations have been estimated based on reasonable values from the literature for medium sand, and adjusted based on the known volume of biodiesel present in the tank.

The two models are very similar besides the mineral reactions, which are adjusted based on two potential sources for the increased Fe and Mn concentrations in the sandtank. In Model A, Fe and Mn

oxides are reduced via microbially mediated degradation reactions. Siderite and rhodochrosite serve as solubility controls for Fe and Mn in solution. In Model B, the dissolution of ankerite-dolomite is investigated as a source of observed Fe and Mn. In all likelihood, the sandtank experiment underwent some combination of these reactions, and possibly other reactions which would explain the increased concentrations of these elements. For this chapter, these two hypothetical reaction networks were simulated and the results of the two endmember models were compared. This experiment is a good example for challenges with data interpretation due to non-uniqueness.

4.1.1 Conceptual Model

The first stage of both models involves the hydrolysis of free-phase biodiesel, which releases the biodiesel into the surrounding water, represented as a readily degradable sugar ($C_6H_{12}O_6$).

The geochemical reaction network includes four general reactions which degrade the biodiesel or occur in response to the biodiesel degradation:

(i) aerobic degradation of biodiesel

(ii) intermediary fermentation reactions which produce VFAs

(iii) Fe and Mn reactions

   a. reduction of iron and manganese oxides (model A)

   b. dissolution of ankerite-dolomite (model B)

(iv) biodegradation of biodiesel and/or VFAs via methanogenesis

These four general types of reactions were inputted in the models using a variety of experimentally derived rate expressions. Monod and inhibition terms were used to describe microbially-mediated reactions or to limit the reaction progress of inorganic reactions. The conceptual model of the reaction network is described in more detail in the following sections.

4.1.1.1 Biodiesel Hydrolysis

Since biodiesel is a fairly complex molecule, the first step in the models is to force the biodiesel to undergo hydrolysis and form a simpler organic molecule, $C_6H_{12}O_6$ via the following reaction:

$$C_{16}H_{32}O_2 + 7O_2 \rightarrow 2.667C_6H_{12}O_6$$

Without the presence of O_2, this reaction becomes:

$$C_{16}H_{32}O_2 + 14H_2O \rightarrow 2.667C_6H_{12}O_6 + 14H_2(aq)$$

This reaction also simulates the biodiesel dissolution into the surrounding water, mobilizing the organic contaminant.

4.1.1.2 Aerobic degradation

Next, the simpler glucose molecule is aerobically degraded with O_2 to form CO_2 and H_2O via the following equation:

$$C_6H_{12}O_6 + 6O_2(aq) \rightarrow 6{CO_3}^{2-} + 12H^+$$

Aerobic degradation should be occurring first. Aerobic degradation continues to occur throughout the experiment in the unsaturated zone of the sandtank, since O_2 ingress is fast enough to maintain oxic conditions in this zone. To account for delays in the onset of certain reactions associated with microbial growth, an "inhibition" variable is used at the start of the experiment. The inhibitory component is steadily degraded via an independent reaction and eventually reaches a level that allows biodegradation reactions to proceed more rapidly.

4.1.1.3 Acidogenesis

As O_2 levels drop, the organic carbon molecule may undergo fermentation reactions to produce acetate and eventually (once acetate concentrations have reached solubility) other VFAs including propionate and butyrate. The following three reactions show the stoichiometric chemical equations for the production of acetate, propionate and butyrate, respectively.

$$C_6H_{12}O_6 + 4H_2O \rightarrow 2CH_3COO^- + 6H^+ + 4H_2(aq) + 2{CO_3}^{2-}$$

$$C_6H_{12}O_6 + 2H_2(aq) \rightarrow 2CH_3CH_2COO^- + 2H^+ + 2H_2O$$

$$2C_6H_{12}O_6 + 6H_2(aq) \rightarrow 3CH_3CH_2CH_2COO^- + 3H^+ + 6H_2O$$

As acetate levels decrease, propionate and butyrate are converted to acetate via the following reactions:

$$CH_3CH_2COO^- + 3H_2O \leftrightarrow CH_3COO^- + 2H^+ + {CO_3}^{2-} + 3H_2(aq)$$

$$CH_3CH_2CH_2COO^- + 3H_2O \leftrightarrow CH_3CH_2COO^- + 2H^+ + {CO_3}^{2-} + 3H_2(aq)$$

4.1.1.4 Mineral Reactions

Dissolution-precipitation reactions can be described as surface-controlled or transport-controlled reactions; in this model, surface-controlled reactions were used. The reaction pathways are considered to be occurring in parallel and were specified as irreversible or reversible processes.

4.1.1.4.1 Model A

In Model A, it was assumed that the reduction of Fe and Mn hydroxides accepts electrons during biodiesel degradation at later stages, and simultaneously acts as a pH-buffer due to the tendency of these reactions to consume acidity. The reductive dissolution rates of iron oxides and manganese oxides were increased until a good match was observed with the cation concentrations in the water. Experimental data showed high levels of Fe (5-60 ppm) and Mn (20-200 ppm). For these reactions to proceed, some regions of the sandtank must have been anoxic. These reactions were modeled as irreversible reactions, controlled by an O_2-inhibition term.The balanced chemical formulae are:

$$Fe(OH)_3 + 0.125CH_3COO^- + 1.625H^+ \rightarrow Fe^{2+} + 0.25{CO_3}^{2-} + 2.5H_2O$$

$$MnO_2 + 0.25CH_3COO^- + 1.25H^+ \rightarrow Mn^{2+} + 0.5{CO_3}^{2-} + H_2O$$

Although the XRD analysis did not report the presence of Fe and Mn oxides in the sand, these phases may still exist in the sandtank. If they are present below the detection limit of the instrument (approximately 0.5%) or if they are present as amorphous phases, the Fe and Mn oxides would not show up on the sediment analysis report. As a result there is a good chance that these minerals were present

in the sediments. At many contaminated sites, the anaerobic zone is large and Fe(III) is generally the most abundant electron acceptor for organic matter oxidation in such a system (Anderson et al., 1998).

Higher concentrations of Fe were strongly correlated with the nutrient addition event and less strongly correlated with pH values. These results point to Fe oxide reduction as the source of dissolved Fe over mineral dissolution due to pH buffering.

According to simulations completed in PHREEQCi, chemical conditions at several ports (including temperature, pH, pE, alkalinity and species concentrations) were such that minerals such as siderite ($FeCO_3$) and rhodochrosite ($MnCO_3$) were saturated and likely to be precipitating on the sediment grains. The input and results of the PHREEQCi simulations can be found in Appendix B. The equilibrium reactions for siderite and rhodochrosite were included in Model A and are shown below.

$$FeCO_{3(am)} \leftrightarrow Fe^{+2} + {CO_3}^{-2}$$

$$MnCO_{3(am)} \leftrightarrow Mn^{+2} + {CO_3}^{-2}$$

The concentrations of Fe and Mn will be balanced by the precipitation of Fe as siderite ($FeCO_3$) or Mn as rhodochrosite ($MnCO_3$). Since this provides a sink for Fe and Mn, the rates of Fe and Mn oxide reduction may be an overestimate; however, since other parameters were considered in the calibration (e.g. pH), the rates are assumed to be reasonable.

4.1.1.4.2 Model B

Fe and Mn may also be produced via ankerite dissolution. Aerobic degradation in the vadose zone and the generation of organic acids in the saturated zone may have lowered the pH of the water and enhanced dissolution of the ankerite-dolomite phase. Ankerite dissolution is expected in areas where the pH decreases.

Model B assumed that the ankerite-dolomite found in the sediment analysis (approximately 0.9% by volume) provided the main mechanisms for pH buffering of the system as well as elevated

concentrations of Ca, Mg, Mn and Fe. The balanced chemical reaction for ankerite dolomite dissolution is:

$$Ca(Mg, Mn, Fe)CO_3 \rightarrow Ca^{2+} + 0.4Mg^{2+} + 0.3Mn^{2+} + 0.3Fe^{2+} + 2{CO_3}^{2-}$$

The stoichiometry of the reaction was assumed based on the average concentrations of Ca^{2+}, Fe^{2+}, Mn^{2+} and Mg^{2+} seen in the experimental results.

4.1.1.5 Methanogenesis

Methanogenesis is also occurring in some regions of the sandtank. These reactions were inputted at low kinetic rates. Methanogenesis tends to occur if all other electron acceptors are depleted. It can occur via one of two pathways in this simulation. The first is methanogenesis via CO_2 reduction, as shown in the equation:

$${CO_3}^{2-} + 4H_2(aq) + 2H^+ \leftrightarrow CH_4(aq) + 3H_2O$$

Or acetogenesis consumes acetate to produce CH_4:

$$CH_3COO^- + H_2O \leftrightarrow CH_4(aq) + {CO_3}^{2-} + H^+$$

Currently, the pH in the water of the sandtank ranges from 4.5 (near the water surface and the biodiesel-water interface) to 6.1 in the lower ports. This meant that the model required pH inhibition in areas where the water became too acidic for the microbes.

4.1.1.6 Degassing reactions

The partitioning of gases from soil air into soil water is assumed linear, instantaneous, and is described by Henry's Law. Hydrophobic compounds tend to accumulate at the gas-water interface; however, this area is small in sands, therefore this effect is less important (Aelion, 2009). Sorption may be important for hydrophobic compounds with lower partial pressures (Aelion, 2009).

The degassing reactions occurring in the sandtank involve gas exchange of O_2, CO_2, CH_4 and H_2. The balanced chemical reactions are:

$$O_{2(aq)} \leftrightarrow O_{2(g)}$$

$$CO_3{}^{-2} + 2H^+ - H_2O \leftrightarrow CO_{2(g)}$$

$$CH_{4(aq)} \leftrightarrow CH_{4(g)}$$

$$H_{2(aq)} \leftrightarrow H_{2(g)}$$

In a multi-phase system, components move between the gaseous and aqueous phases as defined by Henry's Law for a constant temperature:

$$p_g = K_H C$$

Where p_g is the partial pressure of the compound in the gas phase, K_H is the Henry's Law Constant for the compound, and C is the concentration of the compound in the aqueous phase. The units of the Henry's Law Constant K_H are m^3 atm mol^{-1}.

4.1.2 Initial Conditions and Boundary Conditions

Table 4-1 shows the physical parameters used in the input file for the model. The distance parameters were selected based on the physical size of the sandtank. The simulation time is the approximate length of the experiment.

Table 4-1: Physical input parameters for both simulations

Parameter	Symbol	Value	Unit
Length	L	4	m
Height	H	1.5	m
Cross sectional area	A	6	m^2
Spatial discretization	Δx	0.04	m
Simulation time	T	590	day
Maximum time step	Δt_{max}	1	day
Porosity	N	0.4	[-]
Hydraulic conductivity	K	1.2d-4	m s^{-1}
Residual saturation	S_r	0.032	[-]
Alpha (Van Genuchten)	A	10.1	m^{-1}
N (Van Genuchten)	N	2.2255	[-]
Free diffusion coefficient – water	D_w	2.38d-9	m^2 s^{-1}
Free diffusion coefficient – air	D_a	2.07d-5	m^2 s^{-1}
Longitudinal dispersivity	α_L	5.0d-2	m
Vertical transverse dispersivity	α_T	1.0d-3	m

The spatial discretization of 4 cm was deemed adequate to properly delineate processes occurring in the sandtank without causing unreasonable simulation times. The porosity, hydraulic conductivity and residual saturation were determined experimentally as described in Chapter 2. The free diffusion coefficients and dispersivities were assumed based on reasonable values for sand. The soil hydraulic function parameters were adjusted to match the volumetric water content results described in section 3.1. These parameters caused an initial water saturation profile as shown in Figure 4-2. For simplicity, the effect of the presence of the biodiesel on water saturations was neglected.

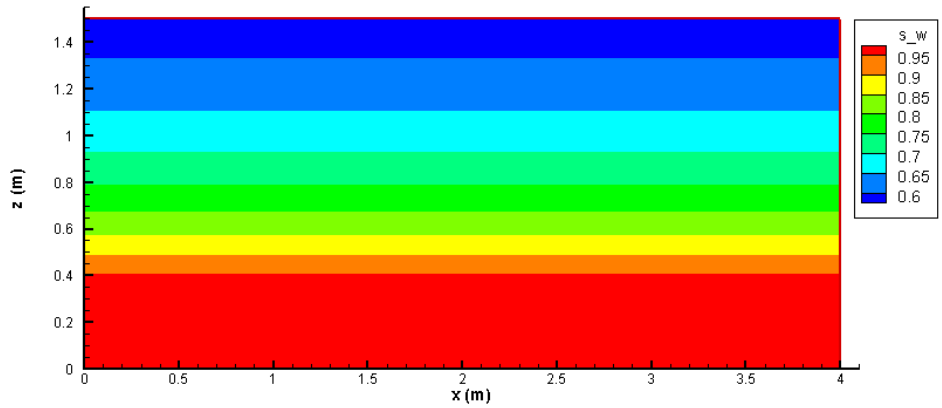

Figure 4-2: Water saturation profile at the start of the simulations

The flow boundary conditions for each side of the simulation are shown in Figure 4-3. The bottom of the sandtank is a no flow boundary as well as the sides of the sandtank for the top 1.2 m. The bottom 0.3 m of the sandtank sides are a type 1 (constant head) boundary where h=30 cm. The front and rear panels of the sandtank would also be modeled as no flow boundaries in a three dimensional model. The top of the sandtank is a specified flux boundary (specified flux = 0).

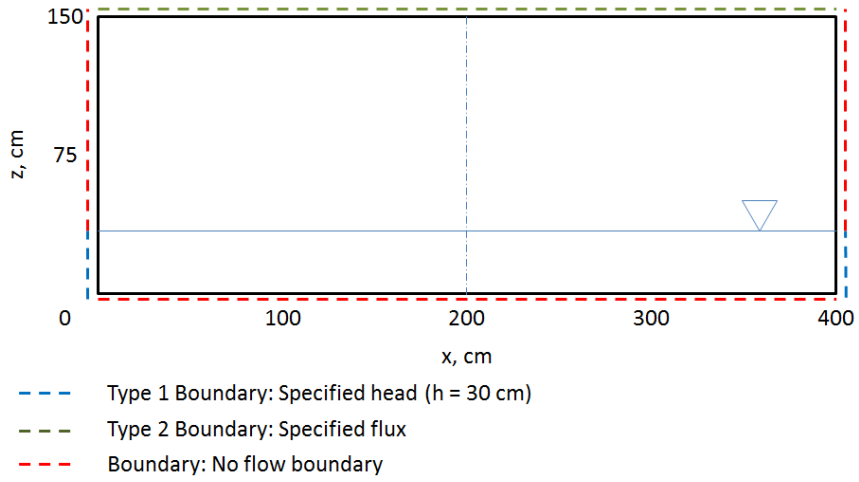

Figure 4-3: Flow boundary conditions for both simulations

The reactive transport boundary conditions are shown in Figure 4-4. The top of the sandtank is open to the atmosphere and considered a constant concentration boundary with atmospheric gas chemistry (first type boundary condition). Since the gas flux is diffusive and the concentration at the top are fixed, this will provide a control for the gas efflux calculations for the model. The bottom 0.3 m of the sandtank on both sides is modeled as a free exit boundary, and the top 1.2 m of the sandtank sides as well as the bottom are zero mass flux boundaries.

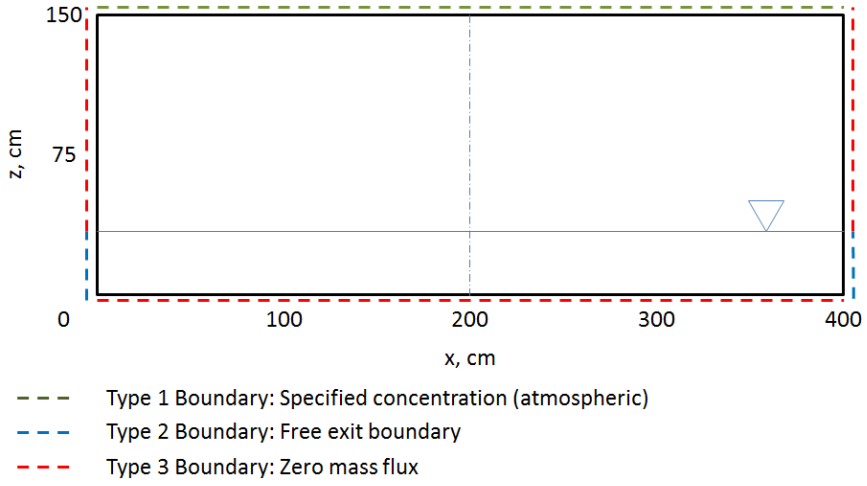

Figure 4-4: Reactive transport boundary conditions for both simulations

Since the water table is set at 30 cm across the entire tank, there is no advective flow in the system and the main mode of transport for components will be via diffusion (both gaseous and aqueous phase

diffusion). For a dilute diffusing gaseous compound in a bulk phase, Fick's Law is valid and widely applied; however, some VOCs are not dilute enough to obey Fick's Law (Thorstenson and Pollock, 1989). This model assumes that Fick's Law provides an adequate representation of the diffusive transport occurring in the sandtank.

Table 4-2 shows a list of the chemical components present in the sandtank and their initial concentration values at all locations in the tank. The fixed concentration of each species at the boundary at the top of the tank is also recorded.

Table 4-2: Boundary conditions concentrations and initial concentrations for aqueous components

Species	Initial Condition	Boundary Condition
pH	6.5	6.5
pE (as O_2 (aq) or pO_2)	-2.5	0.21
CO_3^{2-}	1.6d-5	1.6d-5
$C_6H_{12}O_6$	1.0d-10	1.0d-10
CH_4(aq)	1.0d-10	1.0d-10
Acetate	1.0d-10	1.0d-10
Propionate	1.0d-10	1.0d-10
Butyrate	1.0d-10	1.0d-10
H_2(aq)	1.0d-10	1.0d-10
Fe^{+2}	1.0d-10	1.0d-10
Mn^{+2}	1.0d-10	1.0d-10
Mg^{+2} (Model B)	1.0d-10	1.0d-10
Ca^{+2} (Model B)	1.0d-10	1.0d-10
Inhibition component accounting for microbial growth	1.0d-5	-

All aqueous concentrations are in mol L^{-1} and gaseous concentrations are pressure in atm, pH is unitless.

4.1.3 System of Chemical Reactions

Table 4-3, Table 4-4, Table 4-5 and Table 4-6 describe the systems of intra-aqueous chemical reactions, gas dissolution-exsolution reactions, aqueous complexation reactions and mineral reactions taking place in the sandtank simulations. Reaction coefficients were calibrated to match the experimental data. Reactions coefficients and equilibrium constants for each reaction are shown.

Table 4-3: System of intra-aqueous chemical reactions in Models A and B

Name	Reaction	Reaction Coefficients	Units	Remarks
Aerobic oxidation	$C_6H_{12}O_6+6O_{2(aq)}\rightarrow 6CO_3^{2-}+12H^+$	8.96E-4	mol L^{-1} s^{-1}	Irreversible
Acetate formation	$C_6H_{12}O_6+4H_2O\rightarrow 2CH_3COO^-+6H^++2CO_3^{2-}+4H_{2(aq)}$	3.46E-5	mol L^{-1} s^{-1}	Irreversible
Propionate formation	$C_6H_{12}O_6+2H_{2(aq)}\rightarrow 2CH_3CH_2COO^-+2H^++2H_2O$	1.46E-5	mol L^{-1} s^{-1}	Irreversible
Butyrate formation	$2C_6H_{12}O_6+6H_{2(aq)}\rightarrow 3CH_3(CH_2)_2COO^-+3H^++6H_2O$	3.96E-6	mol L^{-1} s^{-1}	Irreversible
Propionate degrad.	$CH_3CH_2COO^-+3H_2O\rightarrow CH_3COO^-+2H^++CO_3^{2-}+3H_{2(aq)}$	9.16E-8	mol L^{-1} s^{-1}	Irreversible
Butyrate degrad.	$CH_3(CH_2)_2COO^-+3H_2O\rightarrow CH_3CH_2COO^-+2H^++CO_3^{2-}+3H_{2(aq)}$	5.16E-9	mol L^{-1} s^{-1}	Irreversible
Methanogenesis	$CO_3^{2-}+4H_{2(aq)}+2H^+\rightarrow CH_{4(aq)}+3H_2O$	1.16E-10	mol L^{-1} s^{-1}	Irreversible
Acetate fermentation	$CH_3COO^-+H_2O\rightarrow CH_{4(aq)}+H^++CO_3^{2-}$	3.16E-10	mol L^{-1} s^{-1}	Irreversible
Inhibition (microbial)	$I\rightarrow 0$	3.70E-12	mol L^{-1} s^{-1}	Irreversible

Table 4-4: System of gas dissolution-exsolution reactions in Models A and B

Name	Reaction	Henry's Constant	Units	Remarks
$O_{2(g)}$ dissolution-exsolution	$O_{2(aq)}\leftrightarrow O_{2(g)}$	2.898	mol L^{-1} atm^{-1}	Henry's Law
$CO_{2(g)}$ dissolution-exsolution	$CO_3^{2-}+2H^+-H_2O\leftrightarrow CO_{2(g)}$	18.16	mol L^{-1} atm^{-1}	
$CH_{4(g)}$ dissolution-exsolution	$CH_{4(aq)}\leftrightarrow CH_{4(g)}$	2.8894	mol L^{-1} atm^{-1}	Henry's Law
$H_{2(g)}$ dissolution-exsolution	$H_{2(aq)}\leftrightarrow H_{2(g)}$	-13.6337	mol L^{-1} atm^{-1}	Henry's Law

Table 4-5: System of aqueous complexation reactions in Models A and B

Name	Reaction	Equilibrium Constant	Units	Remarks
OH^-	$OH^-+H^+\rightarrow H_2O$	log K_{25}=-14.0	-	
HCO_3^-	$HCO_3^-\rightarrow H^++CO_3^{2-}$	log K_{25}=10.33	-	
$H_2CO_{3(aq)}$	$H_2CO_{3(aq)}\rightarrow 2H^++CO_3^{2-}$	log K_{25}=16.68	-	
Propionate	$CH_3CH_2COOH_{(aq)}\rightarrow CH_3CH_2COO^-+H^+$	log K_{25}=4.87	-	
Butyrate	$CH_3(CH_2)_2COOH_{(aq)}\rightarrow CH_3(CH_2)_2COO^-+H^+$	log K_{25}=4.73	-	
Acetate	$CH_3COOH_{(aq)}\rightarrow CH_3COO^-+H^+$	log K_{25}=4.76	-	

Table 4-6: System of mineral reactions in Models A and B

Name	Reaction	Reaction Coefficients	Units	Remarks
$C_{16}H_{32}O_2$(f)	$C_{16}H_{32}O_{2(f)}+14H_2O\rightarrow 2.667C_6H_{12}O_6+14H_{2(aq)}$	1.0d-9 Initial vol: Figure 4-1	mol L^{-1} s^{-1}	Irreversible dissolution
Model A				
Acetate + $Fe(OH)_3$	$Fe(OH)_{3(s)}+0.125CH_3COO^-+1.625H^+\rightarrow Fe^{2+}+0.25CO_3^{2-}+2.5H_2O$	1.0d-9 Initial vol: 0.015	mol L^{-1} s^{-1}	Irreversible dissolution
Acetate + MnO_2	$MnO_{2(s)}+0.25CH_3COO^-+1.25H^+\rightarrow Mn^{2+}+0.5CO_3^{2-}+H_2O$	1.0d-9 Initial vol: 0.009	mol L^{-1} s^{-1}	Irreversible dissolution
Siderite(d)	$FeCO_{3(am)}\leftrightarrow Fe^{2+}+CO_3^{2-}$	1.0d-8 log K_{25}=10.45 Initial vol: 0.0	mol L^{-1} s^{-1}	Surface, reversible
Rhodochrosite	$MnCO_{3(am)}\leftrightarrow Mn^{2+}+CO_3^{2-}$	1.0d-8 log K_{25}=10.41 Initial vol: 0.0	mol L^{-1} s^{-1}	Surface, reversible
Model B				
Dolomite	$Ca(Mg,Fe,Mn)(CO_3)_2\leftrightarrow Ca^{2+}+0.4Mg^{2+}+0.3Mn^{2+}+0.3Fe^{2+}+2CO_3^{2-}$	1.0d-9 log K_{25}=17.09 Initial vol: 0.009	mol L^{-1} s^{-1}	Surface, reversible

Since many of these reactions are microbially mediated, a multiplicative Monod-type formulation was used (Borden and Bedient, 1986) which allows consideration of the availability of substrate and electron acceptors. Inhibition and toxicity effects due to the presence of certain substances can also be considered using this formulation. These terms for each reaction are shown in Table 4-7.

Table 4-7: Hyperbolic and inhibition terms for chemical reactions

Name	Hyperbolic Terms (mol L^{-1})	Inhibition Terms (mol L^{-1})
Intra-aqueous chemical reactions		
Aerobic oxidation	$C_6H_{12}O_6$: K_h = 1.0E-4 $O_{2(aq)}$: K_h = 1.0E-3	H^+: K_i = 3.0E-6
Acetate formation	$C_6H_{12}O_6$: K_h = 1.0E-4	H^+: K_i = 3.0E-6 $O_{2(aq)}$: K_i = 3.125E-5 I: K_i =1.0E-8
Propionate formation	$C_6H_{12}O_6$: K_h = 1.0E-4 $H_{2(aq)}$: K_h = 1.0E-5	H^+: K_i = 3.0E-6 $O_{2(aq)}$: K_i = 3.125E-5 I: K_i =1.0E-8
Butyrate formation	$C_6H_{12}O_6$: K_h = 1.0E-4 $H_{2(aq)}$: K_h = 1.0E-6	H^+: K_i = 3.0E-6 $O_{2(aq)}$: K_i = 3.125E-5 I: K_i =1.0E-8
Propionate degradation	$CH_3CH_2COO^-$: K_h = 1.0E-4	H^+: K_i = 3.0E-6 $O_{2(aq)}$: K_i = 3.125E-5 I: K_i =1.0E-8
Butyrate degradation	$CH_3(CH_2)_2COO^-$: K_h = 1.0E-5	H^+: K_i = 3.0E-6 $O_{2(aq)}$: K_i = 3.125E-5 I: K_i =1.0E-8
Methanogenesis	$H_{2(aq)}$: K_h = 5.0E-5 CO_3^{2-}: K_h = 5.0E-5	$O_{2(aq)}$: K_i = 3.125E-6 I: K_i =1.0E-8
Acetate fermentation	CH_3COO^-: K_h = 5.0E-4	$O_{2(aq)}$: K_i = 3.125E-6 I: K_i =1.0E-8
Inhibition (microb. growth)	I: 1.0E-5	N/A
Mineral reactions		
$C_{16}H_{32}O_2$(f)	N/A	N/A
Acetate + $Fe(OH)_3$	CH_3COO^-: K_h = 1.0E-3 H^+: K_h = 1.0E-6	$O_{2(aq)}$: K_i = 1.0E-6 I: K_i =1.0E-8
Acetate + MnO_2	CH_3COO^-: K_h = 1.0E-3 H^+: K_h = 1.0E-6	$O_{2(aq)}$: K_i = 1.0E-6 I: K_i =1.0E-8
Siderite(d)	N/A	N/A
Rhodochrosite	N/A	N/A

The terms were assumed; hyperbolic terms were chosen to ensure that reasonable concentrations of reactants were present for the reactions to proceed. Inhibition terms were assumed based on known species which, when present, would make the reaction thermodynamically unfavourable (typically from

a redox perspective, e.g. O_2 is the preferred electron acceptor when present in the system and would slow the progress of other oxidation-reduction reactions). An attempt was made to keep the model as simple as possible, so terms were set to the same value across different reactions in many cases.

The rate of each reaction can be calculated using the following equation:

$$R = -k * [\frac{T}{{K_h}^s + T} * \frac{{K_i}^j}{{K_i}^j + T}]$$

Where k is the rate of the reaction in mol L^{-1} H_2O s^{-1} for aqueous reactions and in mol L^{-1} bulk s^{-1} for mineral reactions. T is the total concentration of the component [mol L^{-1} H_2O], K_h is the half saturation constant [mol L^{-1} H_2O], and K_i is a constant allowing the consideration of inhibition by a particular component [mol L^{-1} H_2O]. Each rate can be inhibited by or dependent on multiple components. The exponential terms, j and s, can be used as numerical controls to prevent depletion of a component.

4.2 Model A Results

The results of the Model A simulation, which included the reductive dissolution of Fe and Mn oxides, are described in this section. Note that this is a preliminary model with a complex system of chemical reactions.

4.2.1 Gaseous Species

An acceptable fit was achieved for the data obtained from the sandtank based on the Model A results. Figure 4-5 shows the simulated concentrations of O_2, CO_2 and CH_4 in the vadose zone of the sandtank.

Considering the complexity of the reaction network, the simulated data provides a reasonably good approximation of the concentrations seen in the sandtank for each gas. This is corroborated by the mass balance results in section 4.2.3, which were also quite good. This gives confidence to the rates and gas migration parameters, which have been captured well.

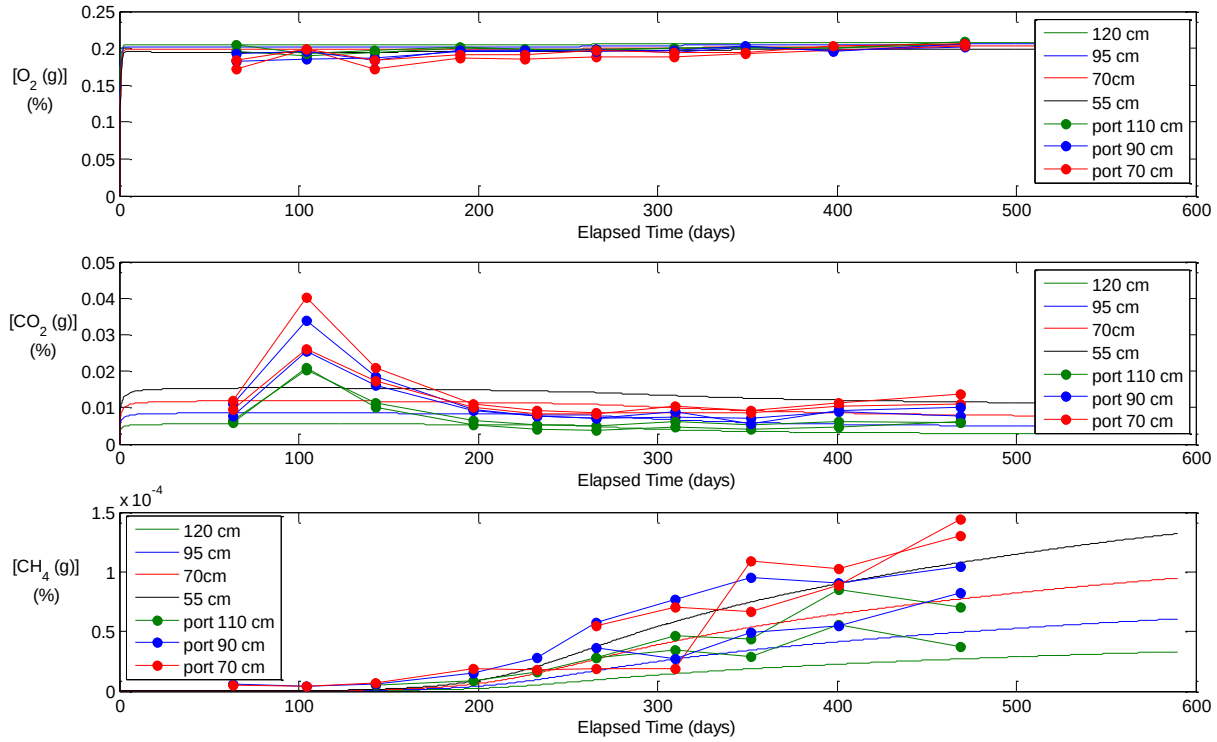

Figure 4-5: Concentrations of O_2, CO_2 and CH_4 gases for Model A

The O_2 remained relatively steady over the course of the experiment, with some noise in the experimental data, which was not reproduced. The CO_2 data shows a short term peak near the start before the first precipitation event. This peak was not considered since CO_2 production remained fairly steady for the remainder of the experiment and this was deemed to be the more important result to capture. The CH_4 production begins to increase around 150 days into the experiment, and the increase is matched fairly well by the simulated CH_4 production. In the model, the delayed onset of CH_4 generation is partially attributable to the inhibition term which accounts for delays due to microbial growth. In reality, CH_4 generation is related to acetate degradation, which was not fully captured by the model.

4.2.2 Aqueous Species

Figure 4-6 shows the pH data from the Model A simulation with the pH data from two of the sandtank ports near the center of the tank (at 30 cm and above the water table at 50 cm). Simulated pH data proved difficult to correlate with the observational sandtank data. In the model, every process affects

the pH or is affected by the pH and trends with depth were complex. Still a reasonable correlation was obtained with the port at 30 cm approximately following the trend of the simulation at 26 cm, and the simulation at 55 cm approximately following the trend of the port at 50 cm. Acidity increases above the water table and decreases in the saturated zone, as observed in the experimental data.

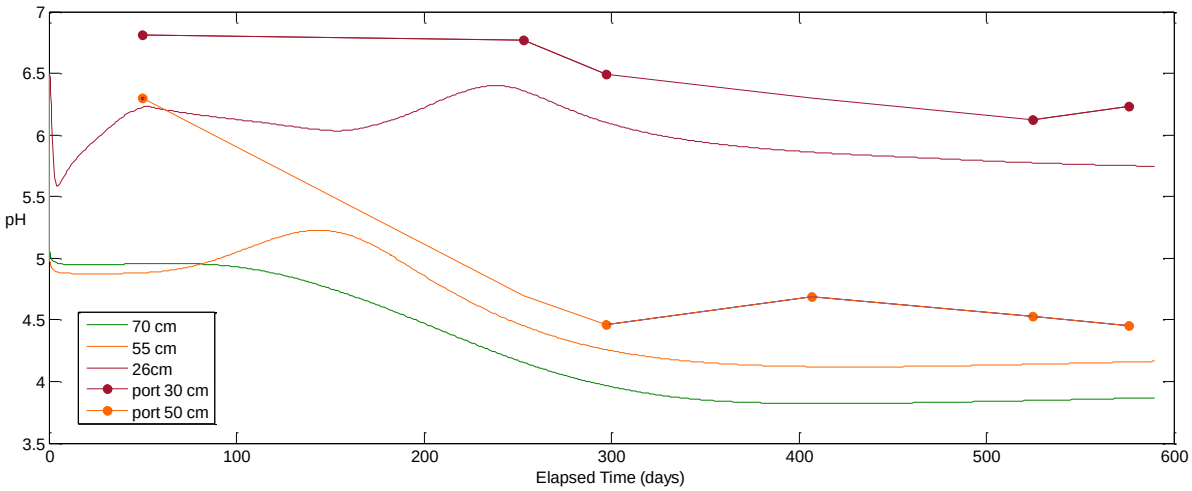

Figure 4-6: Results for simulated pH data from Model A

Figure 4-7 shows the simulated concentrations of acetate, propionate and butyrate over time in the sandtank. Again, the data provides an adequate fit to the experimental data obtained from the aqueous samples in the sandtank over time, which are plotted with the markers. Observed concentrations are reproduced within an order of magnitude.

The VFA data was significantly more stable and therefore easier to simulate. Immediately after the nutrient addition event (at 303 days into the experiment) the sandtank data showed a significant increase in VFA production in the 30 cm ports. Since the precipitation and nutrient addition events were ignored for the simulation for the sake of simplicity, it makes sense that the simulated data does not match well with the sandtank data around the 350 day mark. The rest of the data points agree well and the similarity overall provides confidence that the reaction rates are captured adequately (within an order of magnitude).

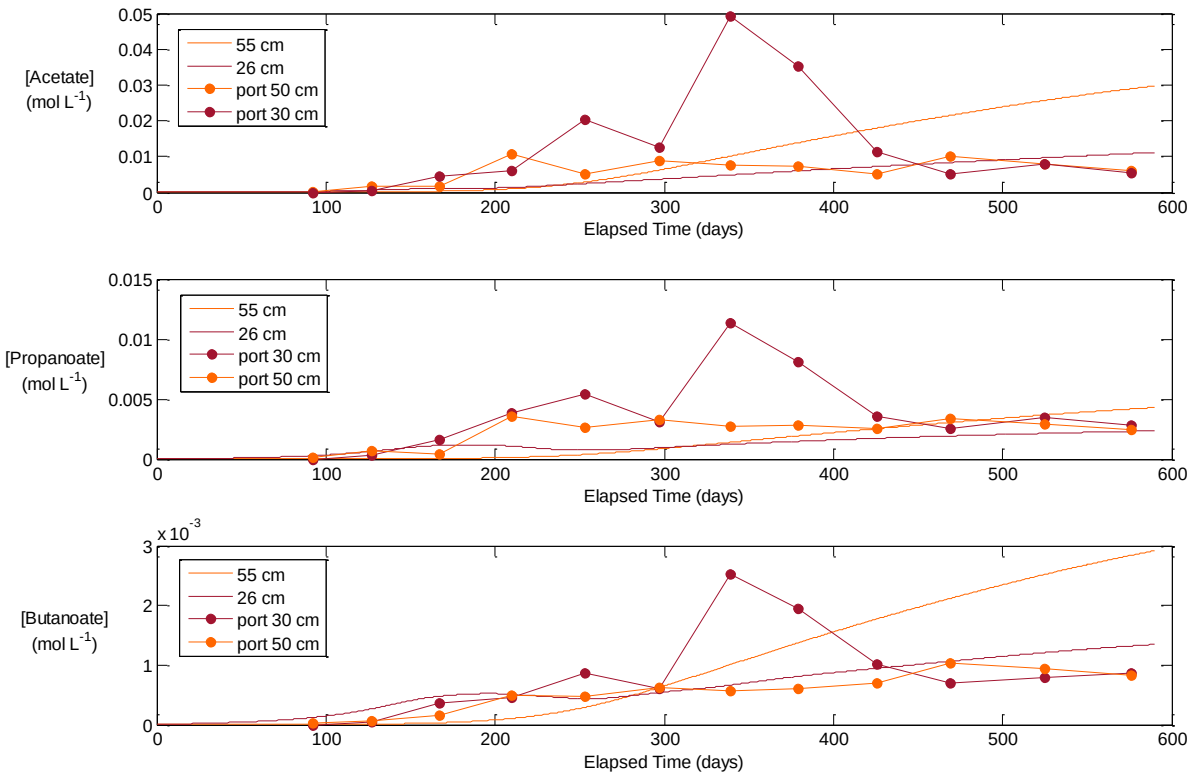

Figure 4-7: Concentrations of acetate, propionate and butyrate for Model A

Figure 4-8 shows the simulated concentrations of Fe and Mn in the sandtank at depths of 55 cm, 26 cm and 10 cm. The simulated data produces a relatively good fit to the sandtank data, which is also plotted on Figure 4-8. The simulation results were calibrated by adjusting the amount of Fe and Mn oxides present in the tank and available for reductive dissolution, as well as adjusting the rate coefficient for the reaction. It was assumed that Fe and Mn hydroxides did not become depleted over the course of the experiment.

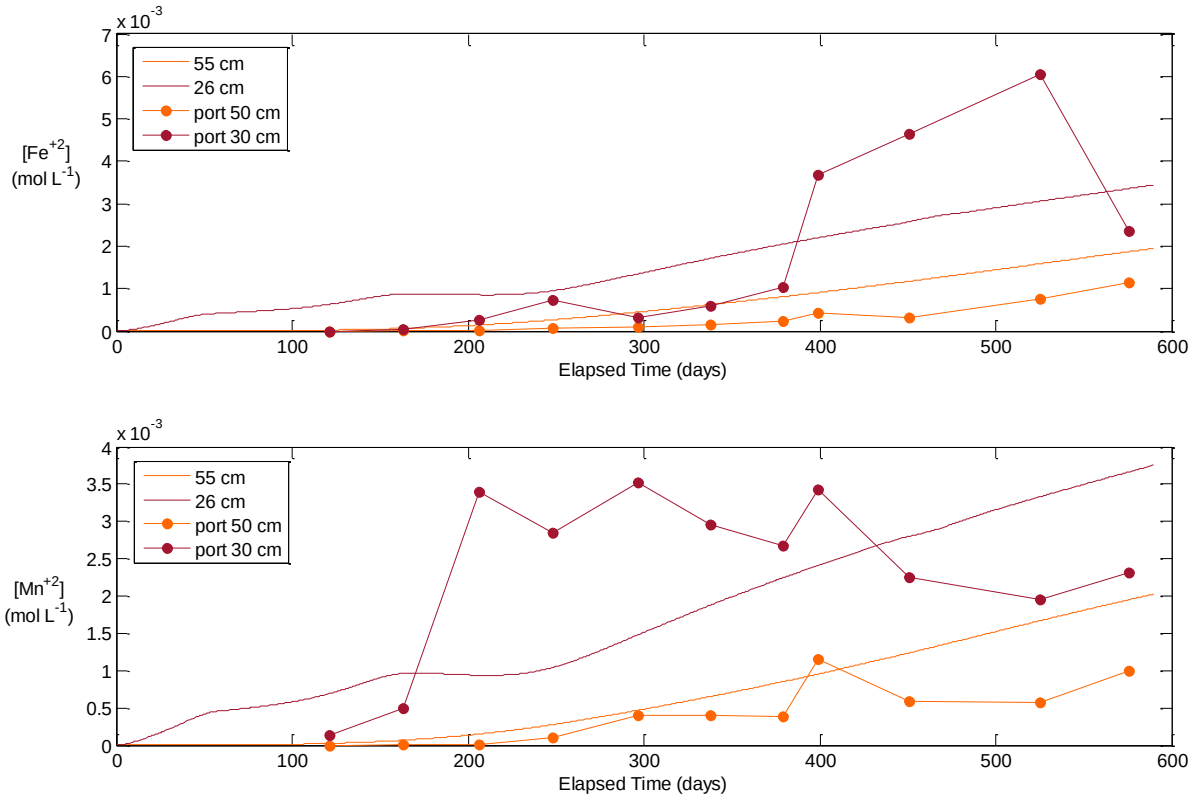

Figure 4-8: Concentrations of Fe and Mn for Model A

The Fe and Mn data obtained from the sandtank is quite erratic. Therefore, the focus of the simulation was on replicating approximately the concentration trends observed (within an order of magnitude) in order to get an idea of the rates of reductive dissolution we might expect to be occurring in the saturated zone of the sandtank. It is clear that generally, the concentrations have increased up to a point, and then began to decrease. For the purpose of this simulation, the focus was on replicating the initial increase in the concentrations in order to determine the reaction rates. Assuming that the Fe and Mn oxides are being reduced in the sandtank, it is possible that the concentrations begin to decrease after 530 days for Fe and after 400 days for Mn because the Fe and Mn oxide supply has become completely depleted in the tank. However, in the present simulation, this does not happen. An excess amount of these phases was assumed and the rate coefficient controls the progress of the reactions. If in fact the Fe and Mn oxides become depleted in the tank, more work should be done in model

calibration to attempt to better replicate this trend. However, this was beyond the scope of this preliminary study.

4.2.3 Carbon Balance

A mass balance file is generated through time for all components in a MIN3P simulation. The mass balance for CO_3^{2-} was used to determine the total mass lost as a gas efflux, which was 234 mol. This value was converted to a percent of biodiesel degraded, similarly to the calculation completed in section 3.5.1.1 where the CO_2 efflux was integrated over the surface of the sandtank to determine the percentage of biodiesel degraded. This comparison was used as a check to ensure that the simulation is representative of the results of the experiment.

Recall that in the real experiment approximately 3.7% of the biodiesel had been converted to CO_2. In Model A, approximately 5.4% of the biodiesel was effluxed as CO_2 after 590 days, which is relatively close considering the many uncertainties associated with both calculations.

4.3 Model B Results

The results of the Model B simulation, which included the dissolution of dolomite containing Fe and Mn, are described in this section. Note that this is a preliminary model which attempts to represent a complex system of chemical reactions.

4.3.1 Gaseous Species

Figure 4-9 shows the concentrations of O_2, CO_2 and CH_4 gases in Model B.

The simulated gas data looks very similar to the Model A results, and provides an adequate fit with the experimental data besides the fluctuations seen near the beginning of the experiment.

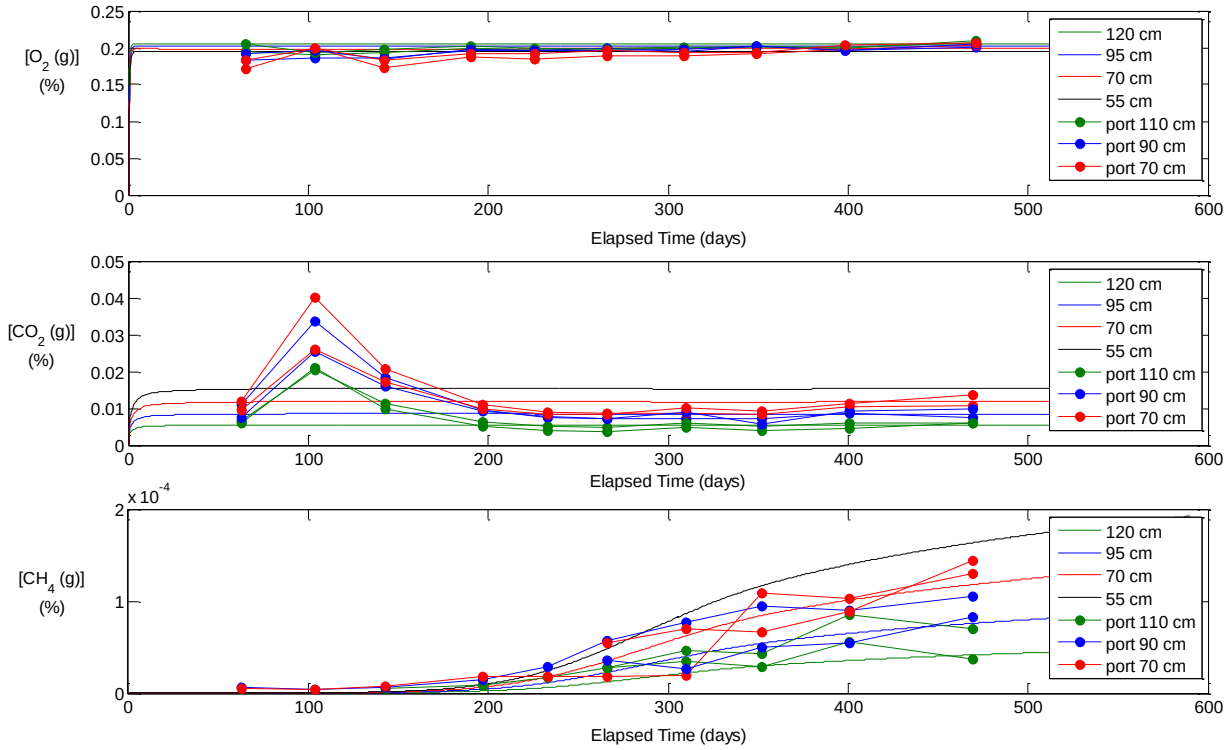

Figure 4-9: Concentrations of O_2, CO_2 and CH_4 gases for Model B

4.3.2 Aqueous Species

Figure 4-10 shows the pH results from the Model B simulation plotted alongside the experimental pH results from ports at 50 cm and 30 cm from the bottom of the tank (in the center).

The pH data increases quickly near the beginning of the experiment, as the water equilibrates with the dolomite in the system. Eventually, the acid producing reactions reach a steady state and the pH data stabilizes at circum-neutral values. The fit of the pH data at the 30 cm port (with the simulation at 26 cm) is excellent. The simulated pH at 50 cm is much higher than what was observed in the sandtank experimental data above the water table.

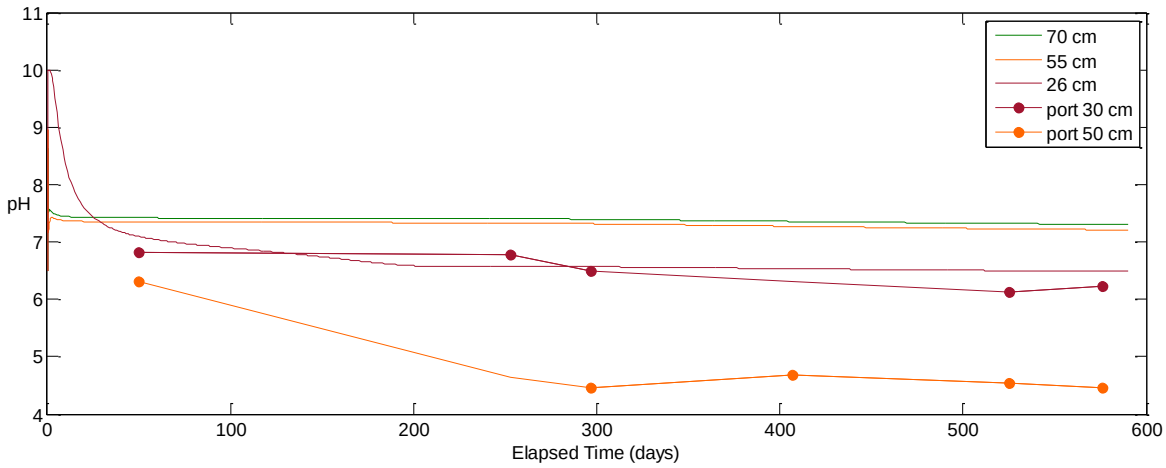

Figure 4-10: Results for simulated pH data for Model B

Figure 4-11 shows the concentrations of acetate, propionate and butyrate obtained from the Model B simulation. The simulated data is more stable than the data from Model A, and it is still within an order of magnitude of the experimental data which is a good fit for the purposes of this exercise. Some features of the experimental data, such as the spike in VFA concentrations around 350 days, were not captured in the simulation (as expected).

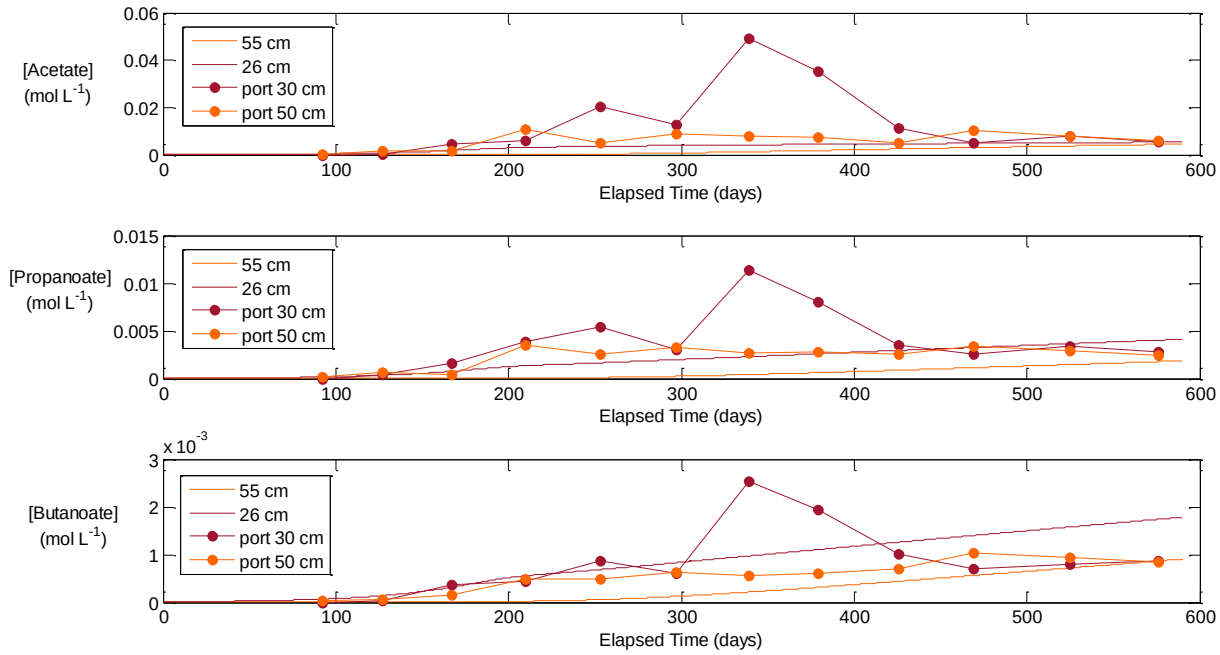

Figure 4-11: Concentrations of acetate, propionate and butyrate for Model B

Figure 4-12 shows the concentrations of Fe and Mn in the Model B simulation, plotted alongside Fe and Mn concentrations from two of the sandtank ports at relevant depths.

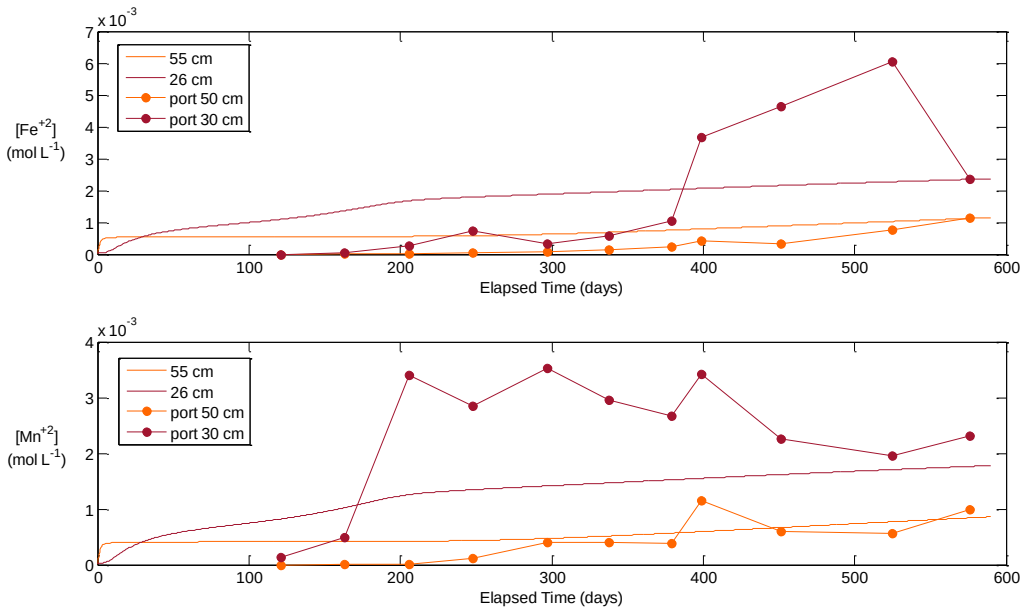

Figure 4-12: Concentrations of Fe and Mn for Model B

Concentrations of Fe and Mn increased rapidly at the beginning of the simulation relative to Model A, then appear to become stable. In Model A, concentrations of Fe and Mn were still noticeable increasing at the end of the simulation time, which is incorrect relative to the experimental data.

4.3.3 Carbon Balance

According to the mass balance file for Model B, approximately 290 moles of CO_2 had effluxed as a gas at 590 days. The initial amount of biodiesel in the simulation was 51.98 kg. This means that 6.7% of the biodiesel had effluxed as CO_2. This is slightly higher than the amount seen in the experiment (approximately 3.7%); however, it is difficult to account for all the errors introduced from approximations made in these calculations.

4.4 Model Uncertainties

Although an attempt has been made to represent the complex interactions between the most important processes occurring in the sandtank, some reactions have not been included in the models, which may affect results. For example, surface complexation has not been accounted for in the simulations. This was a fairly complex system and it is difficult to capture everything in a simulation, particularly the transient effects. Therefore, the focus of the simulations was on overall system behaviour, which was captured in general terms.

Sources of error may arise from uncertainties regarding gas phase saturations and tortuosities. However, gas phase saturations were constrained by measurements which were fairly well reproduced. The tortuosities were described by the widely accepted Millington Quirk model (Millington and Quirk, 1961). As well, the lag time created during the initial growth of the microbial populations was incorporated into the model using a relatively crude method as described in section 4.1.2.

Finally, despite the dense monitoring network used to delineate reactions in the sandtank, it is possible that small sources of error related to sampling and measuring may have impacted the rates chosen for the simulations.

It should also be noted that, although some of the simulation results agreed very well with the experimental results, it does not necessarily mean that the simulation is representing these processes perfectly; there is still uncertainty since model non-uniqueness would play a role in this experiment due to the many inter-dependent chemical reactions.

4.5 Summary and Conclusions

Overall, both preliminary models were reasonably successful at capturing the complex chemical evolution of the biodiesel degradation reactions occurring in the sandtank. Model A included the reductive dissolution of Fe and Mn oxides, balanced with siderite and rhodochrosite precipitation

reactions. This model provided a better fit with the pH data (i.e. lower pH values in the vadose zone) than Model B. Model B involved the dissolution of ankerite-dolomite to provide buffering capacity to the system. The VFA generation in this model was more reasonable, although the pH data showed higher pH values above the water table than what was observed in the experimental data. Overall, Model A is considered more adequate than Model B; with additional effort, it would be possible to refine and recalibrate Model A to better capture the VFA concentrations seen in the experiment. However, such an exercise is considered beyond the scope of the current work. The high pH values seen above the water table in Model B do not match the experimental results; the only explanation would be if the sandtank became depleted in the ankerite dolomite phase, which seems unlikely.

Both models captured gas production in the sandtank very well, and gave a reasonable approximation of the amount of biodiesel degraded in the tank after 590 days. In the experiment, it was calculated that 3.7% of the biodiesel has been effluxed as CO_2 gas. Model A estimated that 5.4% of the biodiesel was degraded, and Model B estimated that 6.7% of the biodiesel was degraded.

5 Conclusions and Recommendations

5.1 Conclusions

There are hundreds of distribution centers and thousands of service stations in Canada that could be affected by a biodiesel spill now and in the future. Many of these distribution centers are located in urban areas, with buildings and subsurface infrastructure in close vicinity, providing potential soil vapor intrusion pathways. This work aimed to evaluate whether the development of explosive conditions in basements or other underground infrastructure due to mixing of ingressing CH_4 with ambient air is a valid concern for biodiesel fuels.

A large-scale sandtank experiment was carried out to develop an understanding of the chemical, biological and physical processes and conditions that control biodiesel degradation in the subsurface, with a focus on vadose zone impacts. The tank was filled with unwashed silty sand obtained from a local source. The sandtank monitoring set up consisted of a network of ports and sensors as well as surface efflux measurements. Three hundred sampling ports were accessible from the rear of the sandtank, and a grid of sensors was emplaced to continuously measure O_2, CO_2, moisture content, and temperature. A flat water table was set at approximately 30 cm from the bottom of the 150 cm tall tank. The surface of the sandtank was open to the atmosphere and allowed oxygen ingress into the tank.

On March 17, 2015, 80 L of biodiesel was applied at the surface in the central 0.5 m^2 rectangular portion of the tank. The pure biodiesel was dyed red with Sudan IV (1 mg per 10 L of fuel) to visually trace the migration of LNAPL. The biodiesel percolated down through the sediment and spread laterally, pooling on the water table. Visible migration of biodiesel stopped after 3 days leaving behind a stagnant labile organic carbon source in the tank. In the vadose zone, biodiesel remained present at residual saturation. At the water table, the biodiesel has spread to form a pool across the length of the sandtank. Water was applied at surface on two occasions to simulate precipitation events and to avoid drying up of the tank. After 303 days, a biostimulation experiment was initiated whereby 100 L of Vancouver tap

water was amended with ammonium chloride and potassium orthophosphate and applied to the surface of the sandtank.

The gas chemistry in the sandtank was delineated via in-situ gas measurements (N_2, O_2, Ar, CO_2 and CH_4), surface gas efflux measurements for CO_2 and CH_4, and stable isotope measurements for $\delta^{13}C$ in CO_2 and $\delta^{13}C$ and $\delta^{2}H$ in CH_4. Aqueous samples were collected from the saturated zone to determine concentrations of VFAs (acetic, propionic and butyric acid), cations (Al, Ca, Fe, K, Mg, Mn, Na, and Si), and anions (Br, Cl, F, NO_2, NO_3, PO_4, and SO_4) as well as pH and alkalinity.

Finally, two models were constructed using the reactive transport code MIN3P to determine the likely source of Fe and Mn concentrations in the aqueous samples. Two scenarios were considered to explain the high concentrations of these metals: (i) the reduction of Fe and Mn oxides with pH buffering from calcite, and (ii) the dissolution of ankerite-dolomite to buffer pH in areas of acid generation.

In particular, the following conclusions from the experimental results are highlighted:

1. **CO_2 generated due to biodegradation was relatively limited.**

   Most of the CO_2 sensors stabilized between 0.5 and 2% near the end of the experiment at 590 days; maximum CO_2 concentrations observed in the tank near the beginning of the experiment were around 3%.

   The CO_2 flux initially increased to around 4.2 µmol m^{-2} s^{-1} before a rapid decrease which coincided with the first precipitation event. The CO_2 effluxes seemed to reach a quasi-steady state ranging between 0.5 and 2 µmol m^{-2} s^{-1}; values increased according to the proximity of the chamber to the spill zone.

   In this experiment, biodiesel degradation did not lead to significant CO_2 concentrations in the subsurface. This was caused by a combination of factors. Most importantly, despite the relatively large dimensions of the experiment, it remains difficult to apply the finding directly to

field sites, which are typically characterized by a much larger spatial scale and larger spill volumes. In addition, low pH conditions likely inhibited microbial growth due to a lack of carbonate minerals in the sediments.

2. **Vadose zone CH_4 concentrations and surface effluxes were small.**

   A contribution to the biodiesel degradation seems to be occurring due to methanogenesis at and below the water table; however, the vadose zone concentrations and surface efflux of CH_4 remained low. The first signs of CH_4 generation according to the Varian GC analysis began approximately 250 days into the experiment. The maximum CH_4 concentration obtained from ports within the tank was approximately 800 ppm, with most values ranging from 130 ppm to 300 ppm.

   The first signs of CH_4 effluxes began around 145 days into the experiment. By the 590 day mark, the flux seemed to have reached a steady-state ranging between 0.01 and 0.03 μmol m^{-2} s^{-1}.

   At early time, some of the CH_4 was oxidized as it diffused up through the vadose zone. At later time, acid generation may have prevented methanotrophic microbial communities from establishing themselves effectively in the sandtank. Low pH conditions resulting from biodegradation and slow microbial acclimatization - possibly affected by nutrient limitation - may have further inhibited degradation of CH_4 in the vadose zone.

3. **Soil Vapour Intrusion risks associated with biodiesel degradation may be limited.**

   Under the experimental conditions, relatively low gas effluxes occurred due to biodiesel degradation. The risk for soil vapour intrusion due to biodiesel degradation is therefore limited on the scale of the sandtank experiment. However, these results cannot be generalized to the field, due to larger scales, larger spill volumes, different soil conditions, and possibly more favorable conditions for degradation. On the other hand, the biodiesel degradation rates observed in this experiment and reported in the literature suggest that biodiesel decomposition

is not as rapid as the degradation of ethanol. The associated soil vapor intrusion risk is therefor also lower than with ethanol or ethanol –blended fuels.

4. **Acidification and precipitation events appear to have had a large impact on biodegradation rates and vadose zone gas chemistry.**

   In the unsaturated zone, slow degradation of biodiesel and CH_4 was likely caused from low pH conditions due to the acidity generated via aerobic degradation. In the saturated zone, the slow degradation was likely caused by anaerobic conditions, possibly aggravated by the presence of the infiltration water covering the biodiesel pool.

5. **The biostimulation event had a noticeable but short-term impact**

   Gas generation as well as VFA concentrations and cation concentrations increased for up to 100 days after the biostimulation event; however, all parameters returned to pre-stimulation values approximately 100 days after the nutrient addition, presumably because the nutrients had been used up.

6. **Water quality impacts are a matter of concern**

   Based on this conceptual model, biodiesel degradation caused a decline of water quality in the sandtank. Aerobic degradation of biodiesel in the vadose zone generated CO_2 and appears to have generated significant acidity based on the vertical pH profiles. Unfortunately, it was not possible to obtain aqueous samples above the 50 cm horizontal transect in the sandtank; however, this zone appears to be a mixing zone where acidity from the vadose zone moves downward and VFAs from the saturated zone migrate upward. VFA production was very high in the saturated zone, and led to the generation of acidity in the capillary fringe and below the water table. The pH of the water decreased significantly, with minimum values of 4.5 in the center of the tank at 50 cm from the base. The acidity had significant consequences related to dissolution of pH-buffering minerals in the sediments, leading to increased concentrations of

several major cations including Ca^{2+}, Mg^{2+}, Fe^{2+} and Mn^{2+}. A further decrease in pH may have mobilized larger amounts of Al^{3+}.

7. **Carbon balance estimates showed that the biodiesel was recalcitrant to biodegradation.**

   At 590 days into the experiment, it is estimated from these mass balance calculations that only 4.2% of the biodiesel had been transformed to VFAs, CO_2 or CH_4 and only 3.7% had effluxed from the tank as CO_2 or CH_4. Other sources of carbon may be present in the sandtank due to biodiesel degradation and include biomass and dissolved CO_2 (TIC); however, the overall volume of biodiesel degraded was clearly limited relative to the initial volume present in the tank. Degradation rates in the sandtank were very similar to those observed in microcosm experiments of biodiesel degradation by Zhang et al. (2013), Corseuil et al. (2011) and Lisiecki et al. (2013).

8. **Conclusions from reactive transport modeling**

   In Chapter 4, two MIN3P simulations are compared to help determine the origin of the Fe^{2+} and Mn^{2+} in the sandtank water; it was hypothesized that amorphous Fe and Mn oxides present in the tank are undergoing reductive dissolution and simultaneously provide some pH-buffer capacity, or that ankerite dissolution is buffering the pH and releasing Fe and Mn over time. In reality, there is probably some combination of these and other reactions occurring in the system. Overall, a reasonable good fit was achieved for both simulations. Model A (Fe and Mn oxide dissolution) was better able to replicate the pH trends seen with depth. Model B (dolomite dissolution) showed more stable results for aqueous parameters, including Mn, Fe and VFA concentrations. Model A predicted a total efflux of degraded biodiesel of 234 moles of CO_2 (5.4% of the biodiesel) and Model B predicted a total efflux of degraded biodiesel of 290 moles of CO_2 (6.7% of the biodiesel). Model A was better overall at capturing the complex

evolution of the system; however, Model B may have been improved by further limiting the fraction of dolomite ankerite.

The continued growth in the production and consumption of biodiesel will increase potential for accidental releases to the environment. Improved understanding of these processes and the ongoing development of advanced modeling tools will ensure that Canadian industry and regulators have access to the most current information available.

This research has helped develop methods to gauge the risk that comes with biodiesel production and usage in Canada and worldwide. In addition to method development, this work provides baseline data on the effects that biodiesel may have on soil vapor intrusion of CH_4 and had indicated that the development of explosive conditions in basements or other underground infrastructure due to mixing of ingressing CH_4 with ambient air may be of lesser concern for this emerging fuel, at least under the experimental conditions described.

5.2 Recommendations

5.2.1 Experimental Work

This experiment involved a comprehensive assessment of the system of chemical reactions involved in the biodegradation of biodiesel. However, some questions remain unanswered which may be worth revisiting in a future experiment, but which were beyond the scope of this M.Sc. thesis.

Very little of the biodiesel was degraded during this 590 days experiment; however, a longer time frame for the experiment may have allowed the microbial communities to establish themselves more effectively, and degradation rates may have eventually increased.

A scanning electron microscope (SEM) analysis and/or sequential extractions should be done in future to determine the quantity of amorphous minerals present in the sand. This value, as the ratio of

amorphous to crystalline metals (eg. iron) would help determine the rate of reduction of the substrate (Roden and Zachara, 1996).

It is hypothesized that VFA production and other anaerobic processes are occurring in the saturated zone, while aerobic degradation is occurring in the vadose zone and generating significant acidity. The capillary fringe at 50 cm appears to act as a mixing zone, where VFA concentrations have migrated upward and acidity has migrated downward. Even though soil water solution samplers were emplaced, obtaining water samples from the vadose zone was not possible during this experiment; however this data would have confirmed or refuted this hypothesis. Along the same lines, obtaining biodiesel samples during late stages of the experiment for carbon isotope analysis would have been useful to gauge the degree of biodiesel degradation in this region. However, techniques were not available to collect and process these samples.

Further work and fine-tuning of the MIN3P models may also help to provide insights into future trends for gas production in the tank.

Finally, in future experiments characterizing the degradation of biodiesel, further complexity could be included to expand the knowledge base on the impacts of this fuel. Several knowledge gaps remain. It would be beneficial to determine rates of degradation in different soil types, system evolution with induced groundwater flow, or the resulting system of reactions during a full-scale field release. This information would build on the foundational knowledge which has been established from this experiment.

Bibliography

Aelion, M.C., Hohener, P., Hunkeler, D., Aravena, R., 2009. Environmental Isotopes in Biodegradation and Bioremediation. CRC Press: 3 – 43.

Ali, A.E.M., 2011. Effect of ethanol and biodiesel addition on the movement and biodegradation of volatile petroleum hydrocarbons in the subsurface. PhD thesis at School of Civil Engineering and Geosciences, Newcastle University, pp. 109-122.

Amos, R.T., Mayer, K.U., Bekins, B.A., Delin, G.N., Williams, R.L., 2005. Use of dissolved and vapor-phase gases to investigate methanogenic degradation of petroleum hydrocarbon contamination in the subsurface. Water Resources Research 41 (2): W02001, doi:10.1029/2004WR003433.

Anderson, R.T., Rooney-Varga, J.N., Gaw, C.V., Lovley, D.R., 1998. Anaerobic benzene oxidation in the Fe(III) reduction zone of petroleum-contaminated aquifers. Environmental Science and Technology, 32 (9): 1222-1229

Apogee Instruments Inc, 2015. Owner's Manual – Oxygen Sensor Models SO-110, SO-120, SO-210 and SO-220. Apogee Instruments Inc.

Aquino, I.P., Hernandez, R.P.B., Chicoma, D.L., Pinto, H.P.F., Aoki, I.V., 2012. Influence of Light, Temperature and Metallic Ions on Biodiesel Degradation and Corrosiveness to Copper and Brass. Fuel, 102: 795-807.

Arduino AG, 2017 <https://www.arduino.cc/>. Accessed February 19th, 2017.

Baedecker, M. J., Cozzarelli, I. M., Eganhouse, R. P., Siegel, D. I., & Bennett, P. C., 1993. Crude oil in a shallow sand and gravel aquifer—III. Biogeochemical reactions and mass balance modeling in anoxic groundwater. Applied Geochemistry, 8: 569-586.

Bekins, B.A., E.M. Godsy, and E. Warren, 1999. Distribution of microbial physiologic types in an aquifer contaminated by crude oil. Microbial Ecology, 37: 263–275.

Bell, F.G., 2016. Fundamentals of Engineering Geology. Elsevier, pp. 445.

Borden, R.C., and Bedient, P.B., 1986. Transport of dissolved hydrocarbons influence by reaeration and oxygen limited biodegradation: 1. Theoretical Development, Water Resources Research, 22, 1973-1982.

Capiro, N.L., Stafford, B.P., Rixey, W.G., Bedient, P.B., Alvarez, P.J., 2007. Fuel-grade ethanol transport and impacts to groundwater in a pilot-scale aquifer tank. Water Research, 41: 656-664.

Chen, Y.D., Barker, J.F., Gui, L., 2008. A strategy for aromatic hydrocarbon bioremediation under anaerobic conditions and the impacts of ethanol: A microcosm study. Journal of Contaminant Hydrology 96: 17– 31.

Christensen, T.H., Bjerg, P.L., Banwart, S.A., Jakobsen, R., Heron, G., Albrechtsen, H.-J., 2000. Characterization of redox conditions in groundwater contaminant plumes. Journal of Contaminant Hydrology 34 (3-4): 165-241.

City of Vancouver, 2015. Vancouver Water Utility Annual 2015 Report. Available at <http://vancouver.ca/files/cov/water-quality-report.pdf>. Accessed October 13, 2016.

Clifford, H.K., Webb, S.W., 2006. Gas Transport in Porous Media, Chapter 2 (pg. 64) and Chapter 7 (pg. 124). Springer Science and Business Media.

Corseuil, H.X., A.L. Monier, M. Fernandes, M.R. Schneider,C.C. Nunes, M. DoRosario, and P.J.J. Alvarez, 2011. BTEX plume dynamics following an ethanol blend release: Geochemical footprint and thermodynamic constraints on natural attenuation. Environmental Science and Technology, 45: 3422–3429.

Davis, M.L., Cornwell D.A., 1998. Introduction to environmental engineering. WCB McGraw Hill: 216-237.

Dempster, H.S., Sherwood Lollar, B., Feenstra, S., 1997. Tracing organic contaminants in groundwater: a new methodology using compound-specific isotope analysis. Environmental Science & Technology 31 (11): 3193-3197.

Derbal, K., Bencheikh-LeHocine, M., and Meniai, A.H., (2012). Production of biogas from sludge waste and organic fraction of municipal solid waste, Biogas, Dr. Sunil Kumar (Ed.), ISBN: 978-953-51-0204-5, InTech, Available from: http://www.intechopen.com/books/biogas/production-of-biogas-from-sludge-and-organic-fraction-of-municipal-solid-waste.

Dynament Inc, 2011. Technical data sheet TDS0058, Premier Carbon Dioxide Infrared Sensor, Non-Certified Version, pp, CO2 range type MSH-P-CO2/NC. Dynament Inc.

Elsner, M., Zwank, L, Hunkeler, D., Schwarzenbach, R.P., 2005. A new concept linking observable stable isotope fractionation to transformation pathways of organic pollutants. Environmental Science and Technology 39 (18): 6896–6916

Fang, H.L., McCormick, R.L., 2006. Spectroscopic Study of Biodiesel Degradation Pathways. SAE Technical Paper 2006-01-3300, doi:10.4271/2006-01-3300.

Freitas, J.G., Fletcher, B., Aravena, R., Barker, J.F., 2010. Methane production and isotopic fingerprinting in ethanol fuel contaminated sites. Ground Water, 48: 844–857.

Gautelier, M., Oelkers, E.H., Schott, J., 1999. An experimental study of dolomite dissolution rates as a function of pH from -0.5 to 5 and temperature from 25 to 80^{o}C. Chemical Geology 157: 13-26.

Harrington, R.R., Poulson, S.R., Drever, J.I., Colberg, P.J.S., Kelly, E.F., 1999. Carbon isotope systematics of monoaromatic hydrocarbons: vaporization and adsorption experiments. Organic Geochemistry 30 (8): 765-775.

Hatch, T. 2011. Biodiesel relative risk: a qualitative approach to determining the environmental fate of animal fat and soy biodiesels through a direct experimental comparison with Ultra Low Sulfur Diesel and screening model simulations using hydrocarbon spill screening model. PhD thesis at School of Civil Engineering, University of California Davis.

Hill, J., Nelson, E., Tilman, D., Polasky, S., Tiffany, D., 2006. Environmental, economic and energetic costs and benefits of biodiesel and ethanol biofuels. Proceedings of National Academy of Sciences of the USA, 103: 11206-11210.

Hodam, R., 2008. Biodiesel: a technical report. Presentation for UST Leak Prevention Unit, State Water Resources Control Board.

Hoefs, J., 1997. Stable Isotope Geochemistry, Springer Verlag, Berlin.

Hunkeler, D., Aravena, R., 2000. Determination of compound-specific carbon isotope ratios of chlorinated methanes, ethanes, and ethenes in aqueous samples. Environmental Science and Technology, 34 (13): 2839-2844.

Hunkeler, D., Chollet, N., Pittet, X., Aravena, R., Cherry, J.A., Parker, B.L., 2001. Effect of source variability and transport processes on carbon isotope ratios of TCE and PCE in two sandy aquifers. Journal of Contaminant Hydrology 74 (1-4): 265-282.

Jewell, K. P., Wilson, J. T., 2011. A new screening method for methane in soil gas using existing groundwater monitoring wells. Groundwater Monitoring and Remediation, 31: 82–94.

Jourabchi, P., Hers, I., Mayer, K.U, DeVaull, G., Bauman, B. (2013), Numerical modeling study of the influence of methane generation from ethanol-gasoline blends on vapor intrusion. National Tanks Conference and Expo, Denver, Colorado, USA.

Klassen, M., 2015. Mineralogical characterization of sediments for monitored natural attenuation experiments. Undergraduate Honor's Thesis, Dept of Earth, Ocean and Atmospheric Sciences, The University of British Columbia, pp. 6 - 20

Labjack Corporation, 2015, <https://labjack.com/about>. Accessed February 19th, 2017.

Leung, D.Y.C., Koo, B.C.P., Guo, Y., 2006. Degradation of biodiesel under different storage conditions. Bioresource Technology, 97: 250-256.

Lisiecki, P., Chraznowski, L., Szulc, A, Lawniczak, L., Bialas, W., Dziadas, M., Owsianiak, M., Stanieskiw, J., Cyplik, P., Marcik, R., Jelen, H., Heipieper, H.J., 2013. Biodegradation of diesel/biodiesel blends in saturated sand microcosms. Fuel 116: 321-327.

Lower Mainland Biodiesel – about the process, 2012. <http://www.lowermainlandbiodiesel.com/about/the-process>. Accessed May 5th, 2015

Lower, S.K., 1999. Carbonate equilibria in natural waters. Environmental Chemistry pp. 11-13.

Ma, J., Rixey, W.G., DeVaull, G.E., Stafford, B.P., Alvarez, P.J.J., 2012. Methane bioattenuation and implications for explosion risk reduction along the groundwater to soil surface pathway above a plume of dissolved ethanol. Environmental Science and Technology, 46: 6013–6019.

Ma, J., He, J., Qi, S., Gaofeng, Z., Zhao, W., Edmunds, W.M., Zhao, Y., 10`2. Groundwater recharge and evolution in the Dunhuang basin, northwestern China. Applied Geochemistry 28: 19-31. DOI: 10.1016/j.apgeochem.2012.10.007.

Mancini, S.A., Ulrich, A.C., Lacrampe-Couloume, G., Sleep, B., Edwards, E.A., Sherwood Lollar, B.S., 2003. Carbon and hydrogen isotopic fractionation during anaerobic biodegradation of benzene. Applied and Environmental Microbiology (69): 191-198.

Mata-Alvarez, J., 2003. Biomethanization of the organic fraction of municipal solid wastes. IWA Publishing: 1-18.

Mayer, K.U., Benner, S.G., Frind, E.O., Thornton, S.F., Lerner, D.N., 2001. Reactive transport modeling of processes controlling the distribution of phenolic compounds in a deep sandstone aquifer. Journal of Contaminant Hydrology, 53: 341-368.

Mayer, K.U., Frind, E.O., Blowes, D.W., 2002. Multicomponent reactive transport modeling in variably saturated porous media using a generalized formulation for kinetically controlled reactions. Water Resources Research 38: 13-1 – 13-21.

Mayer, K.U., and MacQuarrie, K.T.B., 2010. Solution of MoMaS reactive transport benchmark with MIN3P-model formulation and simulation results. Computational Geosciences. 14: 405. doi:10.1007/s10596-009-9158-6.

Meckenstock, R.zu., Morasch, B., Griebler, C., Richnow, H.H., 2004. Stable isotope fractionation analysis as a tool to monitor biodegradation in contaminated aquifers. Journal of Contaminant Hydrology 75 (3-4): 215-255.

Meher, L.C., Vidya Sagar, D., Naik, S.N., 2006. Technical aspects of biodiesel production by transesterification – a review. Renewable and Sustainable Energy Reviews, 10: 248-268.

Miller, N.J., Mudge, S.M., 1997. The Effect of Biodiesel on the Rate of Removal and Weathering Characteristics of Crude Oil within Artificial Sand Columns. Spill Science and Technology Bulletin, 4: 17-33.

Millington, R.J. and Quirk, J.P., 1961. Permeability of porous solids. Transactions of the Faraday Society 57: 1200-1207. doi: 10.1039/TF9615701200

Molins, S., Mayer, K.U., 2007. Coupling between geochemical reactions and multicomponent gas and solute transport in unsaturated media: A reactive transport modeling study. Water Resources Research 43: W05435, doi: 10.1029/2006WR005206.

Molins, S., Mayer, K.U., Amos, R.T., Bekins, B.A., 2010. Vadose zone attenuation of organic compounds at a crude oil spill site - Interactions between biogeochemical reactions and multicomponent gas transport. Journal of Contaminant Hydrology 112: 15-29.

Mueller, D.K., Hamilton, P.A., Helsel, D.R., Hitt, K.J., Ruddy, B.C., 1995, Nutrients in ground water and surface water of the United States--An analysis of data through 1992: U.S. Geological Survey Water-Resources Investigations Report 95-4031, pp. 74.

Ostrem, K., Themelis, N.J., 2004. Greening waste: anaerobic digestion for treating the organic fraction of municipal solid wastes. M.S. Thesis, Earth Engineering Center, Columbia University. Available at http://www.seas.columbia.edu/earth/wtert/sofos/Ostrem_Thesis_Final.pdf.

Pasqualino, J.C., Montane, D., Salvado, J., 2006. Synergic effects of biodiesel in the biodegradability of fossil-derived fuels. Biomass and Bioenergy, 30: 874-879.

Pidwirny, M. (2006). "Atmospheric composition". Fundamentals of Physical Geography, 2nd Edition. Accessed Jan 5, 2017. http://www.physicalgeography.net/fundamentals/7a.html

Ramos, D.T., da Silva, M.L.B., Chiaranda, H.S., Alvarez, P.J.J., Corseuil, H.X., 2013. Biostimulation of anaerobic BTEX biodegradation under fermentative methanogenic conditions at source-zone groundwater contaminated with a biodiesel blend (B20). Biodegradation, 24: 333-341.

Roden, E. E., Zachara, J. M., 1996. "Microbial reduction of crystalline iron (III) oxides: Influence of oxide surface area and potential for cell growth." Environmental Science & Technology 30: 1618-1628.

Sanford, S.D., White, J.M., Shah, P.S., Wee, C., Valverde, M.A., Meier, G.R., 2009. Feedstock and Biodiesel Characteristics Report. Renewable Energy Group, Inc., <www.regfuel.com>. Accessed April 24th, 2015.

Shah, R., Mahajan, D., Patel, S., Ball, J., Colantuoni, V., Maraj, R., 2009. Oxidation Stability in Biodiesel: A Brief Review of Current Technology. Biodiesel Magazine.

Sihota, N.J., and Mayer, K.U., 2012. Characterizing vadose zone hydrocarbon biodegradation using carbon dioxide effluxes, isotopes and reactive transport modeling. Vadose Zone Journal 11 (4) doi:10.2136/vzj2011.0204.

Sihota, N.J., Mayer, K.U., Toso, M.A., Atwater, J.F., 2013. Methane emissions and contaminant degradations rates at sites affected by accidental releases of denatured fuel-grade ethanol. Journal of Contaminant Hydrogeology 151: 1-15.

Sihota N.J., O. Singurindy, K.U. Mayer, 2011. CO2 efflux measurements for evaluating source zone natural attenuation rates in a petroleum hydrocarbon contaminated aquifer. Environmental Science and Technology, 45: 482-488.

Statista <http://www.statista.com/statistics/485400/total-biodiesel-production/> Accessed September 9th, 2016.

Stumm, W. and Morgan, J. J. (1981) Aquatic Chemistry, 2nd edition. J. Wiley and Sons, New York, pp. 780.

Suflita, J.M. and Mormile, M.R. 1993. Anaerobic biodegradation of known and potential gasoline oxygenates in the terrestrial subsurface. Environmental Science and Technology 27 (6): 976.

Thorstenson D.C. and Pollock D. W. (1989) Gas transport in unsaturated zones: Multicomponent systems and the adequacy of Fick's Laws, Water Resources Research 25 (3): 477-507.

Tyson K. 2001 Biodiesel – Handling and Use Guidelines. National Resource Energy Laboratory US Department of Energy, Golden, CO, USA.

U.S. Geological Survey, 1999. The quality of our nation's waters – nutrients and pesticides. U.S. Geological Survey Circular 1225, pp. 82.

Van Ginkel, S., Sung, S.W., Lay, J.J., 2001. Biohydrogen production as a function of pH and substrate concentration. Environmental Science & Technology 35 (24): 4726-4730.

Verma, S., 2002: Anaerobic Digestion Of Biodegradable Organics In Municipal Solid Wastes. Department of Earth & Environmental Engineering (Henry Krumb School of Mines) Fu Foundation School of Engineering & Applied Science Columbia University

Whiticar, M.J., 1999. Carbon and hydrogen isotope systematics of bacterial formation and oxidation of methane. Chemical Geology 161 (1-3): 291-314.

Yu, J., Xie, Z., Sun, L., Kang, H., He, P., Xing, G., 2015. δ^{13}C-CH4 reveals CH4 variations over oceans from mid-latitudes to the Arctic. Scientific Reports 5, 13760; doi:10.1038/srep13760.

Zhang, X., Peterson, C., Reece, D., Haws, R., Moller, G., 1998. Biodegradability of biodiesel in the aquatic environment. American Society of Agricultural Engineers 41(5): 1423-1430.

Appendices

A Appendix A

Appendix A includes all supplementary materials from Chapter 2 – Materials and Methods.

A.1 Arduino Code

The following code is the input for Arduino 1. The input files for Arduino 2 and 3 are not shown and are essentially the same.

```
#define RELAY_ON LOW //0
#define RELAY_OFF HIGH //1
#define Relay_1  2  // Arduino Digital I/O pin number
#define Relay_2  3
#define Relay_3  4
#define Relay_4  5
#define Relay_5  6
#define Relay_6  7
#define Relay_7  8
#define Relay_8  9
#define Relay_9  10
#define Relay_10  11
#define Relay_11  12
#define Relay_12  13

// ON IS OFF AND OFF IS ON FOR THE SAND TANK RELAYS

void setup()   /****** SETUP: RUNS ONCE ******/
{
//-------( Initialize Pins so relays are inactive at reset)----
  digitalWrite(Relay_1, RELAY_OFF);
  digitalWrite(Relay_2, RELAY_OFF);
  digitalWrite(Relay_3, RELAY_OFF);
  digitalWrite(Relay_4, RELAY_OFF);
  digitalWrite(Relay_5, RELAY_OFF);
  digitalWrite(Relay_6, RELAY_OFF);
  digitalWrite(Relay_7, RELAY_OFF);
  digitalWrite(Relay_8, RELAY_OFF);
  digitalWrite(Relay_9, RELAY_OFF);
  digitalWrite(Relay_10, RELAY_OFF);
  digitalWrite(Relay_11, RELAY_OFF);
  digitalWrite(Relay_12, RELAY_OFF);

//---( THEN set pins as outputs )----
  pinMode(Relay_1, OUTPUT);
  pinMode(Relay_2, OUTPUT);
  pinMode(Relay_3, OUTPUT);
  pinMode(Relay_4, OUTPUT);
  pinMode(Relay_5, OUTPUT);
  pinMode(Relay_6, OUTPUT);
  pinMode(Relay_7, OUTPUT);
```

```
  pinMode(Relay_8, OUTPUT);
  pinMode(Relay_9, OUTPUT);
  pinMode(Relay_10, OUTPUT);
  pinMode(Relay_11, OUTPUT);
  pinMode(Relay_12, OUTPUT);
  delay(4000); //Check that all relays are inactive at Reset

}//--(end setup )---

void loop()   /****** LOOP: RUNS CONSTANTLY ******/
{
//---( Turn all 4 relays ON in sequence)---
  digitalWrite(Relay_1, RELAY_ON);// set the Relay ON
  delay(500);            // wait for a second
  digitalWrite(Relay_2, RELAY_ON);// set the Relay ON
  delay(500);            // wait for a second
  digitalWrite(Relay_3, RELAY_ON);// set the Relay ON
  delay(500);            // wait for a second
  digitalWrite(Relay_4, RELAY_ON);// set the Relay ON
  delay(500);            // wait for a second
  digitalWrite(Relay_5, RELAY_ON);// set the Relay ON
  delay(500);            // wait for a second
  digitalWrite(Relay_6, RELAY_ON);// set the Relay ON
  delay(500);            // wait for a second
  digitalWrite(Relay_7, RELAY_ON);// set the Relay ON
  delay(500);            // wait for a second
  digitalWrite(Relay_8, RELAY_ON);// set the Relay ON
  delay(500);            // wait for a second
  digitalWrite(Relay_9, RELAY_ON);// set the Relay ON
  delay(500);            // wait for a second
  digitalWrite(Relay_10, RELAY_ON);// set the Relay ON
  delay(500);            // wait for a second
  digitalWrite(Relay_11, RELAY_ON);// set the Relay ON
  delay(500);            // wait for a second
  digitalWrite(Relay_12, RELAY_ON);// set the Relay ON
  delay(30000);            // wait see all relays ON

//---( Turn all 4 relays OFF in sequence)---
  digitalWrite(Relay_1, RELAY_OFF);// set the Relay OFF
  delay(500);            // wait for a second
  digitalWrite(Relay_2, RELAY_OFF);// set the Relay OFF
  delay(500);            // wait for a second
  digitalWrite(Relay_3, RELAY_OFF);// set the Relay OFF
  delay(500);            // wait for a second
  digitalWrite(Relay_4, RELAY_OFF);// set the Relay OFF
  delay(500);            // wait for a second
  digitalWrite(Relay_5, RELAY_OFF);// set the Relay OFF
  delay(500);            // wait for a second
  digitalWrite(Relay_6, RELAY_OFF);// set the Relay OFF
  delay(500);            // wait for a second
  digitalWrite(Relay_7, RELAY_OFF);// set the Relay OFF
  delay(500);            // wait for a second
  digitalWrite(Relay_8, RELAY_OFF);// set the Relay OFF
```

```
  delay(500);             // wait for a second
  digitalWrite(Relay_9, RELAY_OFF);// set the Relay OFF
  delay(500);             // wait for a second
  digitalWrite(Relay_10, RELAY_OFF);// set the Relay OFF
  delay(500);             // wait for a second
  digitalWrite(Relay_11, RELAY_OFF);// set the Relay OFF
  delay(500);             // wait for a second
  digitalWrite(Relay_12, RELAY_OFF);// set the Relay OFF
  delay(120000);              // wait see all relays OFF

}//--(end main loop )---

//*********( THE END )***********
```

A.2 Water Infiltration Test

The results of the water infiltration test performed on March 10th, 2015 (7 days before the biodiesel infiltration event) are shown in the Figure A-1 to Figure A-5. 100 L of Vancouver tap water amended with Nutrafin ™ were applied to the surface of the sandtank over 4 hours. The response of the GS3 sensors, which measure volumetric water content, can be seen for each depth. Each figure represents a vertical transect at the location in the sandtank shown in the figure title.

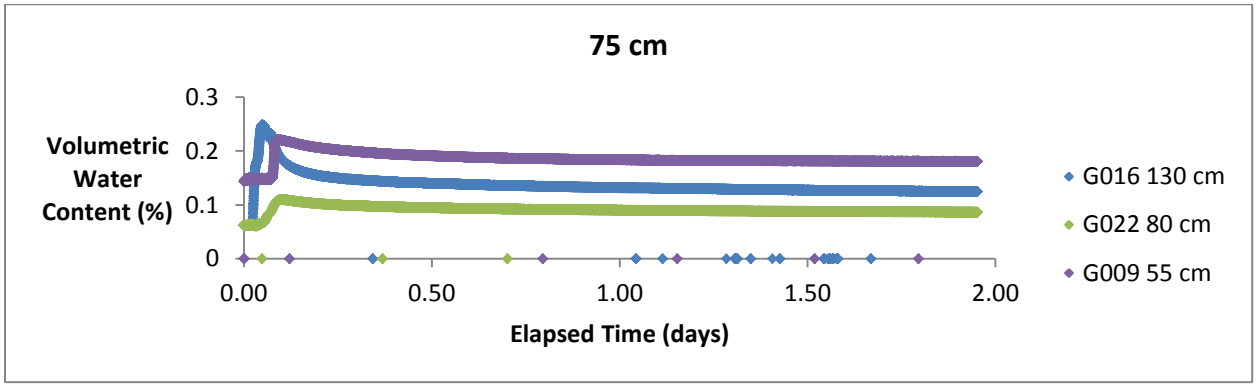

Figure A-1: VWC GS3 sensor response to 100 L infiltration test (x = 75 cm)

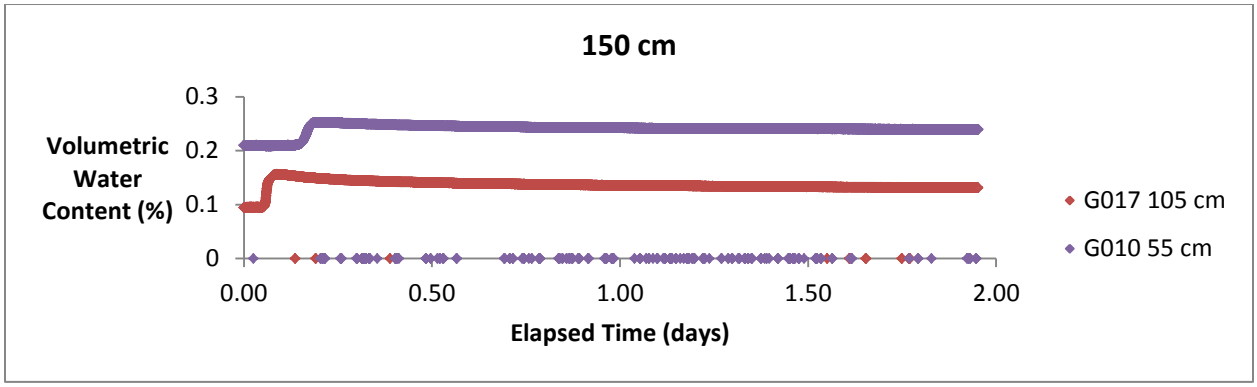

Figure A-2: VWC GS3 sensor response to 100 L infiltration test (x = 150 cm)

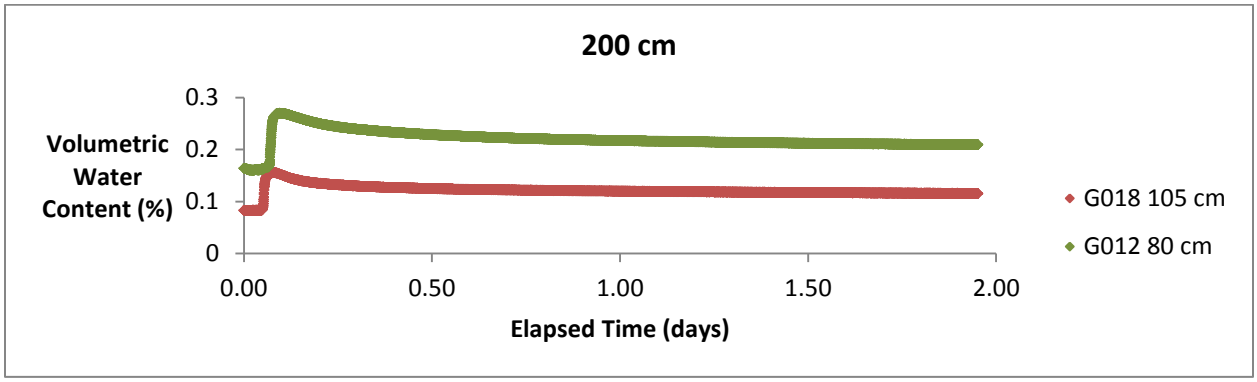

Figure A-3: VWC GS3 sensor response to 100 L infiltration test (x = 200 cm)

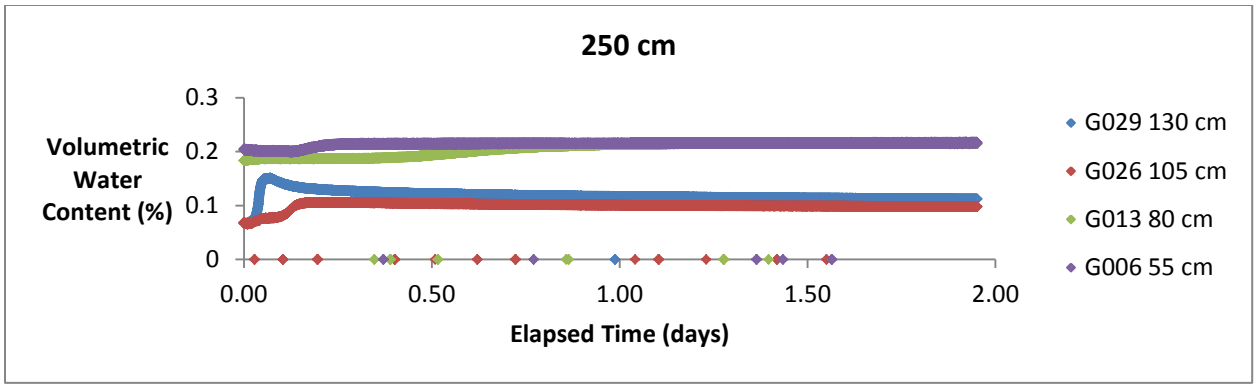

Figure A-4: VWC GS3 sensor response to 100 L infiltration test (x = 250 cm)

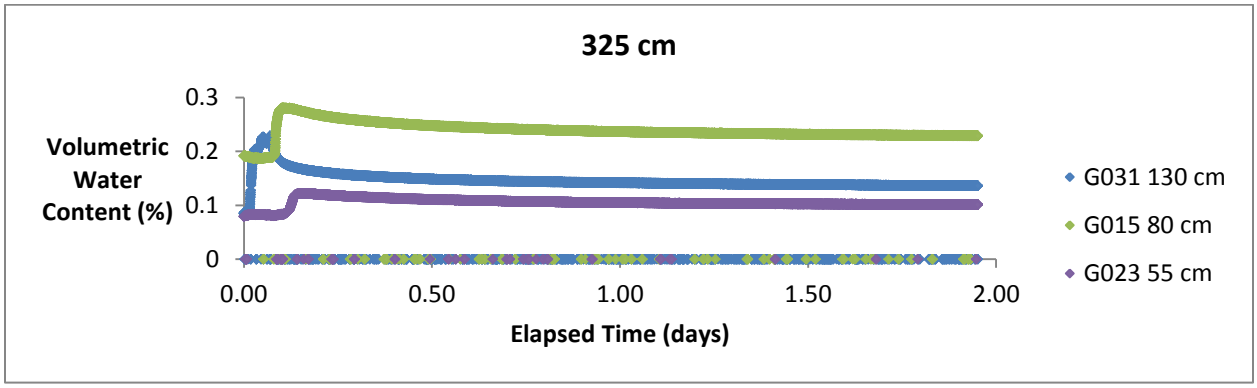

Figure A-5: VWC GS3 sensor response to 100 L infiltration test (x = 325 cm)

A.3 CO_2 and O_2 sensor responses

The Dynament CO_2 sensors and the Apogee O_2 sensor responses to the site specific injection test are shown in Table A-1 and Table A-2, respectively. The test was performed on March 2nd, 2015. CO_2 was injected at 3.5% for sensors with a range from 0-5% and 0-10%, and 14.9% for sensors with a range between 0-20% and 0-30% CO_2. Pure O_2 (100%) was injected for all sensors for the O_2 test. Injection was at 10 psi for 20 minutes.

Table A-1: Dynament CO_2 sensor responses to calibration tests

CO_2 Sensor	(x)	(z)	Port (x)	Port (z)	Start	End	0	3.05	Comments	m	b
CO2 17	75	130	60	130	14:18	14:38	0.037	0.038	Poor response		
CO2 18	150	130	140	130	14:19	14:39	0.143	1.028		3.45	-0.50
CO2 01	150	105	140	105	14:21	14:41	0.004	0.151		20.74	-0.09
CO2 13	150	80	140	80	14:38	14:59	0.004	Unresponsive			
CO2 05	150	55	140	55	14:39	14:59	0.020	0.302	Sig. drop before test	10.81	-0.22
CO2 31	200	130	180	130	14:59	15:19	0.004	Unresponsive			
CO2 06	200	105	180	105	14:59	15:19	0.006	0.290	Sig. drop before test	10.72	-0.06
CO2 14	200	80	180	80	15:00	15:20	0.004	Unresponsive			
CO2 08	200	55	180	55	15:20	15:40	0.007	0.298		10.48	-0.08
CO2 20	250	130	260	130	15:20	15:40	0.004	Unresponsive			
CO2 07	250	105	260	105	15:20	15:40	0.007	0.261		11.97	-0.08
CO2 15	250	80	260	80	15:42	16:02	0.004	Unresponsive			
CO2 04	250	55	260	55	15:42	16:02	0.006	0.128		24.94	-0.16
CO2 21	325	130	340	130	15:42	16:02	0.004	Unresponsive			

Table A-2: Apogee O2 sensor responses to calibration tests

O_2 Sensor	(x)	(z)	Port (x)	Port (z)	Start	End	0	10.05	Comments	m	b
OXY 03	75	130	60	130	14:18	14:38	0.647	0.645	Unsure, poor response		
OXY 07	150	130	140	130	14:19	14:39	0.442	0.655		47.24	-20.89
OXY 12	150	105	140	105	14:21	14:41	0.452	0.672	Sig. drop right before test	45.69	-20.68
OXY 21	150	80	140	80	14:38	14:59	0.427	0.654	Sig. drop right before test	44.35	-18.95
OXY 06	150	55	140	55	14:39	14:59	0.428	0.424	delayed response		
OXY 08	200	130	180	130	14:59	15:19	0.516	0.515	Poor response		
OXY 13	200	105	180	105	14:59	15:19	0.425	0.644		45.82	-19.47
OXY 22	200	80	180	80	15:00	15:20	0.430	0.675		41.11	-17.70
O2 07	200	55	180	55	15:20	15:40	0.421	0.632		47.64	-20.05
OXY 18	250	130	260	130	15:20	15:40	0.521	0.521	Poor response		
OXY 14	250	105	260	105	15:20	15:40	0.424	0.656		43.31	-18.38
OXY 15	250	80	260	80	15:42	16:02	0.438	0.630		52.16	-22.82
O2 09	250	55	260	55	15:42	16:02	0.670	0.617	Poor response		
02 06	325	130	340	130	15:42	16:02		0.668	Didn't reach 0 O_2		

A.4 Labjack Code

Figure A-6 and Figure A-7 show the Labview codes for Labjack 1 (offset interface and block diagram, respectively). The codes for Labjacks 2 and 3 are essentially the same, with slightly different offsets; therefore only the code for Labjack 1 has been included.

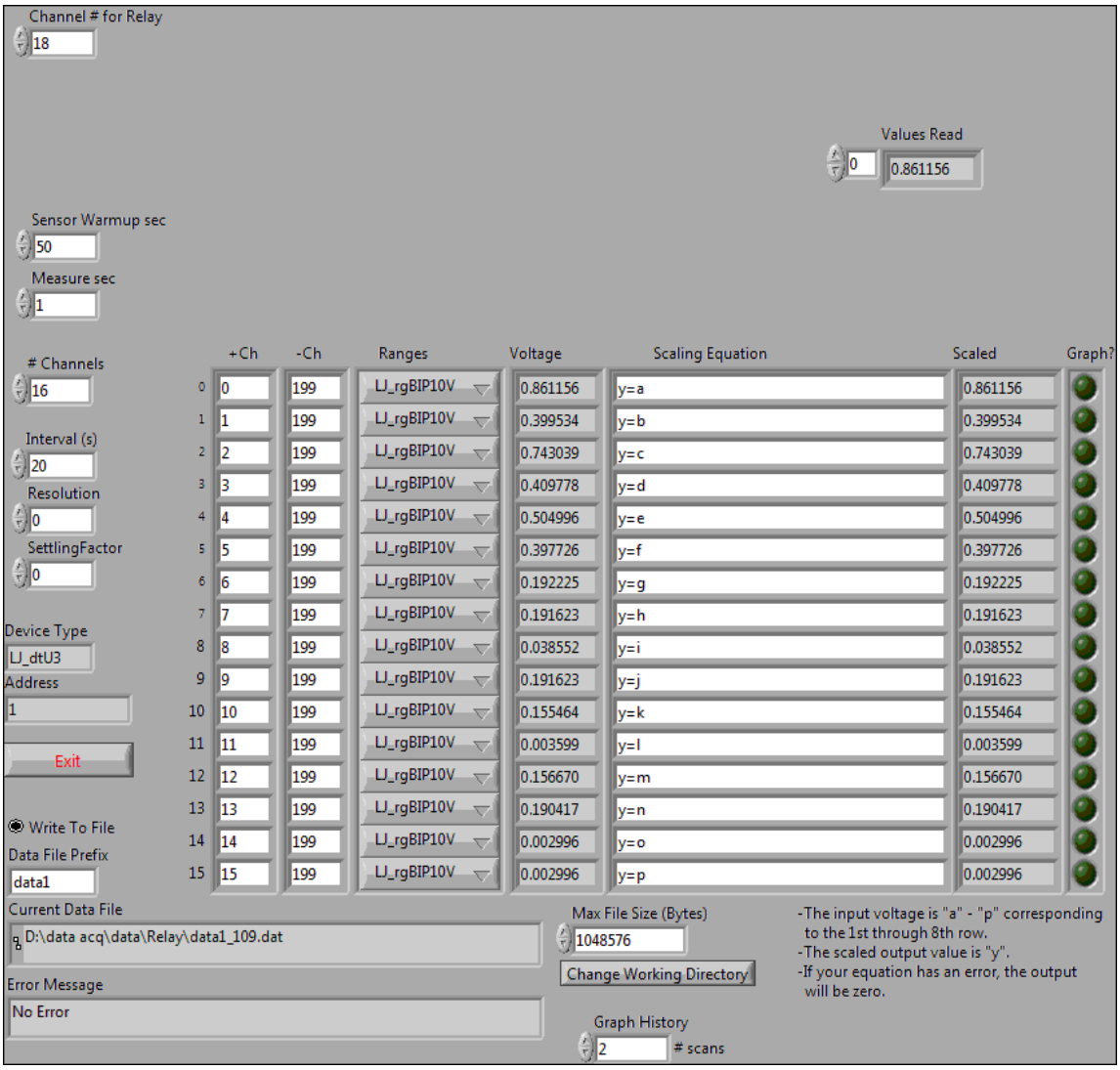

Figure A-6: Labjack 1 interface for labview code

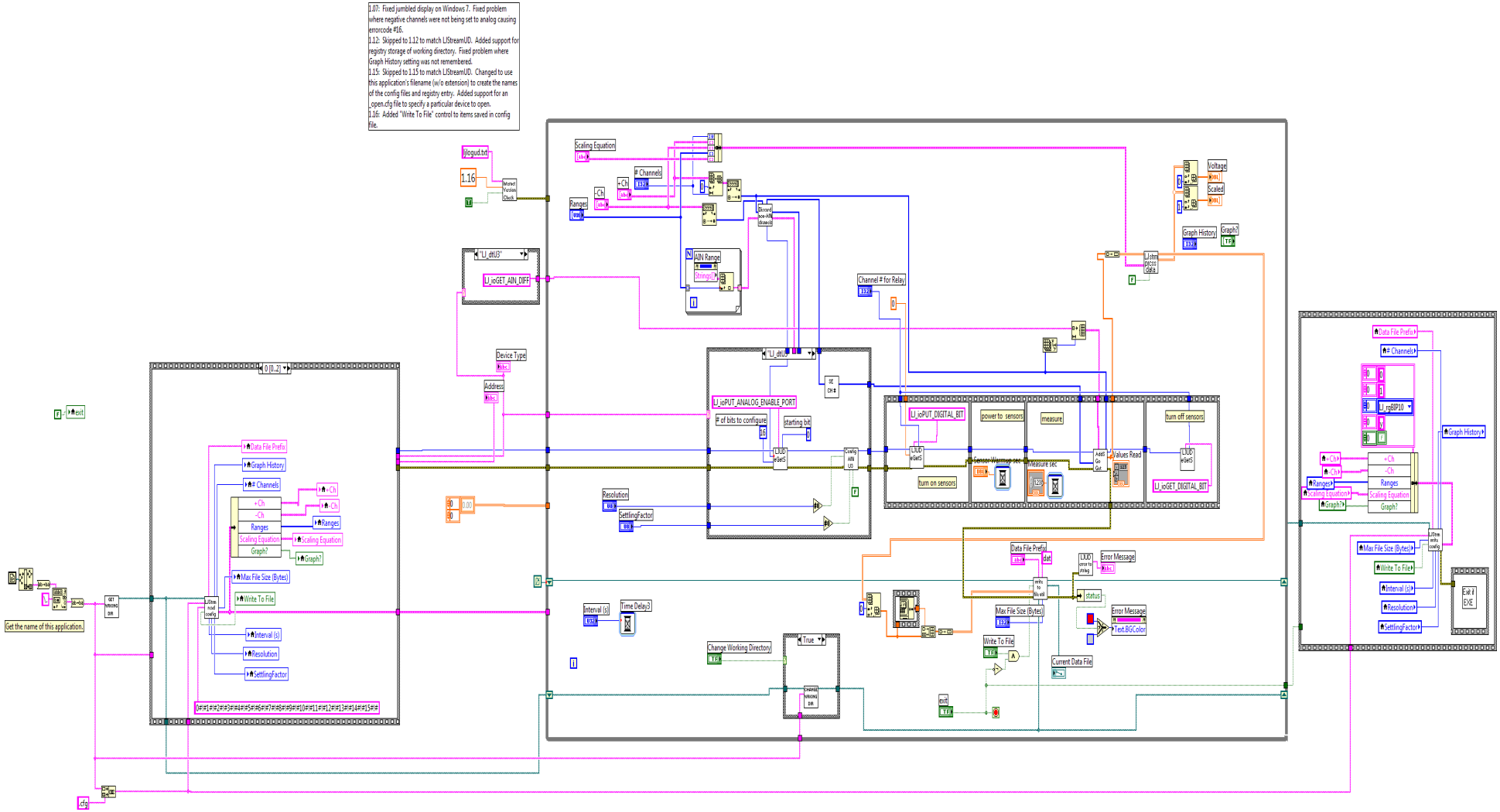

Figure A-7: Labview block diagram for Labjack

A.5 Flux Chamber (Licor and LGR) set up

The set up for the LI-COR and LGR gas analyzers is shown in Figure A-8. The two instruments require different flow rates; therefore a jumper line was inserted to account for the difference in pumping rates.

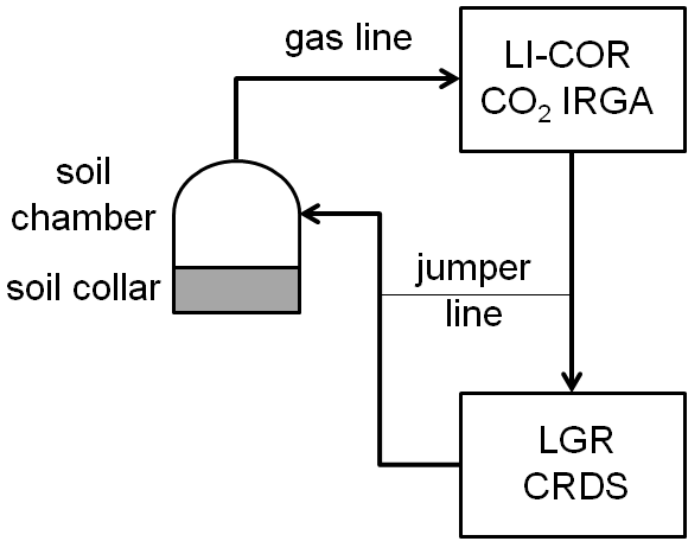

Figure A-8: LICOR and LGR set up (Figure from Sihota et al., 2013)

A.6 LGR Raw Data

Figure A-9 shows a sample of the LGR data. The slope of each peak is used to calculate the CH_4 efflux.

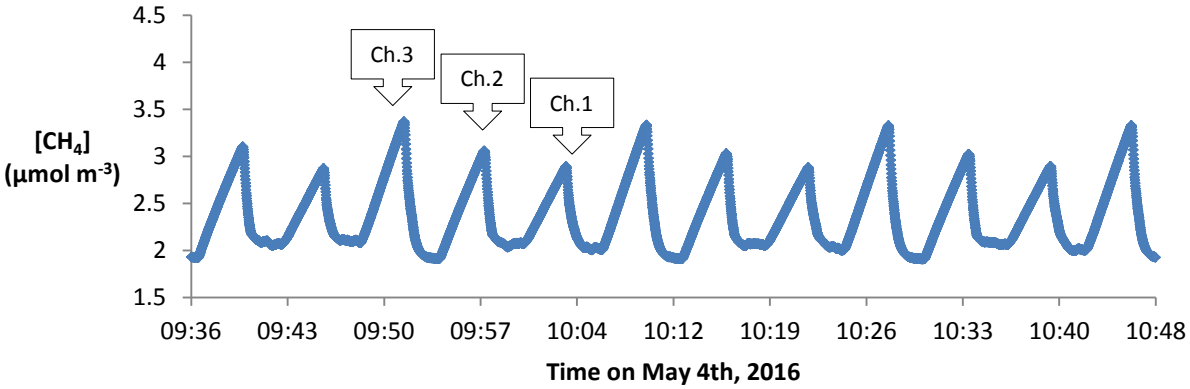

Figure A-9: LGR raw data

Recall that the formula used for this calculation is:

$$F = \frac{10VP_0\left(1-\frac{W_0}{1000}\right)}{RA(T_0+273.15)}\frac{\partial C}{\partial t}$$

where F is the gas efflux [µmol m^{-2} s^{-1}], W_0 is the initial water vapour mole fraction [µmol mol^{-1}], T_0 is the initial air temperature [°C], V is the total volume of the system (chamber, analyzers, tubing and the soil collar) [cm^3], P_0 is the initial pressure [kPa], A is the soil surface area [cm^2], R is the gas constant (8.314 [Pa m^3 K^{-1} mol^{-1}], and ∂C/∂t is the change in the dry air concentration of the gas species of interest (i.e. corrected for the water vapour flux) within the chamber headspace over the measurement period [µmol mol^{-1} s^{-1} or ppm_v s^{-1} of CO_2 or CH_4].

In this case, the efflux from chamber 3 can be calculated using the following variables:

T_0 = 25 (assumed)

W_0 = 1 (assumed)

R = 8.314 (known)

P_0 = 100.6591 (instrument measurement)

A = 217 cm^2 (measured soil collar)

V = 5021.2 cm^3 (summed known volumes from manual)

dC/dt = (3.23-2.11)/(9:51:30 -9:48:17)=(1.12 µmol m^{-3})/(214 seconds) (from Figure A-9 above)

$$F = \frac{10 * 5021.2 * 100.6591\left(1-\frac{1}{1000}\right)}{8.314 * 217(25+273.15)}\frac{1.12}{214} = 0.049\ \mu mol\ m^{-2}s^{-1}$$

A.7 Alkalinity Titration

Figure A-10, Figure A-11 and Figure A-12 show the alkalinity titration results for port 20-30.

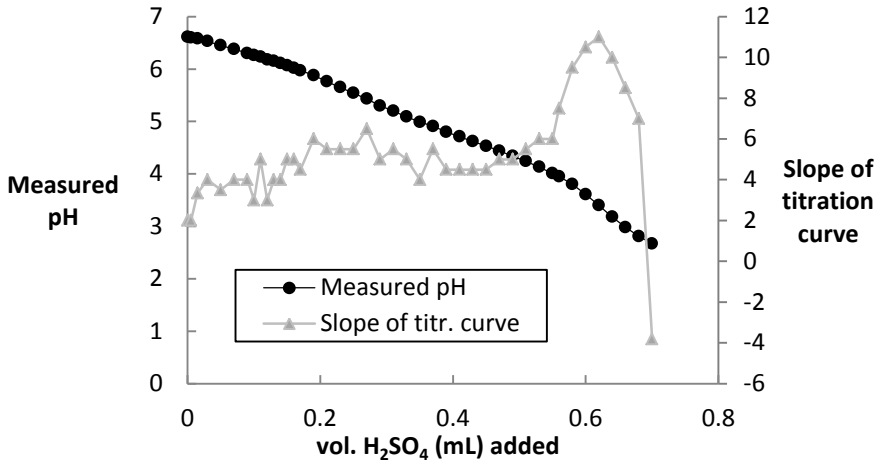

Figure A-10: Titration results for port 20-30

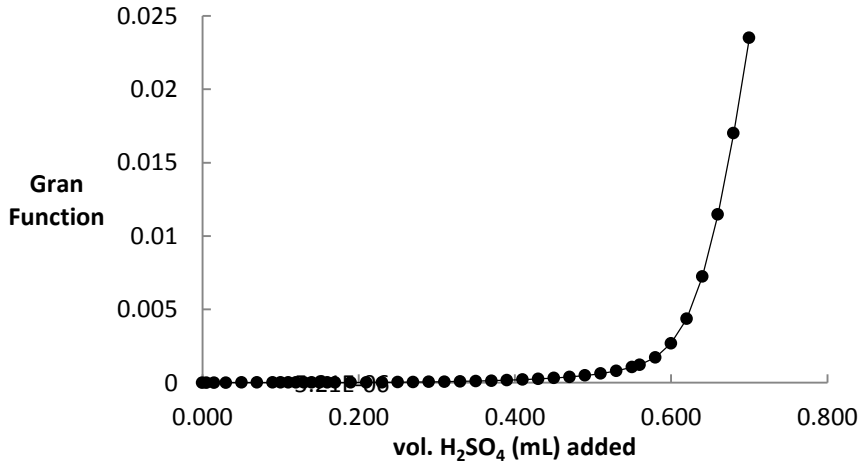

Figure A-11: Full Gran Function for port 20-30

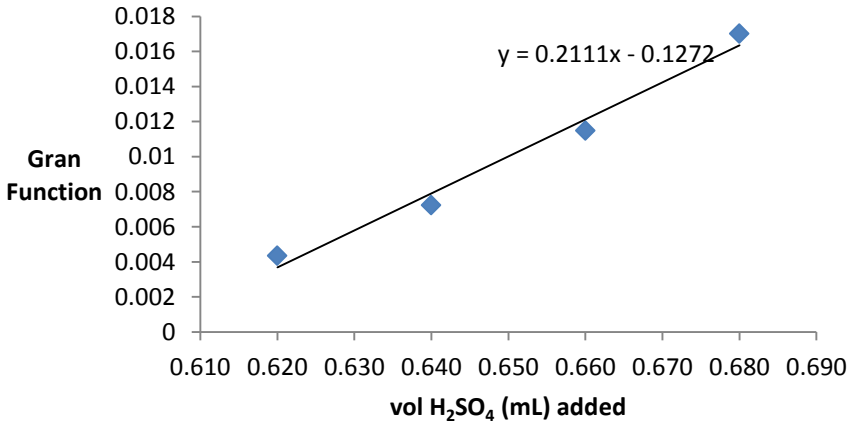

Figure A-12: Section of Gran Function used for calculation of alkalinity for port 20-30

Figure A-13, Figure A-14 and Figure A-15 show the alkalinity titration results for port 60-30.

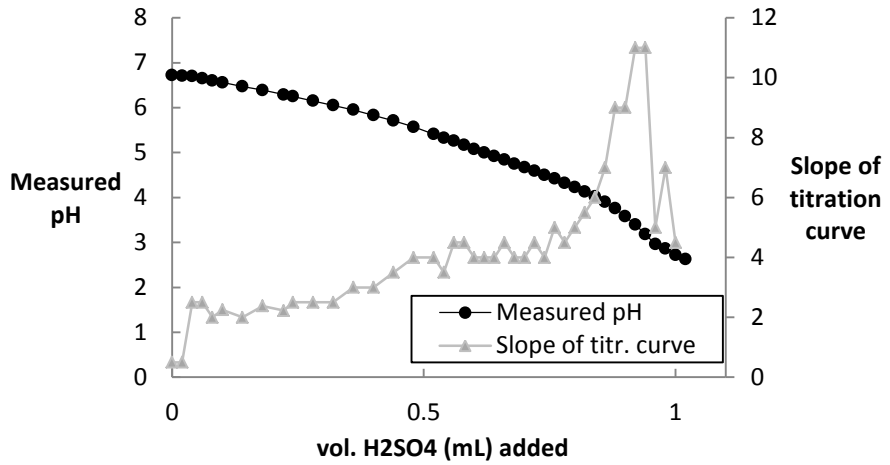

Figure A-13: Titration results for port 60-30

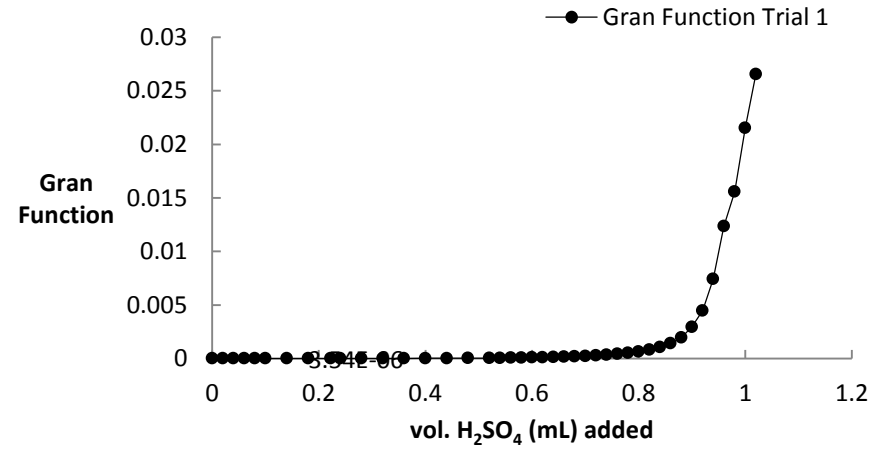

Figure A-14: Full Gran Function for port 60-30

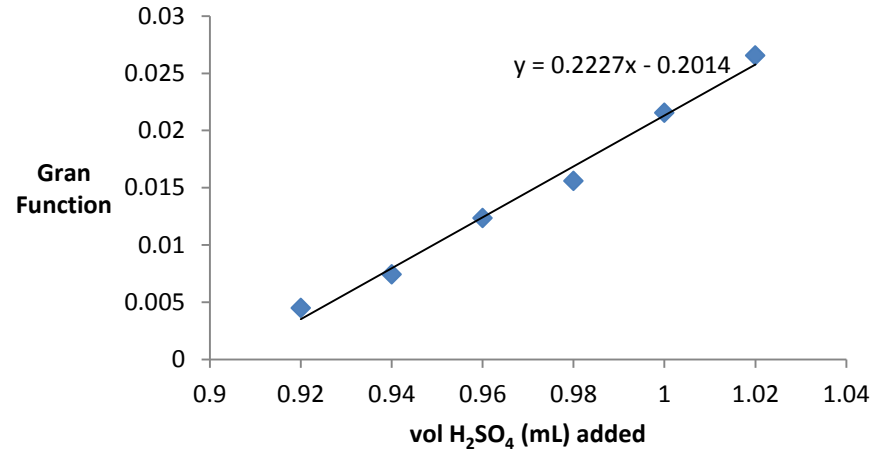

Figure A-15: Section of Gran Function used for calculation of alkalinity for port 60-30

Figure A-16, Figure A-17 and Figure A-18 show the alkalinity titration results for port 100-30.

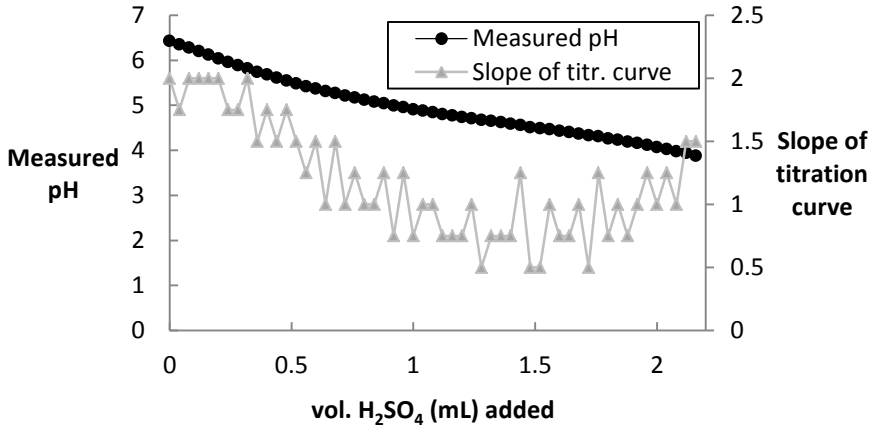

Figure A-16: Titration results for port 100-30

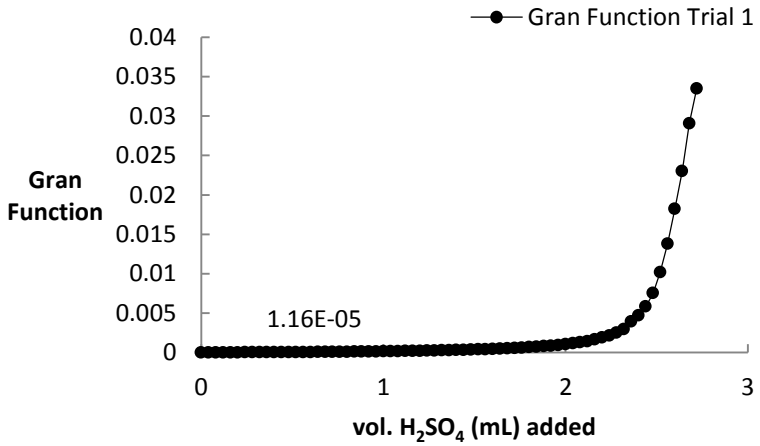

Figure A-17: Full Gran Function for port 100-30

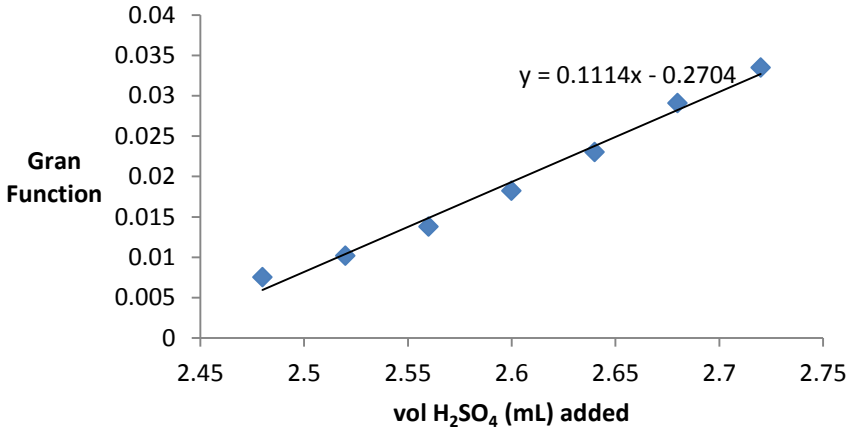

Figure A-18: Section of Gran Function used for calculation of alkalinity for port 100-30

Figure A-19, Figure A-20 and Figure A-21 show the alkalinity titration results for port 140-30.

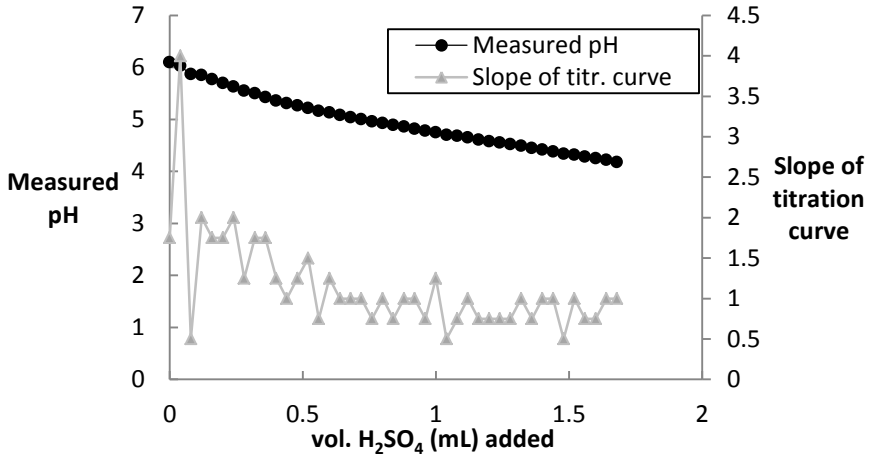

Figure A-19: Titration results for port 140-30

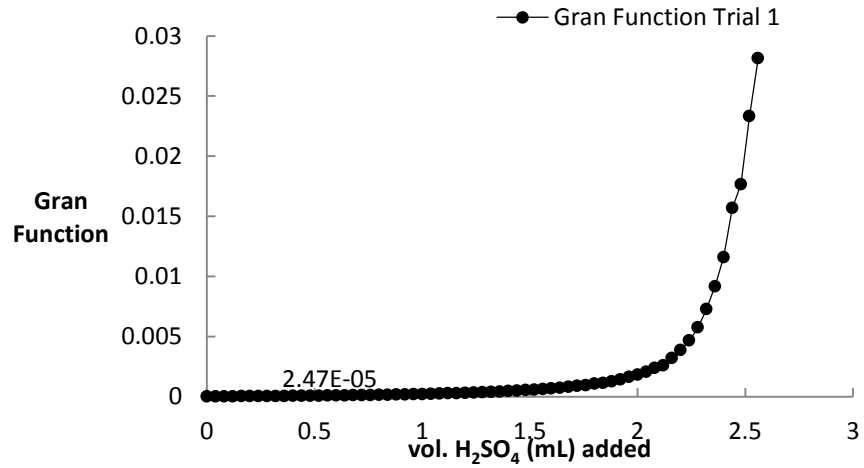

Figure A-20: Full Gran Function for port 140-30

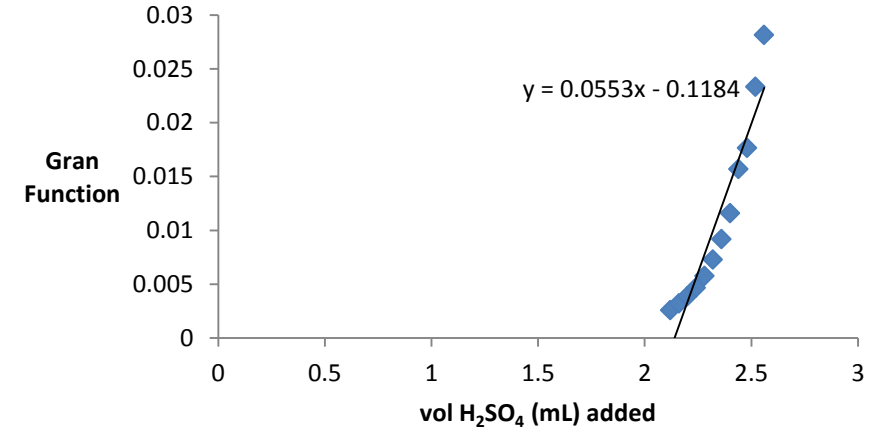

Figure A-21: Section of Gran Function used for calculation of alkalinity for port 140-30

Figure A-22, Figure A-23 and Figure A-24 show the alkalinity titration results for port 180-30.

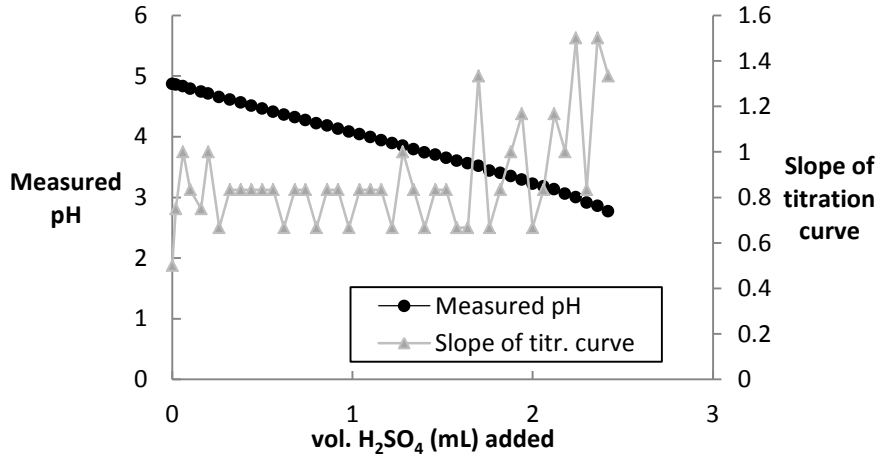

Figure A-22: Titration results for port 180-30

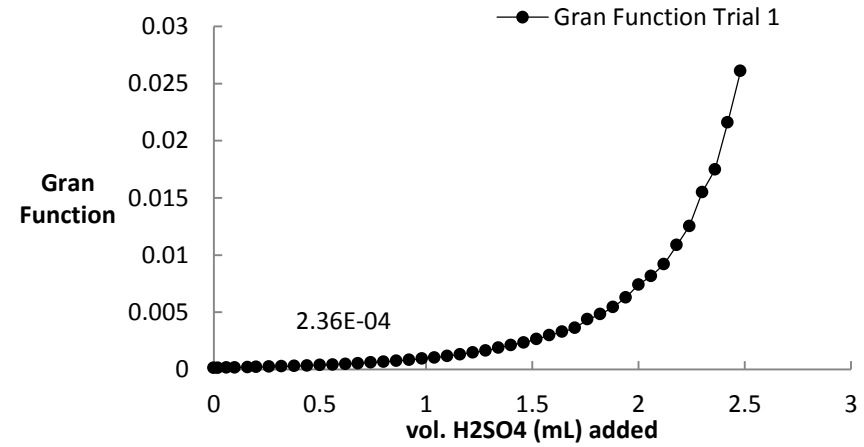

Figure A-23: Full Gran Function for port 180-30

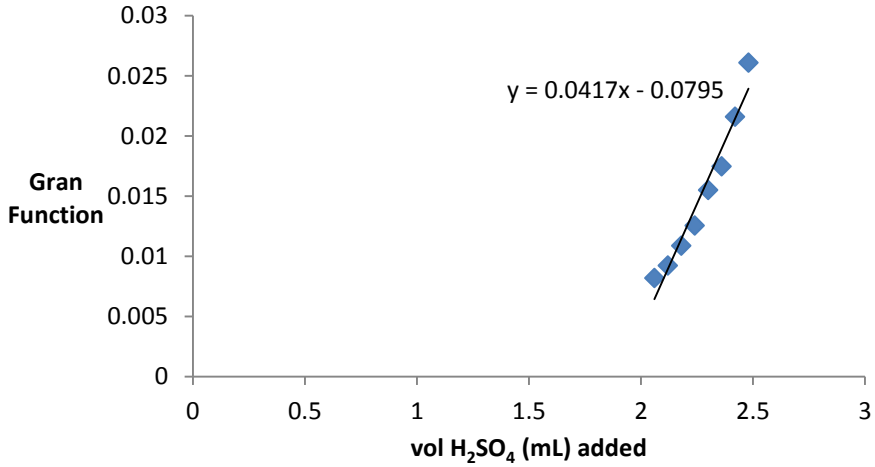

Figure A-24: Section of Gran Function used for calculation of alkalinity for port 180-30

B Appendix B

Appendix B contains the input and results for the PHREEQCi simulations.

B.1 PHREEQCi simulations

PHREEQCi simulations were completed to determine the saturation indices of various minerals as well as the approximate alkalinity at times when alkalinity measurements were not completed. The input results are shown in Table B-1. Each port was modeled as a batch simulation, and input parameters were taken from experimental data collected on the date shown.

Table B-1: PHREEQC simulation inputs

Date	Port	pH	Alk	Ca	Fe	Mn	Mg	Acet	Prop	But
Jan 8 2016	**20-30**	6.54	NA	199.2	0.8	22.1	35.9	287.8	97.8	26
	60-30	6.56	NA	207.5	2.1	28.4	42.4	171	73	21.6
	100-30	6.49	NA	1050	5.2	99.0	226.5	1172.1	347.2	89.2
	140-30	6.45	NA	1282	9.4	111.2	207.3	1535	429.3	107.6
	180-30	6.34	NA	1520	18.2	193.6	231.4	739.5	223.6	52.9
Mar 30 2016	**20-30**	6.26	937	330.9	13.2	63.2	60.3	220.3	75.1	23.2
	60-30	6.25	1406	354.2	5.6	63.3	64.6	513.1	170.1	58.3
	100-30	6.03	3774	1216	24.3	275	192.9	1750.4	511	116.5
	140-30	5.97	3329	656.2	76.0	190	107.4	1832.7	552	149.8
	180-30	4.87	2964	594.3	205	188	101.2	2085.1	590	169.8
Aug 23 2016	**20-30**	6.65	NA	170.2	7.4	31.1	63.2	190.7	113.1	16.7
	60-30	6.55	NA	286.9	7.9	49.7	88.7	390.8	221.6	42
	100-30	6.03	NA	546.1	42.5	75.7	79.8	1363.2	391.3	128.6
	140-30	5.97	NA	982	199.8	188.1	182.4	1301.6	398.1	163
	180-30	4.87	NA	571.4	338.4	107.5	91.5	476.3	250.6	69.4
	20-50	6.13	NA	110.1	47.7	17.7	33.2	86.9	93.8	18.7
	60-50	6.05	NA	93.08	24.2	13.2	20.2	112.5	21.1	19.9
	100-50	6.07	NA	5118	87.9	29.9	40.6	146.7	42.9	21.8
	140-50	4.95	NA	4920	34.8	30.8	44.3	283.9	67.2	39.2
	180-50	4.53	NA	6400.5	20.3	54.0	67.1	378.4	155.8	62

Table B-2 shows the PHREEQC output results for each simulation. The alkalinity is calculated for each port at the times where it was not measured. Saturation indices for $Al(OH)_3$, Al_2O_3, $CaSO_4$, MnO_2, $Fe(OH)_2$, $Fe(OH)_3$, Gibbsite, FeOOH, Fe_2O_3, Fe_2O_4 and MnOOH are given.

Table B-2: PHREEQC results for calculated alkalinity and saturation indices for a variety of minerals

			Saturation Indices										
Date	**Port**	**Alk (eq/kg)**	**$Al(OH)_3$ (am)**	**Al_2O_3**	**$CaSO_4$**	**MnO_2**	**$Fe(OH)_2$**	**$Fe(OH)_3$**	**Gibbsite**	**FeOOH**	**Fe_2O_3**	**Fe_3O_4**	**MnOOH**
Jan 8 2016	**20-30**	6.42E-03	-1.18	-0.52	-3.45	-13.31	-5.66	1.87	1.38	4.61	11.6	14.44	-5.43
	60-30	4.09E-03	-1.33	-0.82	-3.54	-13.13	-5.24	2.32	1.22	5.05	12.49	15.75	-5.27
	100-30	2.54E-02	-0.69	0.45	-3.24	-13.25	-5.33	2.15	1.86	4.89	12.16	15.33	-5.32
	140-30	3.28E-02	-0.45	0.95	-2.71	-13.41	-5.2	2.24	2.11	4.98	12.35	15.65	-5.44
	180-30	1.60E-02	-0.57	0.7	-2.12	-13.67	-5.18	2.15	1.98	4.89	12.16	15.49	-5.58
Mar 30 2016	**20-30**	NA	-1.46	-1.08	-3.4	-14.08	-5.08	2.17	1.1	4.91	12.2	15.62	-5.92
	60-30	NA	-0.82	0.2	-3.5	-14.17	-5.52	1.73	1.74	4.46	11.31	14.29	-6
	100-30	NA	-0.29	1.27	-3.25	-14.71	-5.61	1.41	2.27	4.15	10.68	13.58	-6.32
	140-30	NA	-0.78	0.28	-2.87	-15.02	-5.15	1.82	1.77	4.56	11.49	14.85	-6.56
	180-30	NA	-1.56	-1.26	-2.34	-19.42	-6.91	-1.05	1	1.69	5.77	7.38	-9.87
Aug 23 2016	**20-30**	4.92E-03	NA	NA	-3.92	-12.73	-4.54	3.1	NA	5.84	14.05	18.02	-4.96
	60-30	1.00E-02	0.09	2.02	-3.85	-13.02	-4.76	2.78	2.65	5.52	13.42	17.17	-5.14
	100-30	2.90E-02	-0.76	0.31	-3.49	-14.68	-4.99	2.13	1.79	4.87	12.11	15.63	-6.38
	140-30	2.80E-02	-0.76	0.33	-2.65	-15.47	-4.99	1.88	1.8	4.62	11.61	15.13	-6.92
	180-30	1.08E-02	-0.75	0.34	-2.44	-17.06	-5.36	1.13	1.81	3.87	10.11	13.25	-8.14
	20-50	2.85E-03	NA	NA	-3.96	-15	-4.65	2.48	NA	5.22	12.81	16.67	-6.71
	60-50	2.32E-03	NA	NA	-4.11	-15.41	-5.06	1.98	NA	4.72	11.81	15.26	-7.04
	100-50	3.27E-03	-1.27	-0.69	-3.39	-16.03	-5.5	1.56	1.29	4.3	10.98	13.98	-7.68
	140-50	4.80E-03	-2.73	-3.6	-2.78	-20.47	-8.12	-2.17	-0.17	0.57	3.51	3.91	-11
	180-50	5.57E-03	-2.11	-2.38	-2.16	-22.09	-9.37	-3.85	0.44	-1.11	0.16	-0.7	-12.19

C Appendix C

C.1 Biodiesel degradation rate calculation

The rate of biodiesel degraded was determined based on the slope of the cumulative % biodiesel degraded plot:

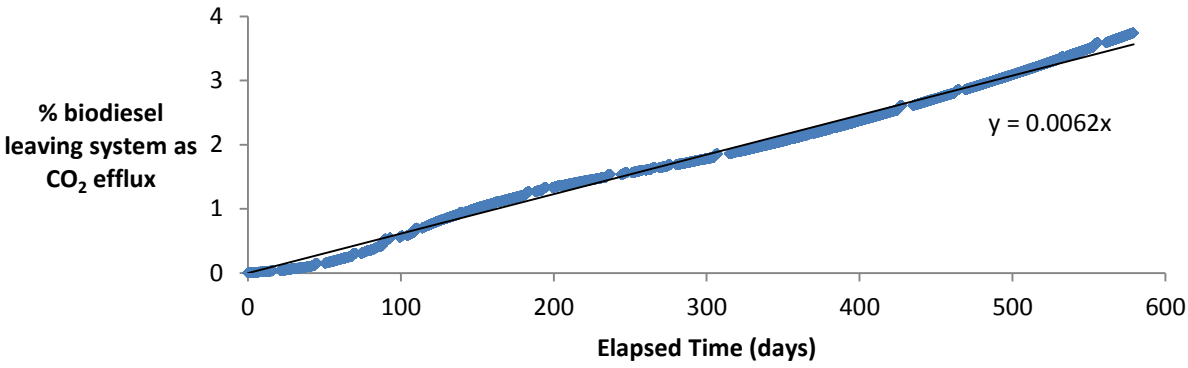

Figure C-1: trendline on % biodiesel leaving system as CO_2 efflux

The equation of the linear trend line is Y = 0.0062 X

Therefore the rate of efflux is 0.0062 % biodiesel day^{-1}. In the equation, this will be converted to a fraction and multiplied by the total amount of biodiesel.

The volume of sediments affected, assuming a residual volume of 0.4 m x 1.16 m x 1 m and a pool volume of 4 m x 0.04 m x 1 m, was 0.624 m^3.

The total amount of carbon in 80 L of biodiesel is 51.9 kg. Using unit conversion:

$$\frac{0.0062\%}{100\%} * \frac{1\ d}{24\ h} * \frac{1\ h}{60\ min} * \frac{1\ min}{60\ s} * 51.9\ kg * \frac{1000\ g}{kg} * \frac{1\ mol}{12\ g} = 3.1 * 10^{-6} mol\ s^{-1}$$

Dividing by the volume affected, = 5.0 x 10^{-6} mol m^{-3} s^{-1}

A secondary check was completed to make sure the calculated rate is reasonable.

Average CO_2 efflux from Chamber 2 (125 cm from the edge) is around 1 µmol m^{-2} day^{-1}.

Unit conversion:

$$1 * \frac{1\ mol}{1000000\ \mu mol} * \frac{4\ m^2}{0.624\ m^3} = 6.4 * 10^{-6} mol\ m^{-3} s^{-1}$$

This is reasonably close to the previous estimate, which used the cumulative biodiesel degraded.